

**Computational Study on Interaction of Heterocyclic,  
Triazine and Thionocarbamate Collectors with  
Pentlandite (Fe,Ni)<sub>9</sub>S<sub>8</sub> Mineral Surfaces**

**MASTER OF SCIENCE (MSc)**

**PHYSICS**

**N.N. Zavala 2025**

**Computational Study on Interaction of Heterocyclic,  
Triazine and Thionocarbamate Collectors with  
Pentlandite (Fe,Ni)<sub>9</sub>S<sub>8</sub> Mineral Surfaces**

**by**

**Nontobeko Nondumiso Zavala**

**DISSERTATION**

Submitted in fulfilment of the requirements for the degree of

**MASTER OF SCIENCE (MSc)**

**in**

**PHYSICS**

**in the**

**FACULTY OF SCIENCE AND AGRICULTURE**

**(School of Physical and Mineral Sciences)**

**at the**

**UNIVERSITY OF LIMPOPO**

**SUPERVISOR: Prof. P.P. Mkhonto**

**CO-SUPERVISORS: Prof. P.E. Ngoepe**

**2025**

## Declaration

I declare that the dissertation hereby submitted to the University of Limpopo, for the degree of Masters (Physics) has not previously been submitted by me for a degree at this or any other university; that it is my work in design and in execution, and that all material contained herein has been duly acknowledged.

Miss NN Zavala

**Full names**



A handwritten signature in black ink, appearing to read 'NNZ'.

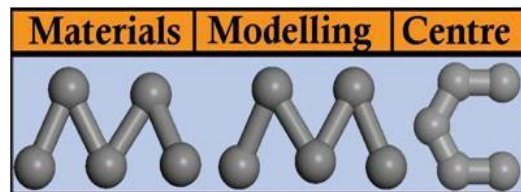
04-02-2025

**Signature and Date**

# Acknowledgements

I would like to reveal my appreciation to my supervisors Prof P.P. Mkhonto and Prof P.E. Ngoepe for supporting me throughout the course of this honours project. I am sincerely thankful for their aspiring recommendations, friendly advice and also the sharing of truthful and helpful views on a number of matters related to the project work.

I would also like to acknowledge the National Research Foundation for their financial support. The Materials Modelling Centre (MMC) for giving me the permission to use all the required equipment's and necessary materials to complete the project. Lastly, I express my endless love and gratitude to my dearest family, for their help and understanding through the time span of my studies.



# **Dedication**

## **My Late Mother**

Dudu Nokuthula Ntshangase

## **My Son**

Duma Nkosinhle Nkolo Lwanzi Zavala

## **My Parents**

Wonderboy Nkosinathi Zavala

Nandi Samukelisiwe Sqedili Zavala

## **My Siblings**

Sinenhlahla Noxolo Xulu

Kwenzeka Zavala

Siyanda Zavala

Champion Mngqobi Obrigado Zavala

Mercy Akabongwe Sicoco Zavala

Prince Zenthia Zavala

## Abstract

Due to the demands of nickel, substantial effort has been put into the recovery of pentlandite. Enhancing the separation of pentlandite minerals from the gangue in the extracted ores remains a problem. Pentlandite is the major source of nickel as well as a major carrier of platinum group elements (PGEs). Nickel is utilised in a wide range of industrial applications such as stainless steel, coinage, and rechargeable batteries. There is a need for selective collectors that can supplement the available xanthates, dithiophosphate and dithiocarbamate collectors for recovery of pentlandite and nickel ores. This study adopted density functional theory (DFT) with dispersion correction by Grimme to investigate the interaction with selective thiol collectors: S-allyl-N-diethyl-dithiocarbamate (ADEDTC), O-isopropyl-N-diethyl-thionocarbamate (IPDETC), Sodium mercaptobenzothiazole (MBT) and Sodium-2,6-Dithio-4-Butylamino-1,3,5-Triazine (SDTBAT) collectors.

The bulk  $\text{Fe}_5\text{Ni}_4\text{S}_8$  pentlandite was previously determined as the most stable compound from cluster expansion which was tetragonal with space group of  $P4_2/nmc$ . The optimised structure had lattice dimensions of  $a = b = 7.020 \text{ \AA}$  and  $c = 9.930 \text{ \AA}$ . The XRD was used to predict the most dominant surface which were found as (111), (211), (224), and (311) surface, with the (311) surface displaying the highest intensity. These were cleaved from the relaxed bulk structure and their surface energies were computed as  $1.622 \text{ J/m}^2$  (111 surface)  $1.843 \text{ J/m}^2$  (211 surface)  $1.844 \text{ J/m}^2$  (224 surface) and  $1.484 \text{ J/m}^2$  (311 surface). The most stable surface was found to be the (311) surface which was in agreement with the experimental X-ray diffraction pattern.

The adsorptions were performed on Ni and Fe atoms of  $\text{Fe}_5\text{Ni}_4\text{S}_8$  (311) surface as preferred adsorption sites. It was found that ADEDTC gave the most exothermic adsorption energy of  $-460.581 \text{ kJ/mol}$  compared to MBTNa ( $-249.59 \text{ kJ/mol}$ ), IPDETC ( $-161.012 \text{ kJ/mol}$ ) and SDTBAT ( $-352.481 \text{ kJ/mol}$ ). Most significantly these collectors preferred to bind on Ni atoms than Fe atoms, which indicated their selectivity towards the pentlandite mineral. These suggested that ADEDTC was the best co-collector compared to IPDETC, SDTBAT and MBTNa collectors for utilisation in the flotation of pentlandite mineral. The adsorption strength decreasing in order: ADEDTC > MBTNa > SDTBAT > IPDETC. This suggests that the ADEDTC collector has the potential to replace and/or be a co-collector with the widely used collectors in the recovery of pentlandite minerals.

# Table of Contents

CHAPTER 1.....	1
Introduction .....	1
1.1 General Background .....	2
1.2 Literature Review .....	3
1.3. Minerals separation.....	5
1.4 Structural Aspects.....	7
1.5 Significance of the Study.....	8
1.6 Rationale, Objectives and Research questions .....	9
1.6.1 Rationale .....	9
1.6.2 Objectives .....	9
1.6.3 Research questions .....	10
1.7 Outline of the dissertation.....	10
CHAPTER 2.....	12
Density Functional Theory Method.....	12
2.1 Density Functional Theory (DFT).....	13
2.1.1 Local density approximation.....	15
2.1.2 General Gradient Approximation.....	16
2.1.3 Dispersion corrections to DFT .....	17
2.2 Plane-wave Pseudopotential Method.....	19
2.2.1 Plane-wave Basis.....	19
2.2.2 Pseudopotential Method .....	20
2.2.3 Projector Augmented Wave Method .....	21
2.2.4 Ultrasoft Pseudopotential.....	22
2.3 K-points sampling .....	22
2.4 VASP implementation.....	23
2.5 Theoretical background of calculated properties .....	24
2.5.1 Density of states .....	24
2.6 Charge population analysis .....	25
CHAPTER 3.....	27
Bulk and Surface Modelling .....	27
3.1 Convergence of the cut-off energy and k-point sampling .....	28
3.1.1 Cut-off energy sampling.....	28
3.1.2 Bulk k-points sampling .....	29
3.2 Surface k-points sampling for Fe <sub>5</sub> Ni <sub>4</sub> S <sub>8</sub> .....	29
3.3 Computational details.....	30

3.4 Bulk $\text{Fe}_5\text{Ni}_4\text{S}_8$ Pentlandite Properties.....	31
3.6 Surface modelling of $\text{Fe}_5\text{Ni}_4\text{S}_8$ .....	34
3.5 Cleaving of (211), (224), (111) and (311) surfaces.....	34
3.6.1 Different surface termination of $\text{Fe}_5\text{Ni}_4\text{S}_8$ (111), (211), (224) and (311) surfaces.....	37
3.6.2 Non-dipole (111), (211), (224) and (311) surface optimisation of $\text{Fe}_5\text{Ni}_4\text{S}_8$ .....	39
3.6.3 Electronic properties of the clean (311) surface.....	41
3.7 Summary.....	42
CHAPTER 4.....	44
Adsorption of collectors on $\text{Fe}_5\text{Ni}_4\text{S}_8$ (311) Surface.....	44
4.1 Collectors geometries and energies.....	45
4.1.1 Molecular geometry of isolated heterocyclic, s-triazine and thionocarbamate collectors ..	45
4.1.2 DOS of ADEDTC, IPDETC, MBTNa and SDTBAT.....	48
4.2 ADEDTC, IPDETC, MBTNa, S-triazine adsorptions on $\text{Fe}_5\text{Ni}_4\text{S}_8$ (311) surface.....	50
4.3 Density of states of ADEDTC, IPDETC, MBTNa and SDTBAT adsorptions.....	56
4.3.1 Electronic properties of ADEDTC, IPDETC, MBTNa and SDTBAT adsorption on $\text{Fe}_5\text{Ni}_4\text{S}_8$ (311) surface.....	57
4.4 Summary.....	67
CHAPTER 5.....	68
Summary and Conclusion.....	68
Recommendations and future work.....	70
References.....	71
Appendix A: Explanation data of the project.....	79
Appendix B: Papers presented at conferences.....	80
Appendix C: Tables.....	81
Appendix D: ADEDTC, IPDETC, MBT and SDTBAT adsorption on $\text{Fe}_5\text{Ni}_4\text{S}_8$ (311) surface.....	82

# List of figures

Figure 1.1: The Bushveld Igneous Complex geological map [9]. .....	2
Figure 1.2 : Schematic diagram of a flotation cell. ....	7
Figure 1.3 : The unit cell of $\text{Fe}_5\text{Ni}_4\text{S}_8$ bulk [36]. ....	8
Figure 2.1 : The relation of both the electron potential of the all-electron potential of the nucleus (blue dash lines) and the pseudopotential potential of a coulomb wave (red solid lines). The function of the pseudo-wave, the real, and potential corresponds to the radius $r_c$ above [42]. ....	21
Figure 3.1: Total energy against kinetic energy cut-off of tetragonal $\text{Fe}_5\text{Ni}_4\text{S}_8$ structure. ....	28
Figure 3.2: Total energy against k-points mesh $\text{Fe}_5\text{Ni}_4\text{S}_8$ tetragonal structures. ....	29
Figure 3.3 : Total energy against k-points mesh $\text{Fe}_5\text{Ni}_4\text{S}_8$ surface structures. ....	30
Figure 3.4 : The relaxed unit cell of $\text{Fe}_5\text{Ni}_4\text{S}_8$ bulk. ....	32
Figure 3.5 : Density of states $\text{Fe}_5\text{Ni}_4\text{S}_8$ bulk model. ....	33
Figure 3.6 : Computational generated XRD for $\text{Fe}_5\text{Ni}_4\text{S}_8$ bulk model. ....	34
Figure 3.7 : A simplified representation of the (000) surface cleavage methodology for on $\text{Fe}_5\text{Ni}_4\text{S}_8$ . ....	35
Figure 3.8 : Representation of the different types of surfaces. ....	36
Figure 3.9 : Shows different terminations for $\text{Fe}_5\text{Ni}_4\text{S}_8$ (111) surface. ....	37
Figure 3.10 : Shows different terminations for $\text{Fe}_5\text{Ni}_4\text{S}_8$ (211) surface. ....	38
Figure 3.11 : Shows different terminations for $\text{Fe}_5\text{Ni}_4\text{S}_8$ (224) surface. ....	38
Figure 3.12 : Shows different terminations for $\text{Fe}_5\text{Ni}_4\text{S}_8$ (311) surface. ....	38
Figure 3.13 : Shows $\text{Fe}_5\text{Ni}_4\text{S}_8$ un-relaxed and relaxed non-dipole surface: (a) (111), (b) (211), (c) (224) and (d) (311) surface terminations. ....	40
Figure 3.14 : Surface density of states of $\text{Fe}_5\text{Ni}_4\text{S}_8$ (311) surfaces. ....	42
Figure 4.1: Relaxed molecular geometries of organic collectors: ADEDTC, IPDETC, MBTNa and SDTBAT. ....	46
Figure 4.2: Collector density of states: (a) ADEDTC, (b) IPDETC, (c) MBTNa and (d) SDTBAT. ....	49
Figure 4.3: The un-relaxed and relaxed ADEDTC collector adsorption on the $\text{Fe}_5\text{Ni}_4\text{S}_8$ (311) surface. ....	51
Figure 4.4 : The un-relaxed and relaxed IPDETC collector adsorption on the $\text{Fe}_5\text{Ni}_4\text{S}_8$ (311) surface. ....	53
Figure 4.5 : The un-relaxed and relaxed MBTNa collector adsorption vertically on the $\text{Fe}_5\text{Ni}_4\text{S}_8$ (311) surface. ....	53
Figure 4.6 : The un-relaxed and relaxed MBTNa collector adsorption horizontally on the $\text{Fe}_5\text{Ni}_4\text{S}_8$ (311) surface. ....	55
Figure 4.7 : The un-relaxed and relaxed SDTBAT collector adsorption on the $\text{Fe}_5\text{Ni}_4\text{S}_8$ (311) surface. ....	56

Figure 4.8 : Partial density of states (PDOS) of ADEDTC collector before and after adsorption on $\text{Fe}_5\text{Ni}_4\text{S}_8$ (311) surface: (a) Ni site adsorption and (b) Fe site adsorption.....	59
Figure 4.9 : Partial density of states (PDOS) of IPEDTC collector before and after adsorption on $\text{Fe}_5\text{Ni}_4\text{S}_8$ (311) surface: (a) Ni site adsorption and (b) Fe site adsorption.....	61
Figure 4.10 : Partial density of states (PDOS) of MBTNa collector before and after adsorption on $\text{Fe}_5\text{Ni}_4\text{S}_8$ (311) surface: (a) Ni site adsorption and (b) Fe site adsorption.....	62
Figure 4.11: Partial density of states (PDOS) of MBTNa collector before and after adsorption on $\text{Fe}_5\text{Ni}_4\text{S}_8$ (311) surface: (a) Ni site adsorption and (b) Fe site adsorption.....	65
Figure 4.12 : Partial density of states (PDOS) of STDBAT collector before and after adsorption on $\text{Fe}_5\text{Ni}_4\text{S}_8$ (311) surface: (a) Ni site adsorption and (b) Fe site adsorption.....	66
Figure D1.1: The un-relaxed and relaxed ADEDTC collector adsorption on the $\text{Fe}_5\text{Ni}_4\text{S}_8$ (311) surface.....	82
Figure D1.2: The un-relaxed and relaxed ADEDTC collector adsorption on the $\text{Fe}_5\text{Ni}_4\text{S}_8$ (311) surface.....	83
Figure D1.3: The un-relaxed and relaxed ADEDTC collector adsorption on the $\text{Fe}_5\text{Ni}_4\text{S}_8$ (311) surface.....	83
Figure D1.4: The un-relaxed and relaxed IPDETC collector adsorption on the $\text{Fe}_5\text{Ni}_4\text{S}_8$ (311) surface. ....	84
Figure D1.5: The un-relaxed and relaxed IPDETC collector adsorption on the $\text{Fe}_5\text{Ni}_4\text{S}_8$ (311) surface. ....	84
Figure D1.6: The un-relaxed and relaxed IPDETC collector adsorption on the $\text{Fe}_5\text{Ni}_4\text{S}_8$ (311) surface. ....	85
Figure D1.7: The un-relaxed and relaxed MBTNa collector adsorption vertical on the $\text{Fe}_5\text{Ni}_4\text{S}_8$ (311) surface.....	86
Figure D1.8: The un-relaxed and relaxed MBTNa collector adsorption vertical on the $\text{Fe}_5\text{Ni}_4\text{S}_8$ (311) surface.....	87
Figure D1.9: The un-relaxed and relaxed MBTNa collector adsorption vertical on the $\text{Fe}_5\text{Ni}_4\text{S}_8$ (311) surface.....	88
Figure D1.10: The un-relaxed and relaxed MBTNa collector adsorption horizontal on the $\text{Fe}_5\text{Ni}_4\text{S}_8$ (311) surface. ....	89
Figure D1.11: The un-relaxed and relaxed MBTNa collector adsorption horizontal on the $\text{Fe}_5\text{Ni}_4\text{S}_8$ (311) surface. ....	90
Figure D1.12: The un-relaxed and relaxed MBTNa collector adsorption horizontal on the $\text{Fe}_5\text{Ni}_4\text{S}_8$ (311) surface. ....	90
Figure D1.13: The un-relaxed and relaxed STDBAT collector adsorption on the $\text{Fe}_5\text{Ni}_4\text{S}_8$ (311) surface.....	91

Figure D1.14: The un-relaxed and relaxed STDBAT collector adsorption on the  $\text{Fe}_5\text{Ni}_4\text{S}_8$  (311) surface.....91

## List of tables

Table 1.1 : The atomic positions in pentlandite Fe <sub>5</sub> Ni <sub>4</sub> S <sub>8</sub> crystal structure from CE.....	8
Table 3.1 The relaxed atomic positions (Wyckoff notation) in pentlandite Fe <sub>5</sub> Ni <sub>4</sub> S <sub>8</sub> crystal structure [55] from CE.....	32
Table 3.2 : (111), (211), (224) and (311) surface optimisation of Fe <sub>5</sub> Ni <sub>4</sub> S <sub>8</sub> , number of atoms per slab, total energy (eV) and surface energies (J/m <sup>2</sup> ). .....	39
Table 3.3 : Atomic vertical displacements ( $\Delta d_z$ , Å) of the (111), (211), (224) and (311) surface of Fe <sub>5</sub> Ni <sub>4</sub> S <sub>8</sub> , obtained from the unrelaxed ( $d_{z(U)}$ ) and relaxed ( $d_{z(R)}$ ) Z-atomic position. ....	41
Table 4.1: Calculated bond lengths ( $R$ , in Å), bond angles ( $\theta$ , in deg.) and torsion angle ( $\phi$ , in deg.). The theoretical/experimental values are shown in parenthesis for comparison.....	47
Table 4.2: Calculated HOMO and LUMO energies. ....	47
Table D1.1: The adsorption energies of ADEDTC on the Fe <sub>5</sub> Ni <sub>4</sub> S <sub>8</sub> (311) mineral surfaces (kJ/mol). 83	
Table D1.2: The adsorption energies of IPDETC on the Fe <sub>5</sub> Ni <sub>4</sub> S <sub>8</sub> (311) mineral surfaces (kJ/mol)....	85
Table D1.3: The adsorption energies of MBTNa on the Fe <sub>5</sub> Ni <sub>4</sub> S <sub>8</sub> (311) mineral surfaces (kJ/mol). ...	88
Table D1.4: The adsorption energies of MBTNa on the Fe <sub>5</sub> Ni <sub>4</sub> S <sub>8</sub> (311) mineral surfaces (kJ/mol). ...	90

## List of Abbreviations

PGEs	Platinum Group Elements
PGMs	Platinum Group Minerals
DFT	Density Functional Theory
GGA	Generalized Gradient Approximations
GGA-PBE Enzerhorf	Generalized Gradient Approximations Perdew-Burke
LSDA	Local Spin Density Approximation
LDA	Local Density Approximation
H-K	Hohenberg-Kohn
K-S	Kohn-Sham
CASTEP	Cambridge Serial Total Energy Package
USP	Ultrasoft Pseudopotential
PAW	Project Augmented Wave
SCC	Self-Consistent Redistribution of Charges
DOS	Density of States
TDOS	Total Density of States
VB	Valence Band
CB	Conduction Band
$E_F$	Fermi Energy
eV	Electron Volte
Å	Angstrom
ADEDTC	S-allyl-N-diethyl-dithiocarbamate
IPDETC	O-isopropyl-N-diethyl-thionocarbamate

SDTBAT

Sodium-2,6-Dithio-4-Butylamino-1,3,5-Triazine

MBTNa

Sodium mercaptobenzothiazole

# **CHAPTER 1**

## **Introduction**

## 1.1 General Background

Pentlandite  $(\text{Fe}, \text{Ni})_9\text{S}_8$  was named after the Irish scientist Joseph Barclay Pentland. It is pale yellow-bronze with a subtle bronze-brown stripe and a metallic lustre. The pentlandite hardness ranges from 3.5 to 4.0 on the Mohs scale, with a moderate specific gravity of 4.6 to 5.0. The pentlandite mineral is composed of about 22% Ni, 42% Fe, and 36% S [1] and usually contains some amount of cobalt in nature [2]. The most common terrestrial nickel sulphide is pentlandite, which usually forms after cooling of magmatic sulphide melts during the formation of parent silicate melt [1]. Furthermore, pentlandite also forms from immiscible sulphide-silicate melts in normal mantle and crustal conditions [3]. The platinum group elements (PGEs) can occur either as discrete platinum group minerals (PGMs) or in solid solution within base metal sulphides (BMS), including pentlandite, chalcopyrite, pyrrhotite, and pyrite. [3, 4, 5]. Pentlandite is located inside the lower margins of mineralized ultramafic to mafic layered intrusions that are in different locations all over the world [7]. For instance, it is located in the Bushveld Igneous Complex of South Africa; the Voiseys Bay troctolite intrusive composite in Canada; and the Duluth gabbro in the United State of Minnesota, where it develops a crucial nickel ore.

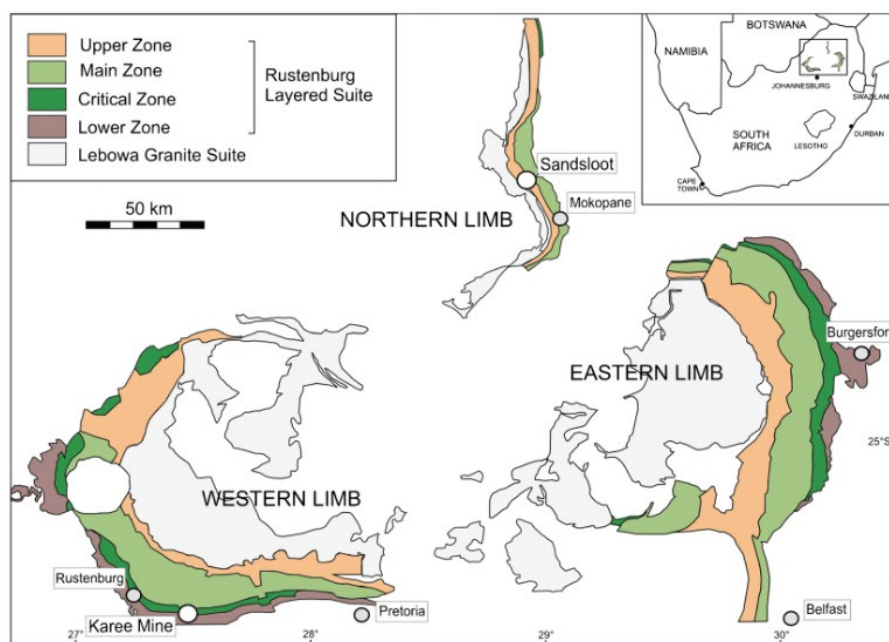


Figure 1.1: The Bushveld Igneous Complex geological map [8].

In South Africa, the Bushveld Igneous Complex as shown in Figure 1.1, is the biggest layered igneous intrusion within the Earth's crust, and it is known for hosting some of the richest mineral resources. The complex has the world's greatest reserves of platinum-group metals (PGMs), such as platinum, palladium, osmium, iridium, rhodium, and ruthenium, as

well as massive amounts of iron, tin, chromium, titanium, and vanadium. The Bushveld complex is a pear-shaped. The western limb extends into the Northwest and Gauteng provinces, while the eastern limb spans portions of the Limpopo and Mpumalanga provinces [9].

## 1.2 Literature Review

Nickel mining is widespread in numerous countries and plays a key role in various industrial applications, including the production of stainless steel, coins, and rechargeable batteries. This has led to a growing demand for nickel, which is projected to be depleted by 2030 [9, 10]. To be viable, the nickel sulphide processing sector must become more efficient and cost-effective. Nickel demand is rising, environmental regulations on sulphur emissions are tightening, nickel oxide ores are competing for the role of principal nickel source, and xanthate collectors are insufficiently selective [12]. Furthermore, there is still a lack of surface exploration of these minerals to explain their crystal shape and properties relevant to their computational recovery. Previously the flotation of natural and synthetic  $(\text{Fe, Ni})_9\text{S}_8$  pentlandite for beneficiation of nickel has been studied by experimental techniques and gave useful insight in understanding the surface reaction of this mineral [13]. Pentlandite and nickel ore flotation has always been achieved using a range of collectors such as xanthates, dithiophosphate and dithiocarbamates, which were not so effective [1, 13, 14].

The flotation technique is one of the most used methods for separating minerals, and it employs thiol collectors such as xanthates, which are usually supplemented with selective collectors such as dithiophosphate and dithiocarbamate [16]. Although these collectors have been employed in metallurgical processes for a long time, there is still a challenge in finding a best collector that will possess both flotation power and selectivity performance. The current collectors are favoured for froth flotation of sulphide mineral ores due to their high electron attraction for sulphide minerals and are sulphur donors [17]. Thionocarbamates (TC) are another class of thiol collectors used in sulphide minerals selective froth flotation. Thionocarbamates are commonly employed as selective for copper in the froth flotation of chalcopyrite over pyrite and galena [17,18]. However, there has not been much research on their utilisation for nickel selectivity in pentlandite. It has been reported that the mixture of xanthate and thionocarbamate collector was the most selective and gave good performance in terms of grade and recovery [20].

Other collectors are heterocyclic, such as 2-mercaptobenzoxazole (MBO) for chalcocite ( $\text{Cu}_2\text{S}$ ), 2-mercaptobenzothiazole (MBT) for galena ( $\text{PbS}$ ) and 2-aminothiophenol (ATP) for

sphalerite (ZnS), which have been studied and have advantages since they can be used in neutral pH and show good selectivity [21]. It has been reported that the heterocyclic compounds can form hydrophobic complexes with many metals such as iron, copper, cobalt and nickel [22]. This indicated that with a benzene ring or mercapto ring present in the collector reagents highly selective collectors were produced. Recently a study was conducted on modification to form a derivative of MBT, MBO and mercaptobenzimidazole (MBI) by introducing a trithiocarbonate (TTC) for flotation of pyrite, and it was found that the derivatives improved the flotation of pyrite under weak acidic (pH = 6) conditions [23]. The triazine compounds, which are a class of nitrogen-containing heterocycles with a molecular formula of  $C_3H_3N_3$ , have not been extensively reported as collectors for minerals separation and are potential collector molecules for sulphide minerals. Recently, an experimental and density functional theory (DFT) study on pyrite using s-triazine such as sodium dithio-butyl-amino-triazine (SDTBAT), in comparison to xanthate and dithiocarbamate of the butyl chain demonstrated that s-triazine had superior flotation and adsorption for pyrite [24]. Moreover, a similar DFT study was recently performed on the cooperite (101) surface, and it was found that s-triazine had stronger adsorption than xanthate and dithiocarbamate [25].

There are few studies on the computational and experimental components of pentlandite separation. Furthermore, innovative collectors that work better than the current xanthate collector and increase the separation of BMSs and PGMs through flotation are still needed. Previously, experimental techniques were used to study pentlandite flotation, which provided insights into the mineral's surface reactivity [1, 13, 14]. It has been reported that xanthates bind more than hydroxide anions to Fe-enriched pentlandite, while on the Ni-enriched pentlandite hydroxide anions bind stronger to xanthates [26]. The potassium amyl xanthate (PAX), sodium isobutyl xanthate (SIBX), and sodium ethyl xanthate (SEX) collectors were studied by Ikotun et al. (2017) to maximise nickel and pentlandite recovery. It was found that the SEX collector collected more nickel and pentlandite contents than the PAX and SIBX collectors [27]. Otunniyi et al. (2016) investigated the flotation separation of pentlandite-pyrrhotite-chalcopyrite with the addition of various dosages of copper sulphate for nickel recovery responses. The study showed that with copper sulphate dosage increased, the nickel recovery was improved in comparison to no addition, although the trend exhibited a maximum after which depression was observed [28].

The DFT study on interaction of SEX, SIBX, and diethyl dithiophosphate (DEDTP) thiol collectors on the nickel-rich pentlandite ( $Fe_4Ni_5S_8$ ) (110) surface was conducted to predict the collecting performances during flotation. The study showed that DEDTP had the best

adsorption strength on the nickel-rich pentlandite mineral amongst the three collectors. Furthermore, they discovered that Fe atoms exhibited the strongest adsorption compared to Ni atoms [29]. Recently, the first-principles calculations were used to reveal the interfacial bonding mechanisms of xanthate and dixanthogen with pentlandite, pyrrhotite, and their heterostructure. It was reported that xanthate bind more strongly with the pentlandite surface based on adsorption configurations and adsorption energy. Furthermore, the adsorption energy and electron localization function showed that the adsorption of collectors on the pentlandite surface had higher priority than pyrrhotite due to the high activity of pentlandite and the existence of galvanic interactions [30]. Another recent study on combined collector showed that the flotation performance of the combined collector system for pentlandite surpasses that of NaBX or NAOITC alone. Furthermore, the FTIR and XPS results reveal that NaBX and NAOITC can chemically adsorb onto the surface of pentlandite. This was supported by computational aspects which showed that the two collectors, enhance the adsorption capacity of each collector on the mineral surface, thereby augmenting the impact of the combined collector system on pentlandite's hydrophobicity. As such the NAOITC collector has great potential to enhance the recovery rate of nickel in industrial beneficiation [31]. There is a clear gap for improving the recovery of pentlandite minerals.

Therefore, there is a need for highly selective and powerful collectors to replace the xanthate and consequently improve the floatability of pentlandite. In addition, the heterocyclic, thionocarbamates and s-triazine collectors have been found to be selective with good flotation performance for sulphides such as chalcopyrite and pyrite. However, their use for pentlandite has never been reported. This study employed the computational methods to investigate the  $(\text{Fe, Ni})_9\text{S}_8$  pentlandite, starting from surface orientations and terminations of the stable pentlandite model to identify the most stable surface. The adsorptions of heterocyclic: sodium mercaptobenzothiazole (MBT), novel triazine: sodium 2,6-dithio-4-butylamino-1,3,5-triazine (SDTBAT) and thionocarbamate: O-isopropyl-N-diethyl-thionocarbamate (IPDETC) and S-allyl-N-diethyl-dithiocarbamate (ADEDTC) collectors will be performed on the most stable surface. The adsorptions onto the surface will be complemented by electronic structures to describe the chemistry of bonding and consequently identify the best- performing collectors suitable for pentlandite flotation.

### **1.3. Minerals separation**

Mineral processing, also known as ore dressing, mineral beneficiation, or mineral engineering, is described as the science and art of extracting valuable metallic and non-

metallic minerals from gangue minerals [1]. The appropriate procedure is determined by taking advantage of variance in the physical and chemical properties of minerals. There are many separation methods, such as electrostatic, magnetic, flotation, leaching, ore sorting, dense medium, dewatering and tailings management. The electrostatic method separates particles with various electrical charges and, if possible, sizes. Magnetic separation is based on the varying degrees of attraction exerted by magnetic fields on particular minerals. To be successful, the feed particles must fall within a specific size range (0.1 to 1 mm). Flotation is the most common process for concentrating fine-grained materials [15]. It makes use of the various physicochemical surface features of minerals, particularly their wettability, which can be natural or purposefully altered by chemical reagents. Gravity techniques exploit the difference in mineral density as the concentrating agent; they are used when flotation is inefficient and operational costs are high due to exceedingly complex physical, chemical, and mechanical concerns [32].

The flotation method involved thoroughly mixing pulverised ore, oil, and an acid or salt to form a pulp, followed by agitation of the pulp on an irregular work surface, initially a washboard. In this process the valuable or target minerals rise to the surface, while waste settles in recessed areas at tailings [33].

The froth flotation process initiates with reduction, wherein the ore is finely crushed to a dimension where the desired minerals are liberated. The crushed ore is then mixed with water to form slurry [33]. To render the mineral's properties hydrophobic, a collector is introduced into the slurry. This slurry transforms into pulp, which is subsequently added to a water-filled container. Air jets are then introduced into the mixture, generating bubbles. The desired mineral, being repelled by water, attaches itself to these air bubbles. As the bubbles rise to the surface, carrying mineral particles, they form froth. The froth is separated and undergoes further refining and extraction processes [34]. Figure 1.2 demonstrates the flotation process.

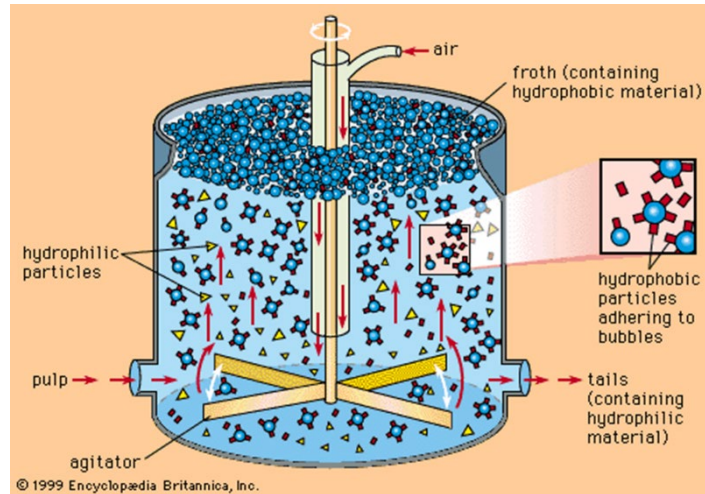


Figure 1.2 : Schematic diagram of a flotation cell.

Collectors are reagents engineered to specifically attach to particle surfaces, forming a monolayer composed of thin films of non-polar, hydrophobic hydrocarbons. This monolayer substantially increases the contact angle, facilitating bubble attachment to the surface [34]. Choosing the appropriate collector is essential for achieving effective separation via froth flotation. Frothers are substances that play a crucial role in stabilising air bubbles, ensuring their even dispersion within the slurry and the formation of a robust froth layer that can be removed without bubble collapse [35]. Modifiers such as pH regulators are substances that influence how collectors adhere to mineral surfaces. They can either enhance the adsorption of a collector onto a specific mineral or hinder the adsorption of a collector onto a mineral [36].

## 1.4 Structural Aspects

The  $\text{Fe}_5\text{Ni}_4\text{S}_8$  structure shown in Figure 1.3 was generated by Molala et al. (2024) using the universal cluster expansion (UNCLE) method [37]. In the determination of the structure, the initial structure was  $\text{Ni}_9\text{S}_8$  and the Fe atoms were inserted on the Ni sites. The  $\text{Fe}_5\text{Ni}_4\text{S}_8$  structure was found to be the most stable since it had the lowest heat of formation with a space group of  $P4_2/nmc$  [38]. The  $\text{Fe}_5\text{Ni}_4\text{S}_8$  mineral forms a tetragonal structure. The lattice dimensions were found as  $a = b = 7.024 \text{ \AA}$  and  $c = 9.934 \text{ \AA}$ , and the angles between the cell faces were  $\alpha = \beta = \lambda = 90^\circ$ . Within its unit cell, the Fe atoms occupy the octahedral M (O), while both Ni and Fe occupy the tetrahedral M (T) sites. The octahedral M (O) metals are coordinated to face-capping sulphurs, while the tetrahedral M (T) metals are coordinated to the linked sulphurs S (l) and the face-capping sulphurs. The linked sulphurs S (l) are 4-coordinated, while the face-capping sulphurs S (f) are 5-coordinated.

Table 1.1 : The atomic positions in pentlandite  $\text{Fe}_5\text{Ni}_4\text{S}_8$  crystal structure from CE.

Property		Value		
Formula		$\text{Fe}_5\text{Ni}_4\text{S}_8$		
Unit cell length (a=b)		7.024 Å		
(c)		9.934 Å		
Cell angles ( $\alpha=\beta=\gamma$ )		90°		
Space-group		P4-2nmc		
Atoms	Position	X	Y	Z
Fe1	(2a)	0.750	0.250	0.750
Fe2	(8g)	0.250	0.500	0.624
Ni1	(8g)	0.250	0.000	0.876
S1	(4d)	0.250	0.250	0.000
S3	(8f)	0.000	0.000	0.250

The lattice parameters in Table 1.1 are for the un-relaxed structure of  $\text{Fe}_5\text{Ni}_4\text{S}_8$ . The bulk structure of  $\text{Fe}_5\text{Ni}_4\text{S}_8$  consist of 36 atoms.

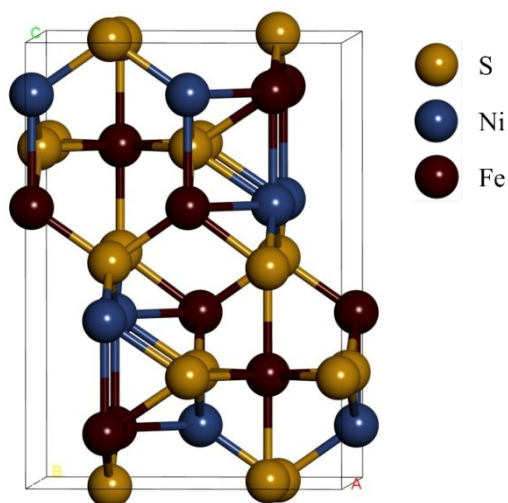


Figure 1.3: The unit cell of  $\text{Fe}_5\text{Ni}_4\text{S}_8$  bulk [38].

## 1.5 Significance of the Study

This research will have a significant impact in the mining industry, in particular the mineral processing industry, in terms of attaining high selective separation and recovery of the pentlandite minerals utilising innovative collectors for beneficiation of nickel. The bonding mechanisms and fundamental understanding of these collectors' interactions with base metal sulphides (BMSs) minerals such as pentlandite will further assist the scientific community in the design and development of reagents for mineral processing. This study will also provide insight into implementation tests and the application of these collectors to additional minerals through publications.

## 1.6 Rationale, Objectives and Research questions

### 1.6.1 Rationale

The proposed study will focus on the pentlandite mineral to investigate its surface adsorption behaviour with various collectors to improve its floatability. This will take advantage of the recently developed technology of computational algorithms that offers hope to investigate the complex surfaces at an affordable cost and efficiency where a collector can be adsorbed on the surface. In the current study, heterocyclic MBTNa, s-triazine, thionocarbamate and S-allyl dithiocarbamate collectors will be tested to examine the best-performing collector. Due to the demands of nickel, substantial effort has been put into the recovery of pentlandite. Enhancing the separation of these minerals from the gangue in the extracted ores remains a problem. The flotation of pentlandite and nickel ore has always been performed using various collectors such as xanthates, dithiophosphates and dithiocarbamates. These collectors were not so effective for pentlandite recovery due to their low selectivity. The chalcopyrite ( $\text{CuFeS}_2$ ) collectors have not been utilised for pentlandite; pentlandite has two metals similar to chalcopyrite. This implied that the chalcopyrite collectors might be useful to selectively attach to the nickel of pentlandite mineral. The current research focuses on utilising the density functional theory with dispersion correction (DFT-D) to investigate the adsorption of MBTNa, SDTBAT, IPDETC and ADEEDTC collectors on dry  $\text{Fe}_5\text{Ni}_4\text{S}_8$  mineral surfaces. The Vienna Ab-initio Simulation Package (VASP) code was adopted. The surface study will investigate and determine the most stable surface of the pentlandite, which will be utilised for adsorption.

The surface and adsorption energies will be utilised to explore the surface interaction. More crucially, the chemistry of the interaction between the collectors and surfaces will be described by exploring the electronic signature, behaviour of DOS and atomic charges. These are crucial in order to determine the preferred surface and adsorption site for possible maximum recovery. The study will start by investigating the bulk and the surfaces prior to adsorption. In addition, the DOS band, and atomic charges will be computed for the bulk, clean surface and adsorbed surfaces.

### 1.6.2 Objectives

The objectives of the study are to:

- i. perform full geometry optimisation of bulk models,

- ii. cleave the low index (100), (110), (111), (224) and (311) surfaces at different terminations,
- iii. determine the most stable surface termination that is less reactive (surface energy),
- iv. calculate electronic structures for the stable surface,
- v. investigate the influence of heterocyclic (MBT), novel triazine (SDTBAT) and thionocarbamate (IPDETC and ADEDEC) collectors on the stable surface,
- vi. determine surface properties: adsorption energy and bond lengths,
- vii. describe the reactivity behaviour from electronic structures of surfaces: DOS, charge density difference and Bader charges.

### **1.6.3 Research questions**

- i. What is the most stable surface for  $\text{Fe}_5\text{Ni}_4\text{S}_8$ ?
- ii. Which collector among heterocyclic (MBT), novel triazine (SDTBAT) and thionocarbamate (IPDETC and ADEDEC) will best improve the floatability of  $\text{Fe}_5\text{Ni}_4\text{S}_8$ ?
- iii. Will the collectors be selective towards the Fe or Ni atoms?
- iv. What is the electronic behaviour of the surface adsorbed with collectors?

## **1.7 Outline of the dissertation**

The following chapters will look into discussions and results obtained while doing the project and the interpretation thereof.

This dissertation gives a report on the study of surfaces and electronic properties of the  $\text{Fe}_5\text{Ni}_4\text{S}_8$  pentlandite using first-principles DFT-D methods.

The dissertation is partitioned into five chapters:

Chapter 1 outlined the background based on the theory and different techniques that have been used previously on studies of these minerals, the literature review and the flotation process. We also review the crystal structure analysis of the  $\text{Fe}_5\text{Ni}_4\text{S}_8$  pentlandite mineral. Finally, the rationale and objectives of this work were stated.

Chapter 2 covers the techniques that have been employed in the current study: DFT-D, the plane-wave pseudopotential method and Vienna Ab-initio Simulation Package (VASP) code. Firstly, the chapter introduces number-first principle techniques; secondly, the DFT for calculating geometry optimisation is described; thirdly, approximation methods such as LDA,

GGA and dispersion correction are described; fourthly, surface preparations and lastly, the background for calculated electronic properties such as density of states and Mulliken population analysis.

Chapter 3 is concerned with optimisation of the bulk and surfaces and their electronic structures.

Chapter 4 is concerned with the results and discussions for collectors' adsorptions on the  $\text{Fe}_5\text{Ni}_4\text{S}_8$  pentlandite surface and their electronic structures and comparison of adsorption energies.

Chapter 5 gives the summary, conclusion, recommendations, future work and appendix. Finally, the bibliography, which helps give insight into the analysis of the work, is listed, and papers presented at conferences are given in appendices.

# **CHAPTER 2**

## **Density Functional Theory Method**

## 2.1 Density Functional Theory (DFT)

The computation methods utilised in this study are described in this section. Experimentally and conceptually, computational simulations examine the structural, surface, and electrical characteristics of metals. The technique was utilised to foresee the actual scenario by adding physical systems as models of unique structures in solid state physics, chemistry, and materials science [39]. To examine surface attributes and model the mineral  $\text{Co}_9\text{S}_8$  structures, all calculations were carried out utilising the initial idea of quantum mechanical DFT and the parameterisation approach of quantum mechanical simulation. The Schrödinger equation is solved using the pseudopotential plane-wave (PW) approach and quantum mechanical simulation.

The electronic structure of multi-body systems, notably atoms, molecules, and condensed phases, is studied using Density Functional Theory (DFT) [40]. DFT might also be used to characterise characteristics of metals, semiconductors, and insulators in their ground states. DFT has long been the most popular method for accurately assessing a wide variety of physical properties. The characteristics of some electron systems may be computed using the DFT using a functional property, i.e., the function of another function, in this case the spatially determined electron density. Since the 1970s, this idea has been widely used in computations. It's employed in computations for solid state physics [41].

It's used in solid-state physics calculations. This theorem may be generalised to the time-independent domain to develop the functional theory of time-dependent density that can be utilised to characterise excited states [42]. The theoretical underpinning of DFT was verified by the two Hohenberg-Kohn (H-K) theorems, despite its theoretical origins in the Thomas-Fermi model. The first H-K theorem states that an electron density with just three spatial coordinates may uniquely determine the ground state features of a multi-electron system. This allows the multi-body issue of  $N$  electrons with  $3N$  spatial dimensions to be reduced to 3 spatial coordinates using the electron density functional. This theorem may be extended to the time-independent domain to construct the functional theory of time-dependent density that can be used to characterise excited states. The first Hohenberg-Kohn theorem states that the density of any structure determines all of the scheme's ground-state features, that is:

$$E = E[\rho], \tag{2.1}$$

Where  $E$  is the ground state energy and  $\rho$  is the ground-state density of the system. The second H-K theorem demonstrates that a variation principle exists for the above-mentioned functional power density  $E[\rho]$ . If  $\rho'$  is not the ground state density of the above system, then:

$$E[\rho'] > E[\rho], \quad 2.2$$

The second H-K theorem determines functional energy for the scheme and shows that the true ground-state electron density reduces this functional energy. The intractable multi-body problem of interacting electrons in static potentials is reduced within Kohn-Sham (K-S) DFT to a tractable problem of non-interacting electrons moving within an efficient potential. The successful potential includes the internal potential and the results of the Coulomb electron interactions, which are the interactions between return and correlation. The latter two relationships within K-S DFT are difficult to model. Non-interacting systems are comparatively easy to solve, as the wave function can be interpreted as an orbital Slater determinant [43].

The total energy functional of Kohn-Sham can be written for a set of dual electronic states as follows:

$$E = \{\psi_i\} = 2 \sum_i \left( \frac{-\hbar}{2m} \right) \nabla^2 \psi_i d^3r + \int V_{\text{ion}}(r) n(r) d^3r + \frac{e^2}{2} \int \frac{n(r)n(r')}{|r-r'|} d^3r d^3r' + E_{\text{xc}}[n(r)] + E_{\text{ion}}(\{R_I\}) \quad 2.3$$

And  $E_{\text{ion}}$  is the Coulomb energy connected with ion interactions at locations  $\{R_I\}$ ;  $V_{\text{ion}}$  is the complete static potential of the electron-ion;  $\rho(r)$  is the electronic density provided by:

$$n(r) = 2 \sum_i |\psi_i(r)|^2, \quad 2.4$$

Where  $E_{\text{xc}}[n(r)]$  is the exchange-correlation functional. Determine the set of wave functions that minimises the functionality of the Kohn-Sham energy. These are provided by the Kohn-Sham equations self-consistent solutions:

$$\left[ \frac{-\hbar}{2m} \nabla^2 + V_{\text{ion}}(r) + V_{\text{H}}(r) + V_{\text{xc}}(r) \right] \psi_i(r) = \varepsilon_i \psi_i(r), \quad 2.5$$

And  $\psi_i$  is the wave function of electronic state  $i$ ,  $\varepsilon_i$  is the Kohn-Sham eigen value and  $V_{\text{H}}$  is the Hartree potential of the electrons [43]. The exchange-correlation as a function of the electron spin density  $n(r)$  within K-S DFT must be approximated [42]. The ground state energy of the system can be written as:

$$E_0 = \min_{\rho} \rightarrow N (F[\rho] + \int \rho(\mathbf{r}) V_{\text{Ne}} d\mathbf{r}), \quad 2.6$$

Where  $F[\rho]$  is the universal function containing kinetic power contributions, classical Coulomb interaction and the non-classical part:

$$F[\rho] = T[\rho] + J[\rho] + E_{ncl}[\rho], \quad 2.7$$

If  $J[\rho]$  is known, then the expressions  $T[\rho]$  and  $E_{ncl}[\rho]$  have to be found. The Thomas-Fermi offers an illustration of the functional theory of density. Then its efficiency is bad due to the poor kinetic energy approximation. Kohn and Sham suggested calculating the non-interacting system's kinetic energy with the similar density as the interacting system using [43] the following equation:

$$TS = \frac{-1}{2} \left\langle \int_i^N \langle \psi^i | \nabla^2 | \psi^i \rangle \right\rangle \text{ and } \rho_S(\mathbf{r}) = \int_i^N \langle \psi^i | \sum | \psi^i(\mathbf{r}, s) |^2 = \rho(\mathbf{r}), \quad 2.8$$

Hence,  $\psi^i$  is the non-interacting orbitals of the system. TS is not comparable to the system of the true kinetic energy. According to Kohn and Sham, the separation of the functional  $F[\rho]$  was introduced:

$$F[\rho] = TS[\rho] + J[\rho] + E_{xc}[\rho], \quad 2.9$$

$E_{xc}$  is the exchange correlation energy, which can be defined by,

$$E_{xc}[\rho] = (T[\rho] - TS[\rho]) + (E_{ee}[\rho] + J[\rho]), \quad 2.10$$

### 2.1.1 Local density approximation

The local density approximation (LDA) is the cause of all approximate exchange correlation functionals. The functional only depends on the local density at a given point, while the GGA depends on the local density and its gradient [44]. Electrons pass inside the LDA on a positive distribution of the background charge. There is a uniform electron gas at the core of this model. The LDA explains the properties of the ground state well (lattice constants and bulk moduli, etc.). The Hohenberg-Kohn theorem offers some inspiration to use approximate methods to explain the energy of exchange correlation as a function of the density of electrons. LDA is the easiest exchange correlation used to explain electronic device capacity. According to Dirac, the exchange functional was introduced to the Slater exchange. The central idea of LDA is the presumption that we can write  $E_{XC}$  in the following form of:

$$E_{XC}^{LDA}[\rho] = \int \rho(\mathbf{r}) \varepsilon_{XC}(\rho(\mathbf{r})) d\mathbf{r} \quad 2.11$$

Hence,  $\varepsilon_{xc}(\rho(\mathbf{r}))$  is the exchange-correlation energy per particle of a uniform electron gas of density  $\rho(\mathbf{r})$ , and the probability  $\rho(\mathbf{r})$  weights with the energy per particle showing an electron at the position. The quantity  $\varepsilon_{xc}(\rho(\mathbf{r}))$  can be further split into exchange and the contributions of correlations:

$$E_{XC}(\rho(\mathbf{r})) = \varepsilon_{XC}(\rho(\mathbf{r})) + \varepsilon_C(\rho(\mathbf{r})), \quad 2.12$$

In the sense that the quantum mechanical problem is solved without any arbitrary or device-dependent parameters, the local density approximation is a first-principle solution. The LDA assumes that the functional exchange-correlation power is strictly local [45].

## 2.1.2 General Gradient Approximation

The GGA Modify K-S energy partitioning to obtain a non-local Hamiltonian, but it is still local [46]. The first logic step to go to the LDA is by supplementing the density with the gradient of charge density information,  $\nabla\rho(\mathbf{r})$ , to report for non-homogeneity of true electron density.

Then the exchange-correlation energy termed generalized gradient approximations can be written as:

$$E_{XC}^{GGA}[\rho\alpha, \rho\beta] = \int f(\rho\alpha, \rho\beta, \nabla\rho\alpha, \nabla\rho\beta) d\mathbf{r}, \quad 2.13$$

Hybrid functional was successfully introduced by Alex Becke in 1993 to improve the results within the exchange functional GGA:

$$E_{XC}^{hyb} = \alpha E_X^{KS} + (1 - \alpha)E_{XC}^{GGA}, \quad 2.14$$

Where the  $E_X^{KS}$  exchange is calculated with the wave function KS,  $E_{XC}^{GGA}$  it is an appropriate GGA, and  $\alpha$  is a fitting parameter. The exchange-correlation energy for the generalised gradient approximation improves upon the local spin density approximations (LSDA) description of solids and atoms [47]. It improves total energies and structural energy differences, and it expands and weakens the bonds [48]. The GGA functions are precise and provide very decent results for molecular geometries and ground-state energies and are expressed in Perdew-Wang terms, theoretically more precise than the functional and meta-GGA functions of the GGA [47]. Other notable DFT functionals are hybrid meta GGA, hybrid and double functional. GGA-PBE is one of the essential functions of trade correlation for solid calculation [49].

### 2.1.3 Dispersion corrections to DFT

Van der Waals dispersion (vdW) interactions are long-range, non-local in nature, and can be crucial for understanding and predicting structure and energetics in many systems. Weakly bonded dimers, molecules on surfaces, and molecular crystals are a few examples of such systems. Traditional local and semi-local exchange and correlation functionals in density functional theory are unable to account for these interactions due to their intrinsic non-locality (DFT). Recent years have seen a plethora of proposed solutions, which range from high-level wave-function techniques within various embedding schemes, via exchange-correlation (xc) functional explicitly constructed to seamlessly include dispersion interactions such as Van der Waals density functional (vdWDF) to the electron correlation resulting from applying the random-phase approximation in the context of the adiabatic-connection dissipation fluctuation theorem. Particularly for large systems or more extensive scans of the huge configuration spaces representative of modern materials science, much more modest semi-empirical schemes that correct at least for the long-range vdW interaction enjoy increasing popularity. In these so-called dispersion-corrected DFT (or short DFT-D) [45, 46] approaches are considered approximately by adding a pairwise interatomic  $\frac{C_6}{R^6}$  term to the DFT energy. At distances below a cut-off, motivated by the vdW radii of the atom pair, this long-range dispersion contribution is heuristically reduced to zero by multiplication with a short-range damping function.

London introduced a number of ideas and methods that are relevant to any two systems that are separated; although anisotropic effects may also be present in more complicated cases, the underlying principles are the same. For two widely separated molecules,  $A$  and  $B$ , with ground state wavefunctions  $\psi_0^A$  and  $\psi_0^B$ , the energy correction to second order perturbation theory, representing polarisation interactions, is given by:

$$E_{pol} = - \sum_{n \neq 0 \wedge m \neq 0} \frac{|\psi_0^A \psi_0^B | \hat{V} | \psi_0^A \psi_0^B |^2}{(E_n^A - E_0^A) + (E_m^B - E_0^B)}, \quad 2.15$$

Where  $n \neq 0 \wedge m \neq 0$  implies that  $n$  and  $m$  cannot be equal to 0 at a time, and  $\psi_0^{A/B}$  are excited states. The polarisation energy can be expressed as the sum of two parts: the induction energy and the dispersion energy:

$$E_{pol} = E_{ind} + E_{disp}. \quad 2.16$$

This is, in fact, the definition of dispersion.

The induction energy is given by:

$$E_{ind} = - \sum_{m \neq 0} \frac{|\psi_0^A \psi_m^B| \hat{V} |\psi_0^A \psi_0^B|^2}{E_m^B - E_0^B} - \sum_{n \neq 0} \frac{|\psi_0^A \psi_0^B| \hat{V} |\psi_0^A \psi_n^B|^2}{E_n^A - E_0^A}, \quad 2.17$$

The first term in the sum represents the electrostatic interaction of molecule  $A$  in its ground state with density  $\rho_{00}^A(\mathbf{r})$ , with molecule  $B$  in an excited state with density  $\rho_{m0}^A(\mathbf{r})$ . The second term is defined in the same manner. For overlapping charge distributions, the induction interactions are crucial; however, due to their exponential decay with distance for non-polar atoms or molecules, they carry no significance at large distances [52].

For the same molecules  $A$  and  $B$ , the dispersion part of the energy for the special case of two distant hydrogen atoms is defined by:

$$E_{disp} = - \sum_{n \neq 0 \wedge m \neq 0} \frac{|\psi_0^A \psi_0^B| \hat{V} |\psi_0^A \psi_0^B|^2}{(E_n^A - E_0^A) + (E_m^B - E_0^B)} \quad 2.18$$

More generally, following a perturbative approach according to London's work by using Eq. 2.18 for molecules or fragments of electronic density  $A$  and  $B$  and performing a multipole expansion for the perturbation Hamiltonian  $\hat{V}$ , the energy of vdW interactions can be estimated. Including higher-order terms in the multipole expansion for  $\hat{V}$ , the dispersion energy can be written as:

$$E_{disp} = - \sum_{n=6}^{\infty} \frac{C_n}{R^n} \quad 2.19$$

Note that  $n = 6$  is the first non-vanishing term in the expansion is valid for general systems. The higher-order terms in the expansion in Eq. 2.19 can contain either exclusively even powers (for spherically symmetric systems) or both even and odd powers for more complex systems like molecules. As previously mentioned, the first term of Eq. 2.19 is the basis for a number of methods aiming to compute vdW interactions which involve determining appropriate expressions for the  $C_6$  coefficients and pairwise-summing over interacting non-overlapping fragments of density in the system. Since the initial assumption is that the two interacting systems are well separated, electron exchange was therefore disregarded as was done for the straightforward case of hydrogen atoms, making it impossible to use the perturbative types of methods demonstrated here for overlapping fragments (molecules or atoms). There are various dispersion methods implemented, such as Grimme [53], Tkatchenko and Scheffer [54], the many-body dispersion and Ortmann-Bechstedt-Schmidt. The choice of the dispersion function is surely dependent on the system under study.

## 2.2 Plane-wave Pseudopotential Method

The variational self-consistent solution to the functional theory of density may be calculated with accuracy using the pseudopotential plane-wave methodology. It may be used in big systems with periodic boundary conditions in three dimensions. This approach extends the wave function in terms of the plane-wave basis, which results in a good pseudopotential representation of the crystal ions.

### 2.2.1 Plane-wave Basis

The use of the plane wave base set has several benefits, including the ease of the base function, which has no assumptions about the shape of the solution, the lack of base set superposition errors, and the ability to properly compute the forces on the atoms [55]. It necessitates the extension of the electrical wave function of the system. The plane-wave pseudopotential approach is a solid tool for studying material characteristics. Bloch's theorem permits electronic wave functions to be enlarged in terms of the plane wave, which is a fair explanation of the plane-wave basis technique [56]. According to Bloch's theorem, the expression of electronic wave functions for periodic solids and the problem, such as atoms and surfaces according can be as follows:

$$\psi_i(\mathbf{r}) = e^{i\mathbf{k}\cdot\mathbf{r}} F_i(\mathbf{r}), \quad 2.15$$

This enables us to express crystal wave functions in terms of plane waves  $F_i(\mathbf{r})$ , which may be expressed as:

$$F_i(\mathbf{r}) = \sum_{\vec{G}} C_{i,G} e^{i\mathbf{G}\cdot\mathbf{r}}, \quad 2.16$$

As a result,  $G$  is the periodic cell's reciprocal lattice vectors. The following is how each electrical wave function may be written:

$$\psi_{k_i}(\mathbf{r}) = \sum_G C_{i,K+G} e^{i(\mathbf{k} + \mathbf{g})\cdot\mathbf{r}}, \quad 2.17$$

Where  $C_{i,K+G}$  are the plane wave coefficients, which are fully dependent on the specific kinetic energy,

$$\left(\frac{\hbar^2}{2m}\right) |\mathbf{K} + \mathbf{G}_c|^2, \quad 2.18$$

The kinetic energy cut-off is controlled by the parameter above, which governs the convergence of expansion. The plane-wave basis set is constrained to a sphere in reciprocal space shown in terms of energy cut-off,  $E_{\text{cut}}$ , and the kinetic energies are less than or equal to a certain cut-off energy for all values of  $G$ , as follows:

$$\left(\frac{\hbar^2}{2m}\right) |K + G_c|^2 \leq E_{\text{cut}}, \quad 2.19$$

The energy cut-off is determined by raising the size of the cut-off until the total energy is converged to the point where precision is required [47]. More quickly variable properties may be specified as the number of plane waves increases, and an endlessly large number of fundamental sets can be easily created. Finite bases are obtained by applying finite cut-off energy to the discrete plane-wave basis set. To avoid mistakes in the calculation of total energy, the cut-off energy should be raised before the measured energy has converged. A denser range of  $k$ -points must be employed to reduce mistakes and ensure satisfactory convergence.

## 2.2.2 Pseudopotential Method

The pseudopotential technique is a fast potential approach for replacing the all-electron atomic potential while excluding core states and valence electrons described by the pseudo-wave function. The key characteristic of the valence electron travelling through a crystal, including a relativistic effect, is characterised as a weak pseudopotential that substitutes the electron core and the attractive Coulomb potential within the ionic core [57]. The pseudo-valence electron and pseudo-ion cores are replaced by the original solid. The pseudo electron has a lower potential within the core region, but it has the same potential outside the core region as the original electron.

The ionic potential ( $Z/r$ ), the function of the valence wave ( $\psi_v$ ), the corresponding pseudopotential function of  $V_{\text{pseudo}}$  and pseudo wave ( $\psi_{\text{pseudo}}$ ) are shown in Figure 2.1. The utilisation of the pseudopotential approximation method had an advantage, since it allows the electronic wave function to expand using a smaller number of a plane-wave basis states. The most general form of pseudopotential is:

$$V_{\text{NL}} = \sum_{lm} |lm\rangle V_i \langle lm|, \quad 2.20$$

The spherical harmonics  $|lm\rangle$  and  $\langle lm|$ , and  $V_i$  is the pseudopotential for angular momentum  $l$ , have no influence on the electronic wave function since this operator decays the wave

function into spherical harmonics, which are then multiplied by the appropriate pseudopotential  $V_i$ . For all rotational momentum components, the local pseudopotential employs the same potential.

The ultrasoft pseudopotential proposed by Vanderbilt is used in the plane-wave computations [58]. In this technique, the pseudo-wave functions are allowed to be soft inside the core area. The term ultrasoft pseudopotential (USP) refers to a group of atoms that includes transition metals. In this research, we utilise the USP in the CASTEP software [45] to calculate total energy.

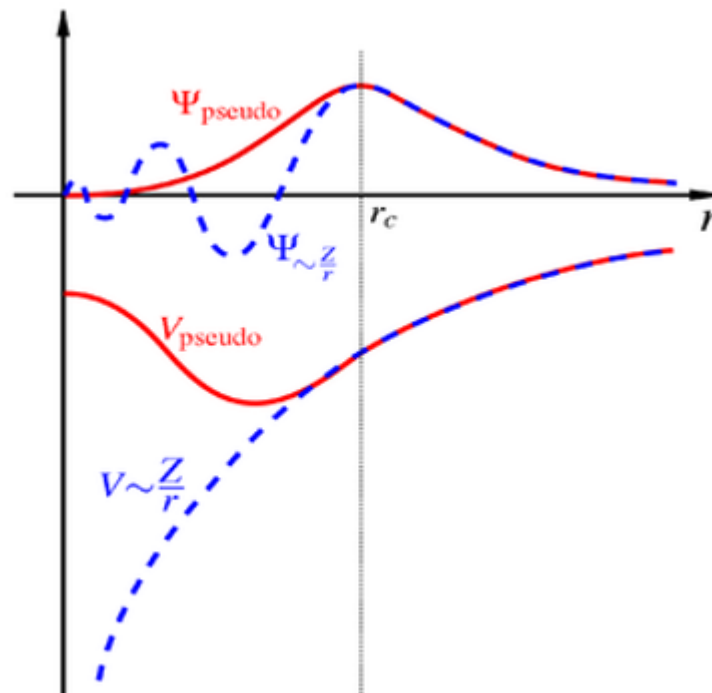


Figure 2.1 : The relation of both the electron potential of the all-electron potential of the nucleus (blue dash lines) and the pseudopotential potential of a Coulomb wave (red solid lines). The function of the pseudo-wave, the real, and potential corresponds to the radius  $r_c$  above [44].

### 2.2.3 Projector Augmented Wave Method

Within the context of DFT, this work employs the projector augmented wave (PAW) method as implemented in the CASTEP code, which has been shown to deliver dependable results for the electronic and structural properties of different solids. The PAW approach is powerful and has been used efficiently, and works like pseudopotentials in many respects. The technique has a close association with the ultrasoft pseudopotentials, but it also makes it possible to quantify the complete wave functions, including the main electron wave functions. The complete wavefunctions are transformed into auxiliary wavefunctions in this

process. In a plane wave base, the auxiliary functions can be extended reasonably quickly, while atomic wave functions complement the complete wave functions. This assumes the approximation of the frozen core but is much more transferable than pseudopotentials.

## 2.2.4 Ultrasoft Pseudopotential

Ultrasoft pseudopotential covers a wide range of atoms, including transition metals (USP). In 1990, Vanderbilt University developed a pseudopotential known as ultrasoft pseudopotential. Kleinman-generalisation Bylander's (Vanderbilt D., 1990) makes extensive use of contemporary pseudopotential computations. The approach is a major departure from norm-conserving pseudopotentials because ultrasoft pseudopotentials yield much smoother pseudo-wave functions. The pseudo wavefunctions are supposed to be identical to all electron wavefunctions outside the radius, as with the norm-conserving pseudopotentials, but they are allowed to be as soft as possible inside the radius. The constraint of maintaining the standard has been removed once more, although this has resulted in several issues. However, because huge radius values can be used in their arrangement, the ultrasoft pseudopotential can still lower the plane cut-off required in computations.

There are two types of issues that develop because of this. To begin with, the pseudo wavefunctions in the interstitial are like all-electron wavefunctions (and have the same standard), but they are not necessarily normalised because they have a different standard inside the topological complexity. Second, computing  $\rho$  as with standard-conserving pseudopotential does not yield the pseudo charge density, resulting in an inaccurate total charge. A third, but less important, problem is that by connecting the norm-conservation, the resulting pseudopotentials can become less transferrable. However, Vanderbilt pseudopotentials were proposed for use in large-scale calculations, where the cost of manufacturing pseudopotentials is small relative to the cost of the calculations (Vanderbilt D., 1990). The electron density is separated into two parts: a smooth component that stretches across the unit's cell and a hard section in the core area. The ultrasoft pseudopotential is better than the standard pseudopotential.

## 2.3 K-points sampling

In a bulk solid, electronic states are permitted at specific k-points determined by the boundary conditions of the system. The density of these allowed k-points is proportional to the volume of the solid. The infinite number of electrons in the solid corresponds to an

infinite number of k-points, though only a finite number of electronic states are occupied at each k-point.

The Bloch theorem simplifies the problem of calculating an infinite number of electronic wavefunctions by reducing it to calculations at a finite set of k-points. Each occupied state at these k-points contributes to the electronic potential in the solid. While, in principle, an infinite number of calculations would be required to compute this potential, the similarity of electronic wavefunctions at closely spaced k-points allows representation of a region of k-space with just a single k-point. This makes it possible to calculate the electronic potential and the total energy of the solid using wavefunctions at only a finite number of k-points.

Accurate approximations of the electronic potential for filled electronic bands can be achieved using special sets of k-points, with methods developed by Chadi and Cohen [59] as well as Monkhorst and Pack being the most common. These approaches allow the electronic potential and total energy of insulators to be computed with calculations at a small number of k-points. Metallic systems, however, require a denser sampling of k-points to accurately define the Fermi surface.

The computational cost of densely sampling k-space increases linearly with the number of k-points in the Brillouin zone. To reduce this cost, density functional codes use a finite sampling of k-points to approximate k-space integrals. Special k-point schemes, particularly the widely used Monkhorst-Pack method, are designed to achieve the desired accuracy with the minimal number of k-points, thereby optimising computational efficiency [60].

## 2.4 VASP implementation

The Vienna *Ab-initio* Simulation Package (VASP) [61] is a widely used electronic structure code for studying solids, surfaces, and interfaces. It also enables *ab-initio* quantum mechanical molecular dynamics (MD) simulations using a plane wave basis set in conjunction with Vanderbilt pseudopotentials or the projector augmented wave (PAW) method. The interaction between ions and electrons is modelled using ultrasoft Vanderbilt pseudopotentials (US-PP) or the PAW approach [62]. VASP is based on density functional theory (DFT) but allows for the incorporation of post-DFT corrections, including hybrid functionals combining DFT with Hartree-Fock exchange, many-body perturbation theory, and dynamical electronic correlations within the random phase approximation [63].

These techniques significantly reduce the number of plane waves required per atom for elements such as transition metals and first-row elements. Forces and stresses can be easily computed in VASP, enabling relaxation of atoms to their instantaneous ground state.

The PAW method, developed by Blöchl [62], is a very powerful tool for performing electronic structure calculations within the framework of density functional theory [57, 58], combining some of the best features of pseudopotential and all-electron approaches. VASP employs efficient matrix diagonalisation and Pulay/Broyden charge density mixing techniques, circumventing issues inherent in the original Car-Parrinello method, which relied on simultaneously integrating electronic and ionic motion equations.

For the Fe<sub>5</sub>Ni<sub>4</sub>S<sub>8</sub> bulk structures, VASP was used to calculate structural relaxation, structural properties, elastic and mechanical characteristics, vibrational properties, electronic properties, and surface properties. These calculations were performed self-consistently using DFT within the generalised gradient approximation (GGA) functional. Electronic wavefunctions were expanded in a plane-wave basis set with periodic boundary conditions.

## 2.5 Theoretical background of calculated properties

### 2.5.1 Density of states

The density of states (DOS) of a system represents the number of available quantum states per energy interval at each energy level. It illustrates how quantum states are distributed within a system. By integrating the DOS over a specific energy range, the total number of states within that range can be determined:

$$N(E) = \int_E^{\Delta E} g(E)dE \quad 2.42$$

Here,  $N(E)$  denotes the carrier density, and  $g(E) dE$  represents the number of states between energy levels  $E$  and  $dE$ . The DOS allows integration with respect to electron energy rather than over the entire Brillouin zone, facilitating the analysis of electronic structures. It provides insights into features like the valence band width, energy gaps in insulators, and the intensity of prominent electronic features, aiding the interpretation of experimental spectroscopic data.

Accurate methods for calculating DOS often use linear or quadratic interpolation of band energies between reference points in the Brillouin zone. The tetrahedron interpolation technique is widely regarded as the most precise and reliable, though it is less compatible with the Monkhorst-Pack grid of special points [66]. In contrast, the VASP code employs a simplified linear interpolation method. This approach uses linear interpolation within parallelepipeds defined by Monkhorst-Pack grid points, followed by histogram sampling of the resulting band energies. In complex minerals, pseudo-gaps may form in the electronic

DOS near the Fermi energy ( $E_F$ ), which can relate to structural stability. Experimental studies by Pierce [67] and Matsuda [68] observed that pseudo-gaps are associated with high resistivity in structurally stable quasicrystals. Several studies have linked pseudo-gap formation directly to structural stability [68]. The density of states is also crucial in evaluating the stability trends of structures with identical compositions near  $E_F$ . According to theory, elements with higher DOS near  $E_F$  are less stable, while those with lower DOS are more stable. Additionally, the element contributing more significantly to the DOS at  $E_F$  is considered the most chemically active or reactive [62,63]. Moreover, the element with the greater contribution at the  $E_F$  is the most active or reactive element.

## 2.6 Charge population analysis

The properties of chemicals and materials are often described in terms of charge transfer between atoms and the presence of ionic charges or electric multipoles on atoms or molecules. Theoretical calculations producing estimates of the electronic charge distribution in the system can, in principle, provide this type of information, but it is not clear how to extract it. However, the atomic charges in molecules or solids are not observables and therefore not defined by quantum mechanical theory. The output of quantum mechanical calculations is a continuous electronic charge density, and it is not clear how one should partition electrons amongst fragments of the system, such as atoms or molecules.

Many different schemes have been proposed; some are based on electronic orbitals (such as Mulliken Population Analysis), and others are based only on the charge density, such as Bader's Atoms in Molecules method. The Mulliken analysis is the most used orbital-based method. It can be applied when basis functions centred on atoms are used in the calculation of the electronic wave functions of the system. The charge associated with the basic functions centred on a particular atom is then assigned to that atom. This can be a fast and useful way of determining partial charges on atoms, but it has the major drawback that the analysis is sensitive to the choice of basis set. A different approach is to focus on the charge density that has been proposed by Bader [71].

The space is then divided into regions by surfaces that run through minima in the charge density. More precisely, at a point on a dividing surface, the gradient of the electron density has no component normal to the surface. The regions bounded by such dividing surfaces are referred to as Bader regions. Because this analysis is based solely on the charge density, it is rather insensitive to the basis set used in the electron wave function calculation and can be used to analyse plane wave-based calculations as well as calculations using atomic basis

functions. In addition, a common complaint about Bader analysis is the computational effort and complexity of the algorithms that have been developed [69, 70]. A commonly used implementation [64, 65, 66] involves finding the critical points of the charge density where  $\Delta\rho = 0$ , followed by the construction of the zero-flux surfaces which intersect these points and then integration of the electronic density within each region. Several refinements have been made since the initial implementation of the method [64, 65, 67]. Most recently, Malcolm and Popelier [77] have used dynamic grid techniques introduced by Silvi and co-workers [69, 70] to effectively treat complicated bonding topology. The current implementations of Bader's analysis are based upon a grid of charge density values where only steepest ascent trajectories confined to the grid points are used to identify the Bader regions [71, 72, 73].

# **CHAPTER 3**

## **Bulk and Surface Modelling**

# Bulk and surface relaxation of Fe<sub>5</sub>Ni<sub>4</sub>S<sub>8</sub>

In this chapter, the DFT-D results of the bulk structure and surface relaxation for Fe<sub>5</sub>Ni<sub>4</sub>S<sub>8</sub> mineral were discussed. Firstly, the bulk convergence test (variation of cut-off and k-points) will be discussed. Secondly, the relaxation of the bulk structures and their electronic properties were explored. Thirdly, the surfaces that will be used in the study and compared to previous studies were presented. Lastly, the electronic structures of surfaces and the adsorption energies formula will be presented.

## 3.1 Convergence of the cut-off energy and k-point sampling

### 3.1.1 Cut-off energy sampling

The method of the plane-wave pseudopotential with generalised gradient approximation to Perdew Burke Ernzerhof (GGA-PBE) [82] within VASP code [61], for the Fe<sub>5</sub>Ni<sub>4</sub>S<sub>8</sub> system was utilised. The cut-off energies must be varied to ensure the adequate accuracy of the total energy before any properties of the system are computed. The single-point energy calculations of Fe<sub>5</sub>Ni<sub>4</sub>S<sub>8</sub> bulk structures were performed at various cut-off energies within the GGA-PBE [82] until a constant minimum energy was obtained within 0.01 eV/Å.

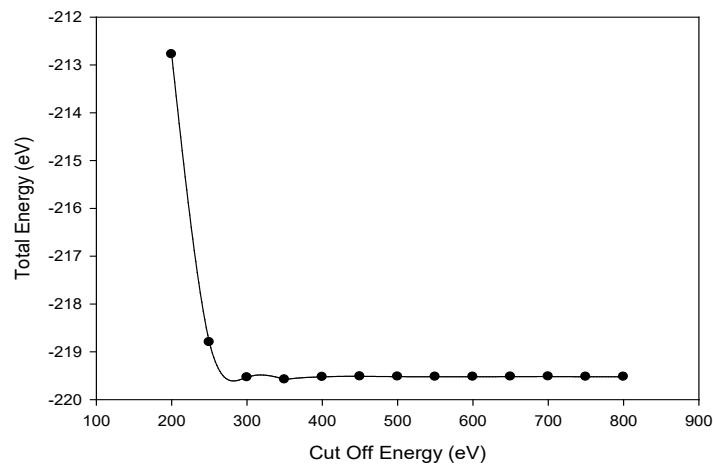


Figure 3.1: Total energy against kinetic energy cut-off of tetragonal Fe<sub>5</sub>Ni<sub>4</sub>S<sub>8</sub> structure.

The graphs of total energy vs cut-off are presented in Figure 3.1 to determine the cut-off energy for the Fe<sub>5</sub>Ni<sub>4</sub>S<sub>8</sub> model. The plot displayed essentially no slope from 300 eV to 800 eV, suggesting that the fluctuation of the total energy was minimal at these points, as shown

in Figure 3.1. The cut-off energy of 400 eV was considered since it was sufficient to converge the bulk total energy at affordable computational costs.

### 3.1.2 Bulk k-points sampling

The number of k-points using the cut-off energy of 400 eV varied. The proper sets of k-points are paramount in obtaining accurate total energies. The Monkhorst-Pack scheme [60] was used to determine the optimal set of k-points to obtain adequate accuracy. The different numbers of k-points from  $1 \times 1 \times 1$  to  $14 \times 14 \times 10$  (Figure 3.2) were varied until the total energy converged to within 0.01 eV/Å. It was noted that the total energy began to converge at the point corresponding to k-points of  $6 \times 6 \times 5$ . The k-point of  $8 \times 8 \times 6$  was adopted. These were found to give accurate results at affordable computational costs.

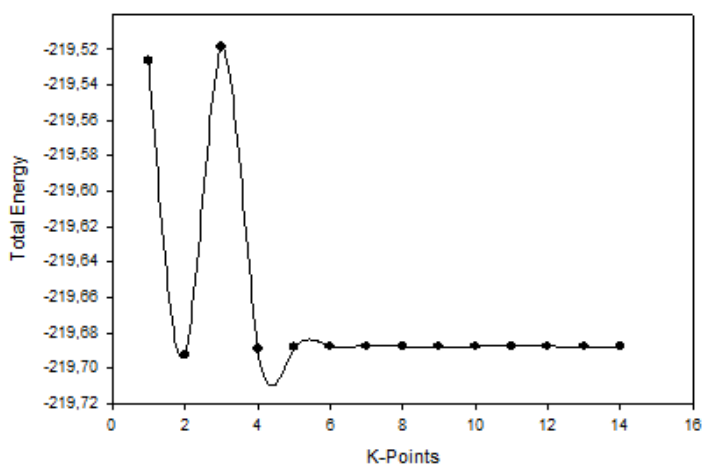


Figure 3.2: Total energy against k-points mesh  $\text{Fe}_5\text{Ni}_4\text{S}_8$  tetragonal structure.

### 3.2 Surface k-points sampling for $\text{Fe}_5\text{Ni}_4\text{S}_8$

It was necessary to establish the optimal number of k-points to be employed in the plane-wave pseudopotential for the surface calculations once adequate kinetic energies (cut-off) and k-points for the bulk models had been acquired. The k-points for surfaces were reliant on the crystal structure, where for a structure with equal or similar a and b lattice, the x and y k-points are equal, and the z direction k-points have a value of unity (1), (e.g.,  $2 \times 2 \times 1$ ). Given that the vacuum slab site is along the z direction, the sampling orders that there should be no compression force along that direction. If the z-direction was given a value greater than unity, the vacuum slab would be disregarded. This will permit unrestricted interaction of the adsorbate in the vacuum. To attain the highest level of precision, an optimal set of special k-

points in the Brillouin zone were chosen using the Monkhorst-Pack scheme of the k-points sampling [66].

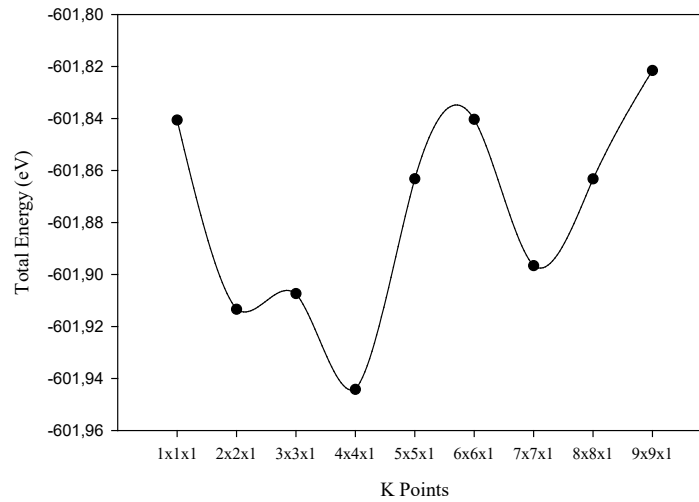


Figure 3.3 : Total energy against k-points mesh  $\text{Fe}_5\text{Ni}_4\text{S}_8$  surface structure.

Different values of k-point mesh parameters varied from  $1 \times 1 \times 1$  to  $9 \times 9 \times 1$  usNi2.pbsing the (311) surface until the total energy change was negligible. The  $4 \times 4 \times 1$  k-points were found to be the appropriate k-points mesh parameters. At this point, it was found that the total energy between two consecutive points converged to within 1.0 meV, which showed that the energy change was minimal (Figure 3.3). These were also adopted to avoid costly computations. Note that the cut-off energy of 400 eV was utilised in obtaining the special k-points for the surfaces, and it will be utilised throughout the study for both bulk and surfaces.

### 3.3 Computational details

The geometry optimisation calculations were performed by employing the density functional theory (DFT). The generalised gradient approximation along with the Perdew-Burke-Ernzerhof functional (GGA-PBE) [82] and the project-augmented-wave (PAW) pseudopotential within the VASP code were adopted [61]. The Grimme [53] dispersion correction method with Becke-Johnson damping D3 (BJ) was adopted. The plane-wave basis set with a cut-off energy of 400 eV was adopted, which demonstrated convergence to within 0.2 meV/atom. The electron configurations considered were Fe-[Ar] $3d^74s^1$ , Ni-[Ar] $3d^{10}$  and S-[Ne] $3s^23p^4$ . The computational optimisations were carried out using the conjugate-gradient algorithm and were considered converged when the force on each ion was less than 0.02 eV/Å. The electron density was considered self-consistent when the change was below  $10^{-6}$  eV. To enhance the convergence of the Brillouin-zone integrations, partial occupancies were

determined using the Methfessel-Paxton smearing method, with a smearing width of 0.2 eV applied to all calculations. The k-points grid of  $8 \times 8 \times 6$  for bulk and  $4 \times 4 \times 1$  for surface structures was generated using the Monkhorst-Pack scheme [83]. However, for surface adsorptions, the k-points of  $1 \times 1 \times 1$  were utilised to reduce the computational costs of these long and intensive adsorption calculations.

The slab depth for each surface model will be determined for each surface as discussed in the next sections. To prevent the adsorbates from interacting with the upper repeating slab model, the vacuum elevation was set to 30.0 Å for all surface models. The surface and adsorption energies will be reported to two (2) decimal places throughout this work model, while total energies (in eV) will be reported to four (4) decimal places to enable future in-depth model comparison and optimisation by other researchers.

### 3.4 Bulk Fe<sub>5</sub>Ni<sub>4</sub>S<sub>8</sub> Pentlandite Properties

In this section the structural properties (lattice constant) and the electronic properties (density of states) for the tetragonal Fe<sub>5</sub>Ni<sub>4</sub>S<sub>8</sub> bulk model were examined. These properties play a huge role in describing the stability and chemical behaviour of the bulk model. The bulk model was optimised, allowing the cell volume, lattice and atomic positions to change, thus relaxing to their ground state energy. The relaxed unit cell bulk structure is shown in Figure 3.4. Table 3.1 displays the obtained lattice parameters in comparison with the experimental lattice parameters. The lattice dimensions were found as  $a = b = 7.020$  Å and  $c = 9.930$  Å, and the angles between the cell faces were  $\alpha = \beta = \lambda = 90^\circ$  with a space group of P4<sub>2</sub>/nmc. Clearly the iron-rich pentlandite was tetragonal, as determined by Molala et al. [84]. It was reported that the multiplication of  $a = b = 7.020 \text{ Å} \times \sqrt{2} = 9.930 \text{ Å}$  which showed that the cluster expansion- generated structure possessed both primitive and conventional lattice parameters [84]. The lattice parameters were in acceptable agreement with previously reported values of 9.991 Å [85] and 9.977 Å [86]. The Fe atoms occupied the octahedral M(O), while both Ni and Fe occupy the tetrahedral M(T) sites within the unit cell. The octahedral M(O) metals were coordinated to face-capping sulphurs, while the tetrahedral M(T) metals coordinated to the linked sulphurs S(l) and the face-capping sulphurs. The linked sulphurs S(l) were 4-coordinated, while the face-capping sulphurs S(f) were 5-coordinated.

The Fe<sub>5</sub>Ni<sub>4</sub>S<sub>8</sub> density of states was analysed from the total density of states (TDOS) and partial density of states (PDOS) as displayed in Figure 3.5. In Figure 3.5, it was observed that the TDOS of Fe<sub>5</sub>Ni<sub>4</sub>S<sub>8</sub> portrayed a metallic behaviour due to no band gap at the Fermi energy

( $E_F$ ). Importantly, the  $E_F$  fell deep into the pseudo gap, which suggested stability. Similar stability has been reported, which was also deduced from the Phonon vibrational stability [24]. The PDOS showed the contribution of each atom in the TDOS. It was noted that in the valence band (VB), both linked and face capping S atoms s-orbitals contributed largely at around  $-15.0$  eV, while the p-orbitals contributed at around  $-8.0$  eV, respectively. It was observed that the S atoms had very little contribution at the  $E_F$ . The S(f) atoms displayed an empty orbital peak at the conduction, which was small for S(l) atoms. This was ascribed to the S(f) coordinated to both M(O) and M(T) metal atoms. The metals dominated that  $E_F$  just below the  $E_F$ , where the Fe(O) displayed a sharp peak, while the Fe(T) displayed a broad sharp peak. The Ni(T) displayed a broad peak also consisting of a sharp peak. It was clear that the Fe(T) dominated strongly at the  $E_F$ , while the Fe(O) and Ni(T) had low states at the  $E_F$ . Significantly, at around  $-7.0$  eV the metals displayed a spd-hybridisation, with largely p-d-orbital mixing within the metals, which also mixed with those of the S atoms.

Table 3.1 The relaxed atomic positions (Wyckoff notation) in pentlandite  $Fe_5Ni_4S_8$  crystal structure [55] from CE.

Property		Value		
Formula		$Fe_5Ni_4S_8$		
Unit cell length (a=b)		$7.020 \text{ \AA} \times \sqrt{2} = 9.930 \text{ \AA}$		
(c)		9.930 $\text{\AA}$		
Cell angles ( $\alpha=\beta=\gamma$ )		$90^\circ$		
Space-group		$P4_2/nmc$		
Atoms	Position	X	Y	Z
Fe1 (O)	(2a)	0.750	0.250	0.750
Fe2 (T)	(8g)	0.250	0.498	0.624
Ni1 (T)	(8g)	0.250	0.002	0.876
S1 (l)	(4d)	0.250	0.250	0.000
S2 (l)	(4c)	0.750	0.250	0.000
S3 (f)	(8f)	0.000	0.000	0.000

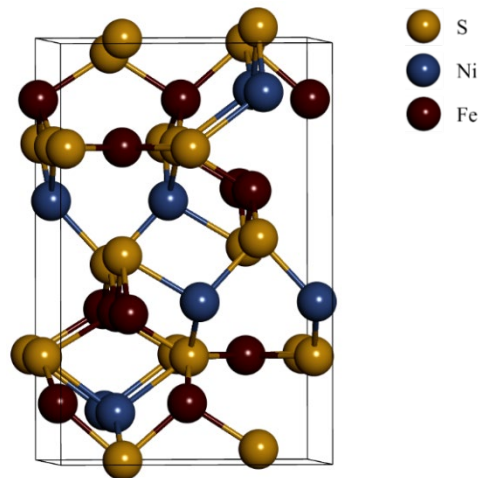


Figure 3.4 : The relaxed unit cell of  $Fe_5Ni_4S_8$  bulk.

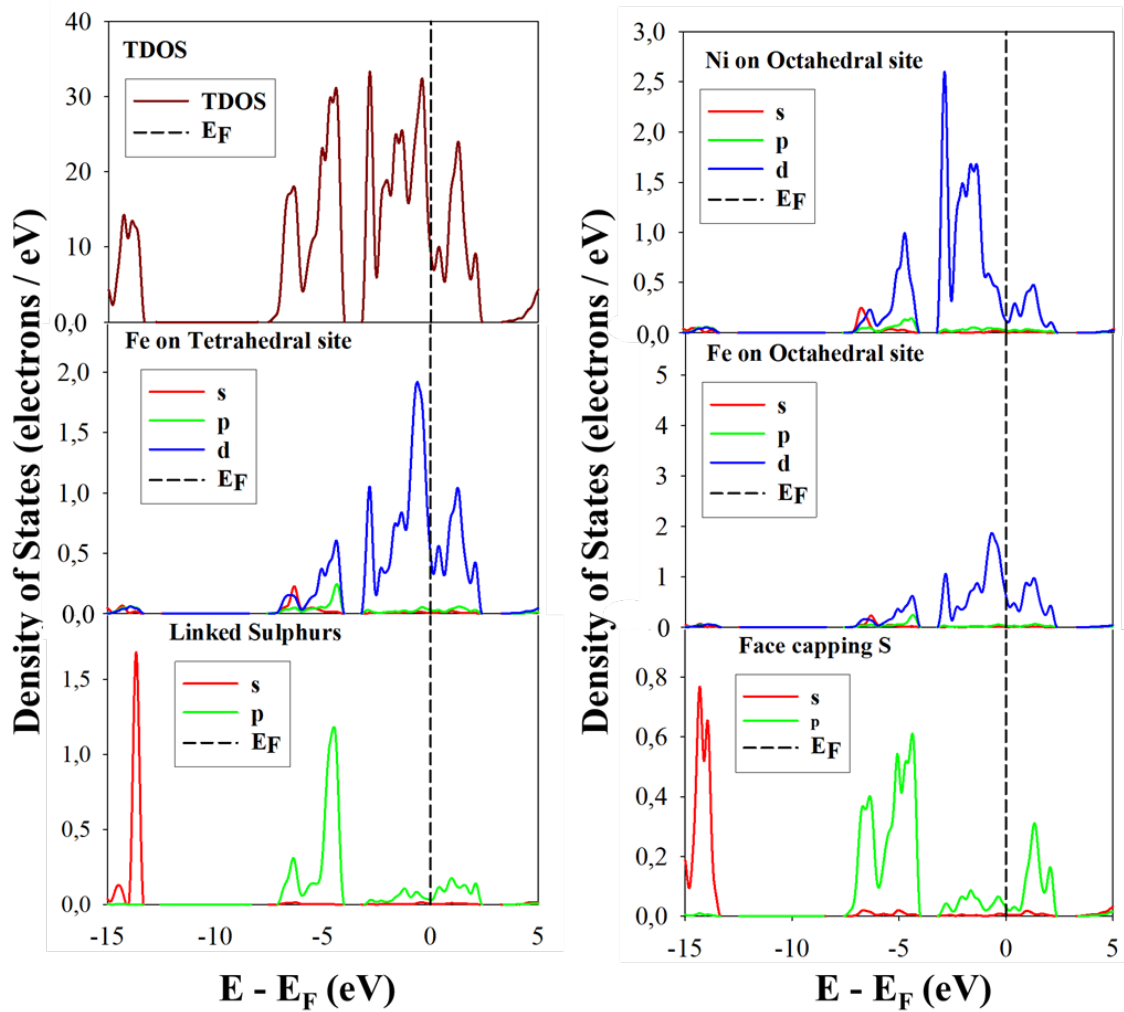


Figure 3.5 : Density of states  $\text{Fe}_5\text{Ni}_4\text{S}_8$  bulk model.

The generated  $\text{Fe}_5\text{Ni}_4\text{S}_8$  structure was characterised using computational X-ray diffraction (XRD) to determine its structural composition, as shown in figure 3.5. The XRD was generated on MedeA software using copper as a source, where it was noted that the (224) and (211) planes were found to have higher intensities. The computational XRD was compared to available experimental XRD of similar structure compounds. Experimentally, the (111), (311), (511) and (440) planes of  $\text{Fe}_5\text{Ni}_4\text{S}_8$  were reported as the highest peak intensities, where the (311) and (440) showed higher intensities to 100 % [87]. Due to the tetragonal structure character of the generated  $\text{Fe}_5\text{Ni}_4\text{S}_8$ , the XRD gave a different plane index compared to experiments. This information will be implemented in the surface studies in the next sections, where the (111), (311), (224) and (211) surfaces will be chosen for further investigation of the most stable surface of  $\text{Fe}_5\text{Ni}_4\text{S}_8$  pentlandite.

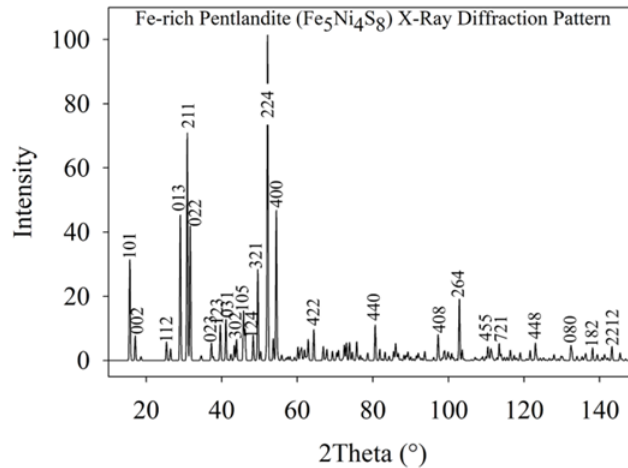


Figure 3.6 : Computational generated XRD for Fe<sub>5</sub>Ni<sub>4</sub>S<sub>8</sub> bulk model.

### 3.6 Surface modelling of Fe<sub>5</sub>Ni<sub>4</sub>S<sub>8</sub>

The various surface terminations for the Fe<sub>5</sub>Ni<sub>4</sub>S<sub>8</sub> system were explored in this section. Examining the surfaces was important to determine the most stable surface terminations. The pentlandite mineral was cleaved along the (111), (211), (224) and (311) surfaces.

### 3.5 Cleaving of (211), (224), (111) and (311) surfaces

Cutting of mineral surfaces emulates the experimental ore or mineral grinding. This process is accomplished by creating two-dimensional slabs of the mineral within a three-dimensional unit cell [88]. The mineral bulk was cleaved along a specific Miller index plane to produce a bulk-terminated surface that extends infinitely in two dimensions while incorporating a vacuum layer along the third dimension, as illustrated in Figure 2.2. This approach mimics the process of crushing rock ore, where various surfaces are exposed. Typically, minerals tend to cleave or fracture along certain planes that are thermodynamically stable, especially those characterised by larger interplanar spacing and stronger bonds [88].

Gibbs [89] concept was established that the equilibrium structure of a crystal minimises excess energy for a given volume. Since volume and surface area are inherently connected, the crystal face with the lowest surface energy tends to dominate. Identifying the surface structure with the lowest surface energy for each metal or mineral under investigation provides the best opportunity to define a broadly representative working surface. This requires accounting for the numerous Miller index planes and the various possible bulk terminations within each plane.

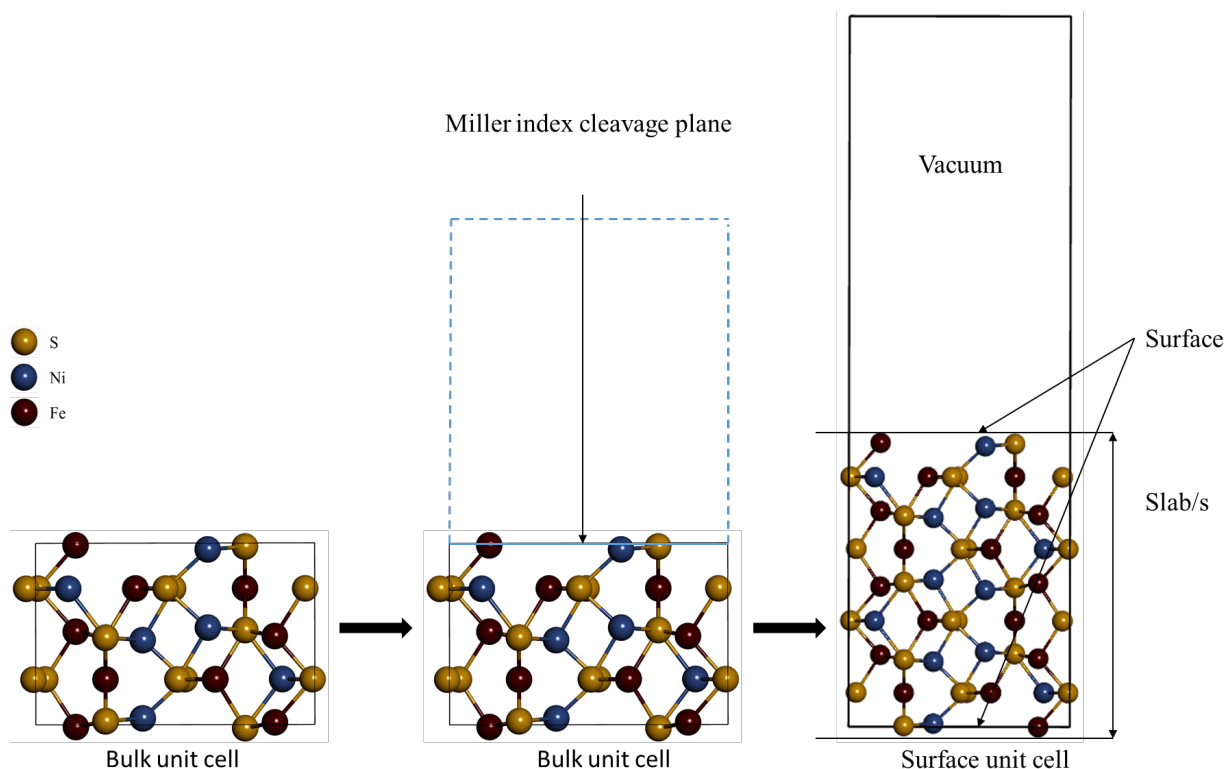


Figure 3.7 : A simplified representation of the (000) surface cleavage methodology for on  $\text{Fe}_5\text{Ni}_4\text{S}_8$ .

As shown in Figure 3.7, the periodic boundaries result in both the top and bottom faces of the mineral slab being bulk terminations and, therefore, exposed surfaces. The geometry of the top surface is defined by the selected Miller index plane and surface termination, while the bottom surface depends on the slab depth. The slab depth is a critical parameter in surface modelling since shallow slabs may inadequately represent a solid-state interface system [88].

The main concern is ensuring the slab depth is sufficient for both surfaces to behave as if they are above an effectively infinite bulk solid, preventing any interaction between the surfaces through the solid. While achieving this would ideally require a very deep slab, the computational cost of modelling such slabs was avoided. The initial approach to surface cleavage focused on identifying the most favourable surface termination without a dipole. If a surface termination exhibits a dipole, it can be addressed through reconstruction. Various surface types, as outlined by Tasker [26] are considered in this process, as shown in Figure 3.8. It is demonstrated that the Type I surface has a repeat unit cell where the anions and cations in the same plane are in a stoichiometric ratio. The Type II surface features a stacking sequence of charged planes, but its repeat unit consists of multiple planes that, when considered together, produce no dipole moment perpendicular to the surface. Type III surfaces consist of a stack of alternately charged planes and generate a dipole moment perpendicular to the surface when cut between any of the planes. In nature, these surfaces are

stabilised by defects or adsorbed species. To simulate Type III surfaces, the dipole must be eliminated, leading to the reconstructed Type III surface.

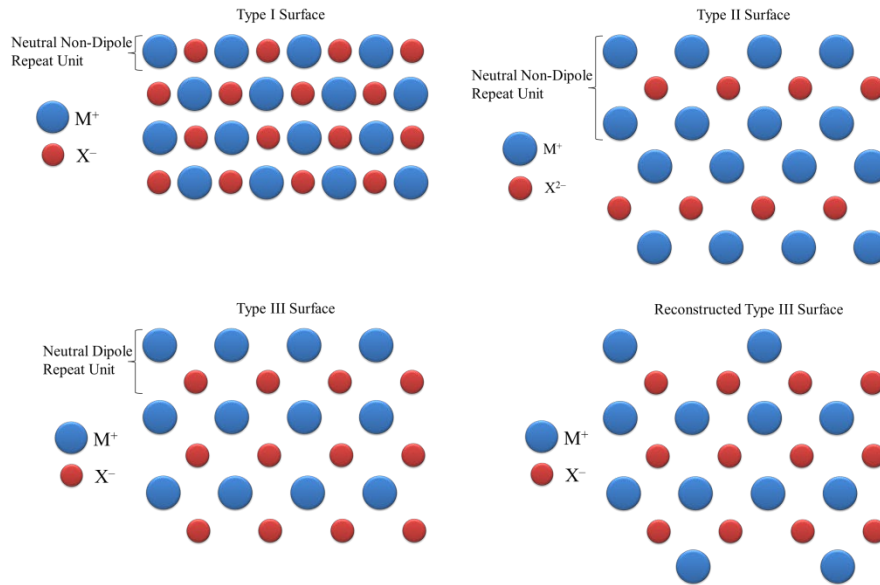


Figure 3.8 : Representation of the different types of surfaces.

The geometry of the top termination surface is determined by the chosen Miller index plane and surface termination, while the bottom termination surface is defined by the slab depth. For a stable surface slab, the bottom termination must be symmetric to the top termination. The most stable surface, free of a dipole, is stoichiometric (bulk equivalent) and symmetric (with top and bottom being mirror images). The stability of surface terminations and slab thickness can be assessed computationally by calculating the surface energy, which measures the excess energy per unit area caused by cleaving a bulk model. A small, positive value indicates a stable surface, as illustrated in Equation 3.1.

$$E_{\text{surface}} = \left( \frac{1}{2A} \right) [E_{\text{slab}} - n(E_{\text{bulk}})], \quad 3.1.$$

In this formula,  $E_{\text{(slab)}}$  represents the surface energy,  $E_{\text{(bulk)}/\text{atom}}$  is the energy per atom in the bulk,  $n_{\text{(slab)}}$  is the number of atoms on the surface, and  $A$  is the surface area. This equation is used to account for the number of atoms at the surface and normalise it with respect to the bulk. To make the search for the most stable surfaces computationally feasible while focusing on the most probable surfaces, only the bulk terminations with the Miller indices (111), (211), (224), and (311) were considered.

### 3.6.1 Different surface termination of $\text{Fe}_5\text{Ni}_4\text{S}_8$ (111), (211), (224) and (311) surfaces

For the  $\text{Fe}_5\text{Ni}_4\text{S}_8$  system, there were 30 distinct surface terminations generated. As illustrated in Figures 3.6–3.9, the (111), (211), (224) and (311) surfaces had 13, 8, 9 and 3 terminations, respectively. Only terminations with no dipole were preferred for further relaxation, which was the first termination for all surfaces.

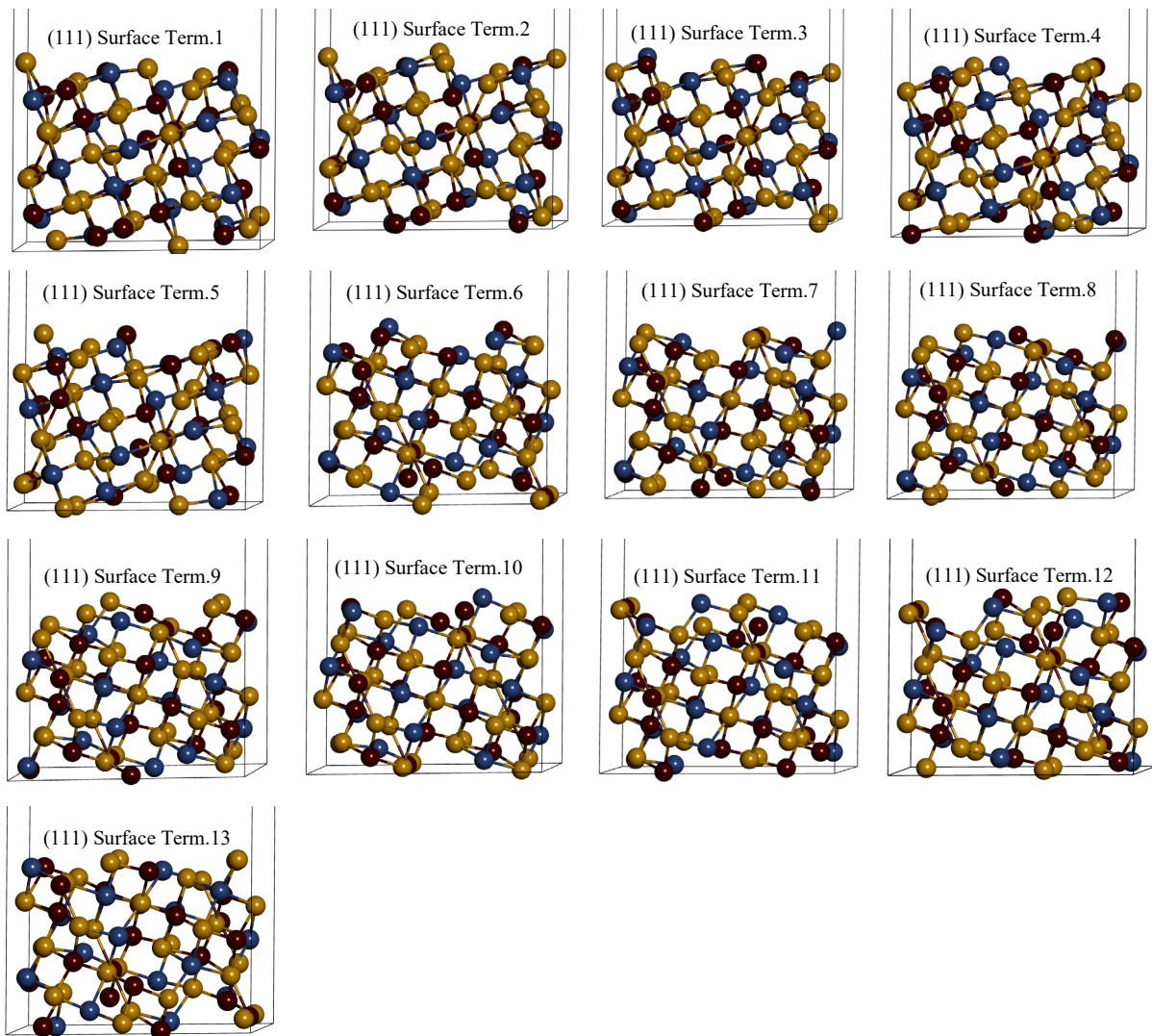


Figure 3.9 : Shows different terminations for  $\text{Fe}_5\text{Ni}_4\text{S}_8$  (111) surface.

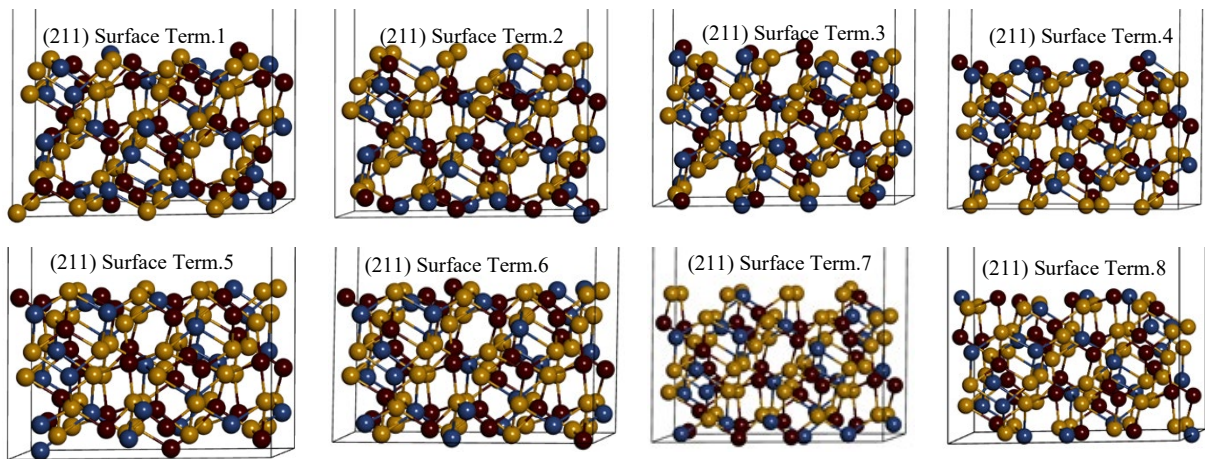


Figure 3.10 : Shows different terminations for  $\text{Fe}_5\text{Ni}_4\text{S}_8$  (211) surface.

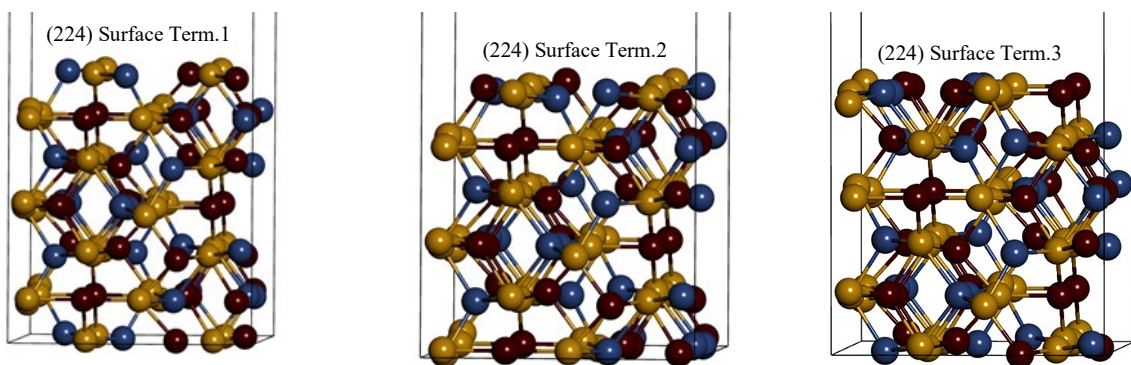


Figure 3.11 : Shows different terminations for  $\text{Fe}_5\text{Ni}_4\text{S}_8$  (224) surface.

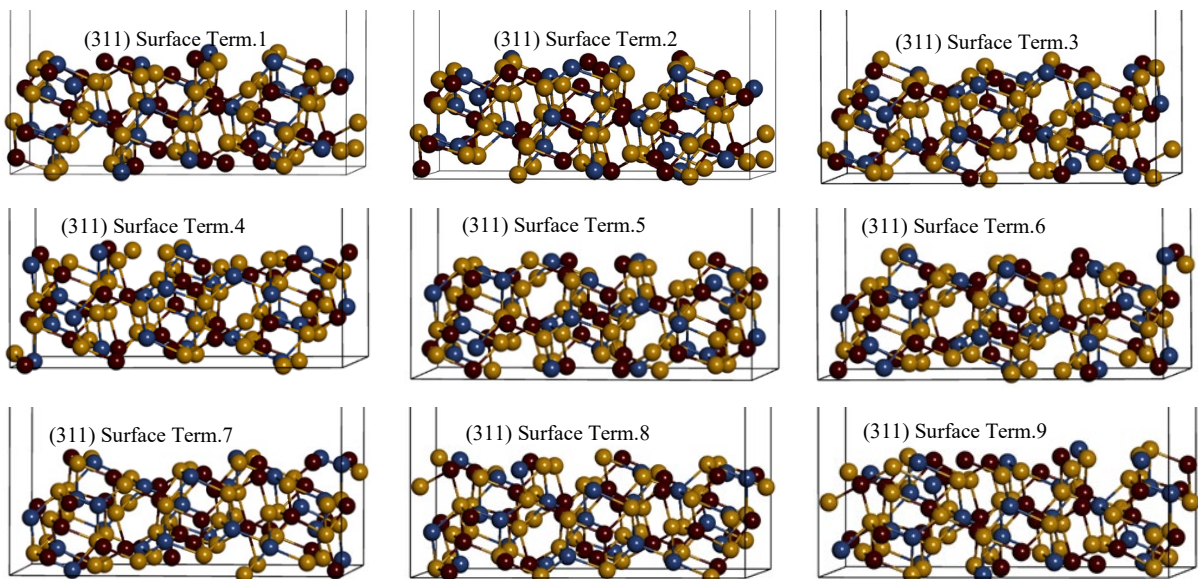


Figure 3.12 : Shows different terminations for  $\text{Fe}_5\text{Ni}_4\text{S}_8$  (311) surface.

### 3.6.2 Non-dipole (111), (211), (224) and (311) surface optimisation of Fe<sub>5</sub>Ni<sub>4</sub>S<sub>8</sub>

The non-dipole surface terminations of (111), (211), (224) and (311) surfaces were investigated; the unrelaxed and relaxed non-dipole surface terminations are shown in Figure 3.10 and their surface energies displayed in Table 3.2. It has been reported that the (111) surface for (Fe, Ni)<sub>9</sub>S<sub>8</sub> was the most stable surface [90]. However, in this study, the (311) surface was found to be the most stable surface since it had the lowest surface energy of 1.484 J/m<sup>2</sup>, followed by the (111) surface with surface energy of 1.622 J/m<sup>2</sup> and then the (211) and (224) surfaces, as shown in Table 3.2. This was in good agreement with the reported experimental XRD [87] which showed that the (311) surface plane had the highest intensity, therefore the most dominant surface.

Table 3.2 : (111), (211), (224) and (311) surface optimisation of Fe<sub>5</sub>Ni<sub>4</sub>S<sub>8</sub>, number of atoms per slab, total energy (eV) and surface energies (J/m<sup>2</sup>).

Surface	No. of Atoms	Surface Area (Å <sup>2</sup> )	Surface Energy (J/m <sup>2</sup> )	Dispersion Energy (J/m <sup>2</sup> )
(111)	68	108.766	1.622	0.452
(211)	102	133.501	1.843	0.511
(224)	102	134.246	1.844	0.406
(311)	102	226.209	1.484	0.415

As demonstrated in Figure 3.13a, the Fe1, Ni2 and Ni3 relaxed inwards by  $-0.0016 \text{ \AA}$ ,  $-0.0166 \text{ \AA}$  and  $-0.0078 \text{ \AA}$ , respectively, on the top surface (Table 3.3). It was noted that Fe1 relaxed and formed a bond with the S1 atom, while Ni3 formed a bond with the S2 atoms after relaxation. This resulted in a preferential sulphur-terminated (111) surface. The bond length between S1 and Ni1 atoms of the (111) surface decreased from  $2.229 \text{ \AA}$  to  $2.200 \text{ \AA}$ . The bond length between S2 and Ni2 before relaxation was  $2.133 \text{ \AA}$ , which decreased to  $2.114 \text{ \AA}$  after relaxation. At the bottom of the surface, it was observed that Fe3 relaxed upwards by  $+0.0131 \text{ \AA}$  and formed a new bond with the S4 atom after relaxation.

Figure 3.13b demonstrated that the Fe1 atom relaxed inwards by  $-0.2839 \text{ \AA}$  (Table 3.3) on the top surface. The bond length between S1 and Fe1 atoms of the (211) surface increased from  $2.102 \text{ \AA}$  to  $2.118 \text{ \AA}$ . The bond length between S2 and Fe2 decreased from  $2.143 \text{ \AA}$  to  $2.117 \text{ \AA}$  after relaxation. At the bottom of the surface, it was noted that the Fe2, Fe3 and S4 atoms relaxed upwards by  $+0.0534 \text{ \AA}$ ,  $+0.0076 \text{ \AA}$  and  $+0.0107 \text{ \AA}$ , respectively (Table 3.3). The Fe2 atom formed a bond with S3 after relaxation. The bond length between Fe3 and S4 was reduced from  $2.672 \text{ \AA}$  to  $2.238 \text{ \AA}$ .

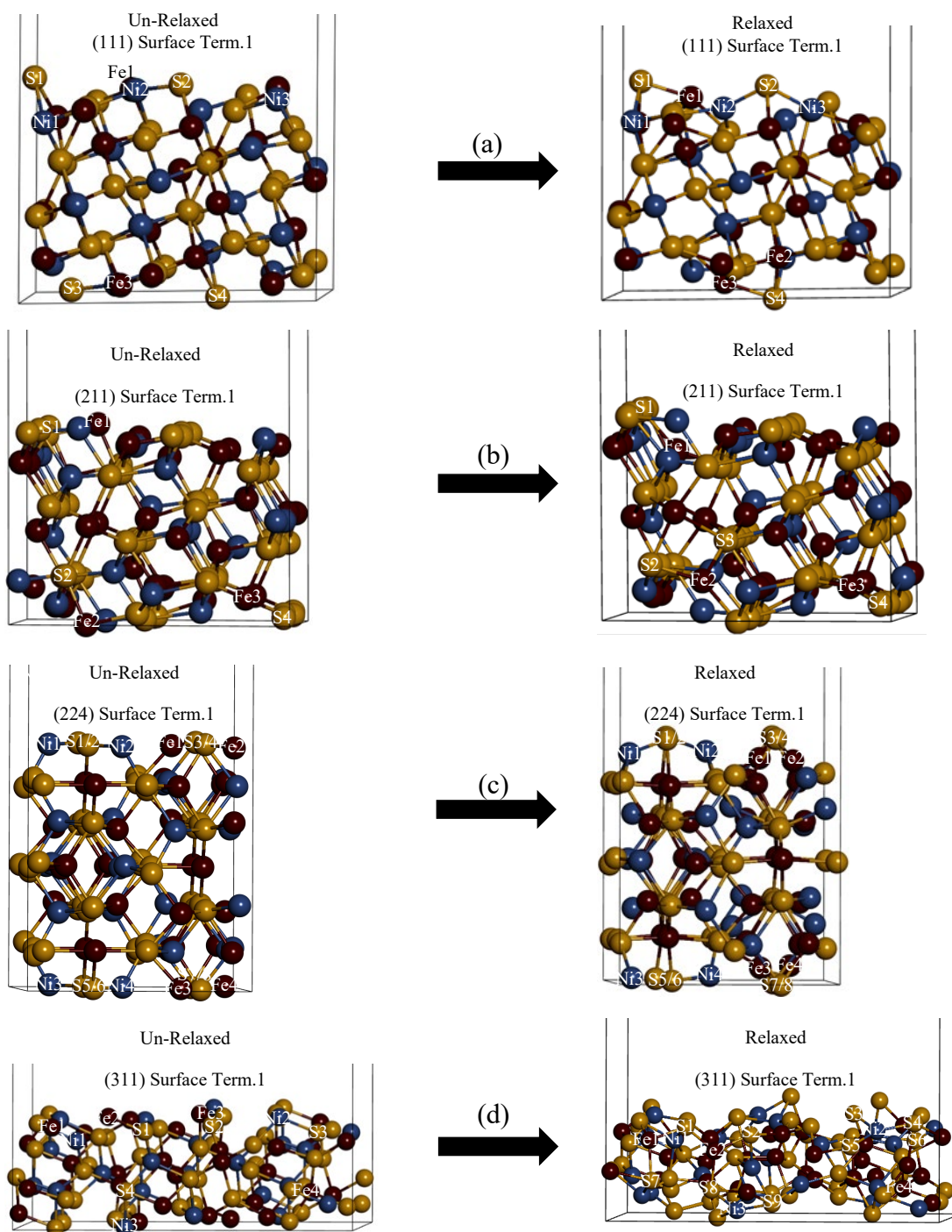


Figure 3.13 : Shows  $\text{Fe}_5\text{Ni}_4\text{S}_8$  un-relaxed and relaxed non-dipole surface: (a) (111), (b) (211), (c) (224) and (d) (311) surface terminations.

The Ni1, Ni2, Fe1 and Fe2 atoms of the (224) surface relaxed inwards by  $-0.0120 \text{ \AA}$ ,  $-0.0121 \text{ \AA}$ ,  $-0.0228 \text{ \AA}$  and  $-0.0228 \text{ \AA}$  (Table 3.3), respectively, on the top surface, as demonstrated in Figure 3.13c. The bond length between S1 and Ni1, S2 and Ni2 decreased from  $2.285 \text{ \AA}$  to  $2.086 \text{ \AA}$ . The bond length between S3 and Fe1, S4 and Fe2 reduced from  $2.285 \text{ \AA}$  to  $2.060 \text{ \AA}$  after relaxation. This resulted in a sulphur-terminated (224) surface. At

the bottom of the surface, it was observed that the Ni4, Fe3 and Fe4 atoms relaxed upwards by +0.0055 Å, +0.0178 Å and +0.0178 Å.

As shown in Figure 3.13d, on the top surface the Fe1, Fe2, Fe3 and Ni2 atoms of the (311) surface relaxed inwards by -0.0410 Å, -0.0133 Å, -0.0328 Å and -0.0851 Å (Table 3.3). It was observed that the Fe1 atoms relaxed and formed a bond with S7, while Fe2 atoms formed new bonds with S1, S2 and S5 atoms after relaxation. Furthermore, Ni2 atoms formed bonds with S3, S4, S5 and S6 atoms after relaxation. The bond lengths between Fe1 and Ni1 and between S2 and Fe2 atoms were noted to increase from 2.506 Å to 2.750 Å and from 2.102 Å to 2.170 Å, respectively. This resulted in a referential sulphur- terminated (311) surface. At the bottom of the surface, it was noted that the Ni3 atom relaxed upward by +0.0183 Å (Table 3.3) and formed a bond with S9. The bond length between S4 and Ni3 increased from 2.229 Å to 2.219 Å after relaxation.

Table 3.3 : Atomic vertical displacements ( $\Delta d_z$ , Å) of the (111), (211), (224) and (311) surface of  $\text{Fe}_5\text{Ni}_4\text{S}_8$ , obtained from the unrelaxed ( $d_{z(U)}$ ) and relaxed ( $d_{z(R)}$ ) Z-atomic position.

Species	$\Delta d_z$
<b>(111) Surface</b>	
Fe1	-0.0016
Ni2	-0.0166
Ni3	-0.0078
Fe3	+0.0131
<b>(211) Surface</b>	
Fe1	-0.2839
Fe2	+0.0543
Fe3	+0.0076
S4	+0.0107
<b>(224) Surface</b>	
Ni1 = Ni2	-0.0120
Fe1 = Fe2	-0.0228
Ni4	+0.0055
Fe3 = Fe4	+0.0178
<b>(311) Surface</b>	
Fe1	-0.0410
Ni1	-0.0133
S2	-0.0328
Fe2	-0.0851
Ni3	+0.0183

A negative and positive value shows inward and upward displacement, respectively.

### 3.6.3 Electronic properties of the clean (311) surface

The computed density of states for the  $\text{Fe}_5\text{Ni}_4\text{S}_8$  (311) surface is shown in Figure 3.14. On the TDOS it was noted that the  $\text{Fe}_5\text{Ni}_4\text{S}_8$  (311) surface had a metallic behaviour since there was no band gap at the  $E_F$ . In addition, the  $E_F$  fell deep into the pseudo gap, suggesting stability. The PDOS clearly showed that the Fe1 was more active at the  $E_F$ . The S1 atom

displayed very low states at the  $E_F$ , suggesting their low activity on the surface. On the VB it was observed that from  $-15$  eV to  $-11$  eV there was a contribution of S1 atoms s-orbital. The broad peak was also observed from VB  $-8$  eV to CB  $2$  eV which consists of S, Ni and Fe atoms. The S1 atoms p-orbital contribute from  $-8$  eV to  $-3$  eV, from  $-3$  eV to  $-1$  eV there was a contribution of Ni1 atoms d-orbital. It was also observed that the Fe1 atom d-orbital contributes from  $-1$  eV to  $2$  eV. At the  $E_F$  it was noted that there was a high contribution of the Fe1 atoms which destabilises the  $Fe_5Ni_4S_8$  (311) surface. However, the low contribution of the S1 and Ni1 atoms at the  $E_F$  stabilises the surface. These observations suggest that the  $Fe_5Ni_4S_8$  (311) surface will be more reactive through the Ni1 atoms.

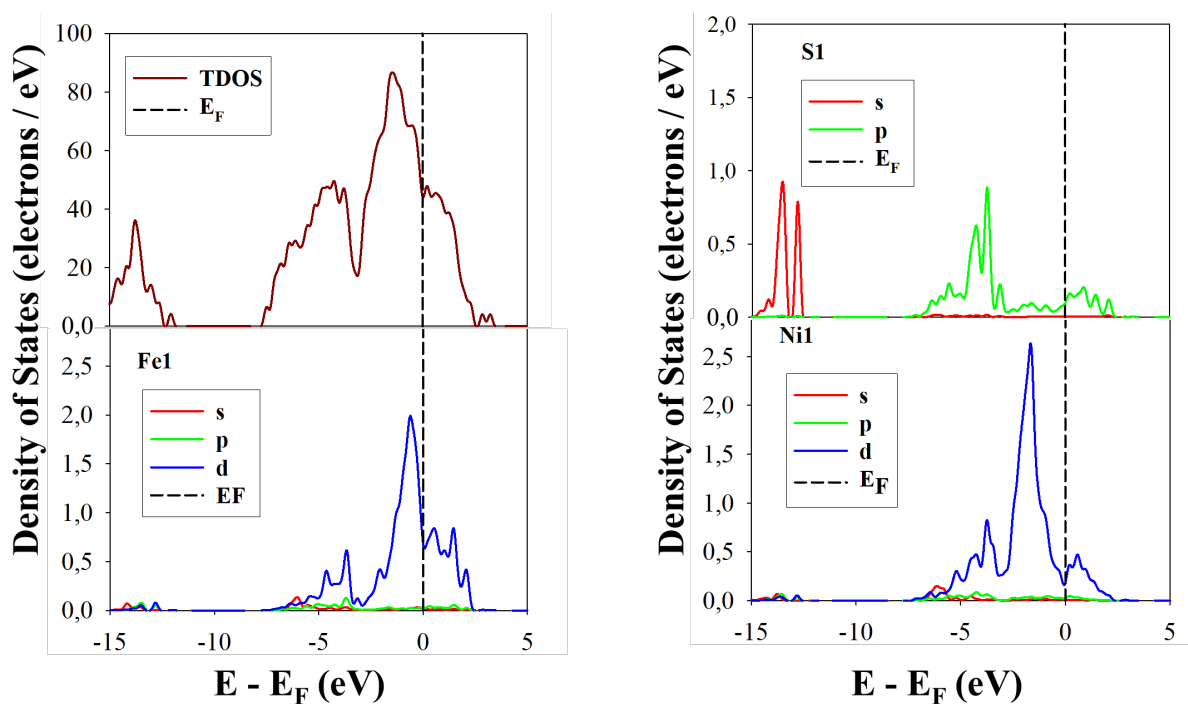


Figure 3.14 : Surface density of states of  $Fe_5Ni_4S_8$  (311) surfaces.

### 3.7 Summary

In this chapter, the bulk and surface structures of  $Fe_5Ni_4S_8$  were analysed. The cut-off energy of 400 eV was found sufficient to minimise the total energy variation of the bulk  $Fe_5Ni_4S_8$  system. The number of k-points required for convergence was found to be  $8 \times 8 \times 6$  for bulk  $Fe_5Ni_4S_8$  and  $4 \times 4 \times 1$  for the surface. The optimised bulk structure was found to have lattice dimensions of  $a = b = 7.020$  Å and  $c = 9.930$  Å. From the electronic structures of the  $Fe_5Ni_4S_8$  bulk the TDOS portrayed a metallic behaviour due to no band gap at the  $E_F$ . The XRD was computed to determine the most dominant plane of the pentlandite minerals. It was found that the (211), (224), (111) and (311) surfaces had the highest intensities and therefore

the most dominant planes. Based on these XRD, the surfaces were cleaved at different terminations, considering the non-dipole surfaces. The surface energies showed that the (311) surface was the most stable and therefore less reactive, which will be adopted for adsorptions. The electronic structures of the  $\text{Fe}_5\text{Ni}_4\text{S}_8$  (311) surface showed that the  $E_F$  fell deep into the pseudo gap suggesting stability. Moreover, the Fe atoms dominated the  $E_F$ , suggesting that they are more active on the surface.

**CHAPTER 4**

**Adsorption of  
collectors on  $\text{Fe}_5\text{Ni}_4\text{S}_8$   
(311) Surface**

In this chapter, the molecular geometries of isolated ADEDTC, IPDETC, MBTNa, and SDTBAT collectors were examined. The collector reagent's role during the flotation process was to promote the interaction between the mineral and air bubbles by creating a water-repellent layer. As such, this will be mimicked to understand the interaction reactivity of collectors with iron-rich pentlandite. Additionally, the adsorption of neutral ADEDTC, IPDETC, MBTNa, and SDTBAT on the  $\text{Fe}_5\text{Ni}_4\text{S}_8$  (311) surface was discussed, with an analysis of the adsorption and dispersion energies, bond lengths and angles of the adsorbate. Finally, the electronic properties of ADEDTC, IPDETC, MBTNa, and SDTBAT adsorptions on the  $\text{Fe}_5\text{Ni}_4\text{S}_8$  (311) surface were presented and analysed.

## 4.1 Collectors geometries and energies

The organic collectors ADEDTC, IPDETC, MBTNa and SDTBAT have different molecular structures, and thus their geometries differ, and therefore their total energies will be different. Their geometric relaxation modes were analysed, and their reactivity predicted from the highest occupied molecular orbital (HOMO) and the lowest unoccupied molecular orbital (LUMO) energies.

### 4.1.1 Molecular geometry of isolated heterocyclic, s-triazine and thionocarbamate collectors

The collectors were optimised using PAW pseudopotentials, with the same cut-off energy and other parameters as those used for the surface system, and k-point parameters set to the gamma point ( $1 \times 1 \times 1$ ) inside a cubic cell of 40 Å using VASP code. The collector molecules HOMO and LUMO energies and their isosurfaces were obtained from optimisation with DMol<sup>3</sup> [91]. The DMol<sup>3</sup> calculations were performed using GGA-PBE and adopted the dispersion correction by Tkatchenko and Scheffler (TS) approach to account for the long-range interactions [54]. The convergence tolerances for energy, force and displacement were  $2.0 \times 10^{-5}$  Ha, 0.004 Ha/Å and 0.005 Å, respectively. The double numerical plus polarisation (DNP) basis set with 4.4 basis files was set using DFT semi-core pseudopotentials. The optimised collector geometries are shown in Figure 4.1, and the parameters for their functional groups are shown in Table 4.1. The s-triazine, heterocyclic and thionocarbamate collectors head group were identified by functional group due to possessing the NCS group –  $\text{NHN}_3\text{C}_3\text{S}_2$ ,  $-\text{NCS}_2$ ,  $-\text{NHSCO}$  and  $-\text{NCS}_2$ , respectively. The chosen parameters (bond length

and bond angles) for the functional groups are reported in this section. These functional groups consist of polar sulphurs, which are the active sites of reaction.

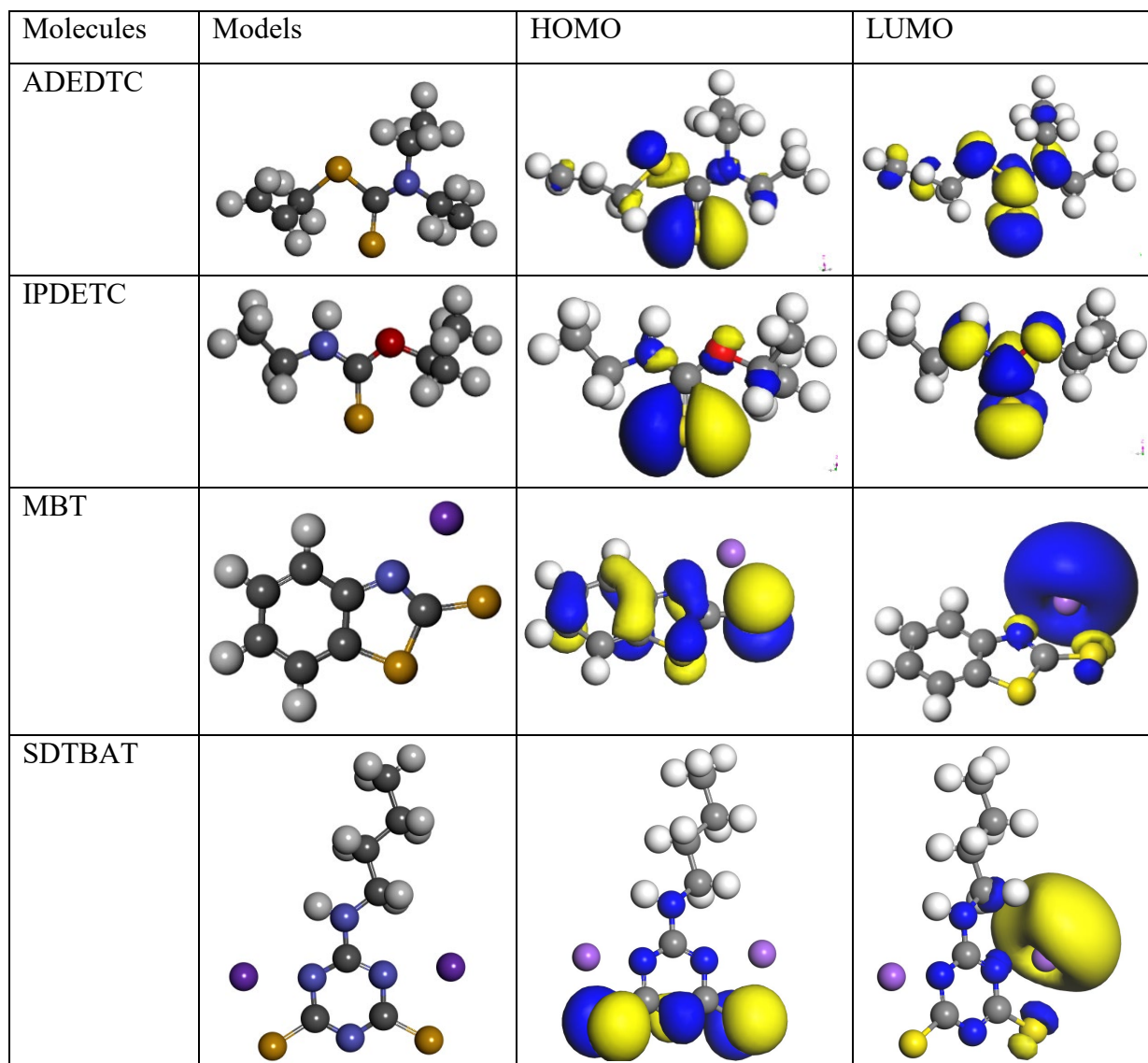


Figure 4.1: Relaxed molecular geometries of organic collectors: ADEDTC, IPDETC, MBTNa and SDTBAT.

The calculated bond lengths, bond angles and torsion angles for ADEDTC, IPDETC, MBTNa, and SDTBAT collectors are shown in Table 4.1. It was observed that the double bond on the ADEDTC, IPDETC and MBTNa was located on the S1 (C=S1). The S1 and S2 atoms on the SDTBAT were single bonded and also negatively charged. The sodium ion ( $\text{Na}^+$ ) was included to neutralise the negative charge/s. The C=S1 bond length of IPDETC (1.665 Å) was noted to be the shortest amongst the collectors, which indicated that this bond was more stable, thus less reactive. The C–S bonds on the SDTBAT (1.725 Å and 1.723 Å) were longer, suggesting less stable and therefore highly reactive. The C–O and C–N bonds

were around 1.35 Å. The torsion angles for ((S1-C=N1)-N) and ((S2-C-N1)=N) were nearly 120°, ((S1-C-N)=S), ((N-C-O)=S1) and ((S1=C-S2)-N/=C) (ADEDTC) were close to 115° and ((S1=C-N)-O) and ((S1=C-S2)-N/=C) (MBTNa) were close to 125°. The atoms with the same torsion angle lied almost in the same plane.

Table 4.1: Calculated bond lengths ( $R$ , in Å), bond angles ( $\theta$ , in deg.) and torsion angle ( $\phi$ , in deg.). The theoretical/experimental values are shown in parenthesis for comparison.

Bonds	Collectors			
	ADEDTC	IPDETC	MBTNa	SDTBAT
$R(\text{C}=\text{S1})$	1.665	1.658	1.706	–
$R(\text{C}-\text{S2})$	1.784	–	1.770	1.725
$R(\text{C}-\text{S1})$	–	–	–	1.723
$R(\text{C}-\text{O})$	–	1.361	–	–
$R(\text{C}-\text{N})$	1.360	1.352	1.341	1.345
$R(\text{C}=\text{N1})$	–	–	–	1.376
$\phi((\text{S1}=\text{C}-\text{S2})-\text{N}/=\text{C})$	112.9	–	120.9	–
$\phi((\text{S1}-\text{C}-\text{N})=\text{S})$	113.5	–	112.8	–
$\phi((\text{S1}=\text{C}-\text{N})-\text{O})$	–	124.4	–	–
$\phi((\text{N}-\text{C}-\text{O})=\text{S1})$	–	108.7	–	–
$\phi((\text{S1}-\text{C}=\text{N1})-\text{N})$	–	–	–	118.1
$\phi((\text{S2}-\text{C}-\text{N1})=\text{N})$	–	–	–	118.8

The reactivity of these collectors before adsorption was characterised by their HOMO and LUMO energies. This was because the spatial distribution of valence electrons, which are crucial for forming chemical bonds between molecules and surfaces, corresponds to the HOMO orbital. Figure 4.1 shows the isosurfaces for the HOMO and LUMO orbitals. It was observed that, for all collectors, the HOMO isosurface was concentrated on the sulphur (S) and nitrogen (N) atoms, indicating that electron donation would likely occur from these atoms. The LUMO isosurface was predominantly located on the sodium (Na) and sulphur (S) atoms for all collectors, suggesting that these atoms can accept electrons. This implied that sulphur atoms have the ability to both donate and accept electrons. The high-density regions of the HOMO orbital can be associated with electrophilic attacks [17, 89]. Previous research suggests that the donor and acceptor behaviour of these collectors on the mineral surface can be predicted by identifying the molecule with the highest HOMO energy and the lowest LUMO energy.

Table 4.2: Calculated HOMO and LUMO energies.

Collector	DMol <sup>3</sup> (eV)		Band gaps (eV)
	HOMO	LUMO	
ADEDTC	-4.744	-1.140	2.57
IPDETC	-4.851	-0.912	3.05
MBTNa	-4.563	-1.755	2.61
SDTBAT	-4.203	-1.567	1.93

A higher HOMO energy level indicates that the molecule has the strongest ability to donate electrons to the unoccupied orbitals of the metal atom, making it more effective as a collector. A lower LUMO energy level indicates that the molecule has the strongest ability to accept electrons from the occupied d-orbitals of the metal atom, enhancing its effectiveness as a collector. According to this theory, the electron-donating ability (HOMO energies) decreases in the following order: SDTBAT > MBTNa > ADEDTC > IPDETC, while the electron-accepting ability (LUMO energies) follows the order: MBTNa > SDTBAT > ADEDTC > IPDETC. This pattern clearly showed that SDTBAT had greater capacity for donating electrons, while MBTNa had the greater capacity of accepting electrons. The band gaps reflect the HOMO-LUMO gap, which can predict the reactivity of the collector molecules, whereby a molecule with a small gap would be more reactive compared to a molecule with a larger gap [93]. This is owed to the easy mobility of electrons from the valence band to the conduction band for a molecule with a small gap. Based on this, as shown in Table 4.2, the SDTBAT had the smallest band gap (1.93 eV), suggesting strong reactivity and the reactivity, order decreased as follows: SDTBAT > ADEDTC > MBTNa > IPDETC. Although the reactivity may be predicted from the H-L gap, adsorption of the collector molecules on the surface is highly dependent on the orientation and matching of the orbital for reactivity. As such, the predicted reactivity may differ from the surface adsorption energies.

### **4.1.2 DOS of ADEDTC, IPDETC, MBTNa and SDTBAT**

The TDOS in Figure 4.2 displays indirect band gaps for the collectors located at the CB, which have been discussed in the previous section to predict the reactivity of the collector molecules. The partial density of states (PDOS) for ADEDTC, IPDETC, MBTNa and SDTBAT collectors clearly showed that the sulphur (S) atoms are the main active sites of reactivity due to their significant contribution at the Fermi energy ( $E_F$ ). The 3p-orbitals of the S atoms were concentrated at the  $E_F$ . The peaks at the  $E_F$  represent the HOMO orbitals, indicating the ability to donate or lose electrons to the mineral surface metal atom. Notably, in Figure 4.2b, the 3p-orbitals HOMO peaks of the S atoms are slightly below the  $E_F$  which reflects its weaker reactivity as predicted from the band gaps. The N atoms for MBTNa and SDTBAT collectors clearly showed little contribution at the  $E_F$  which suggested their weaker ability to react with the mineral surface as compared to the S atoms.

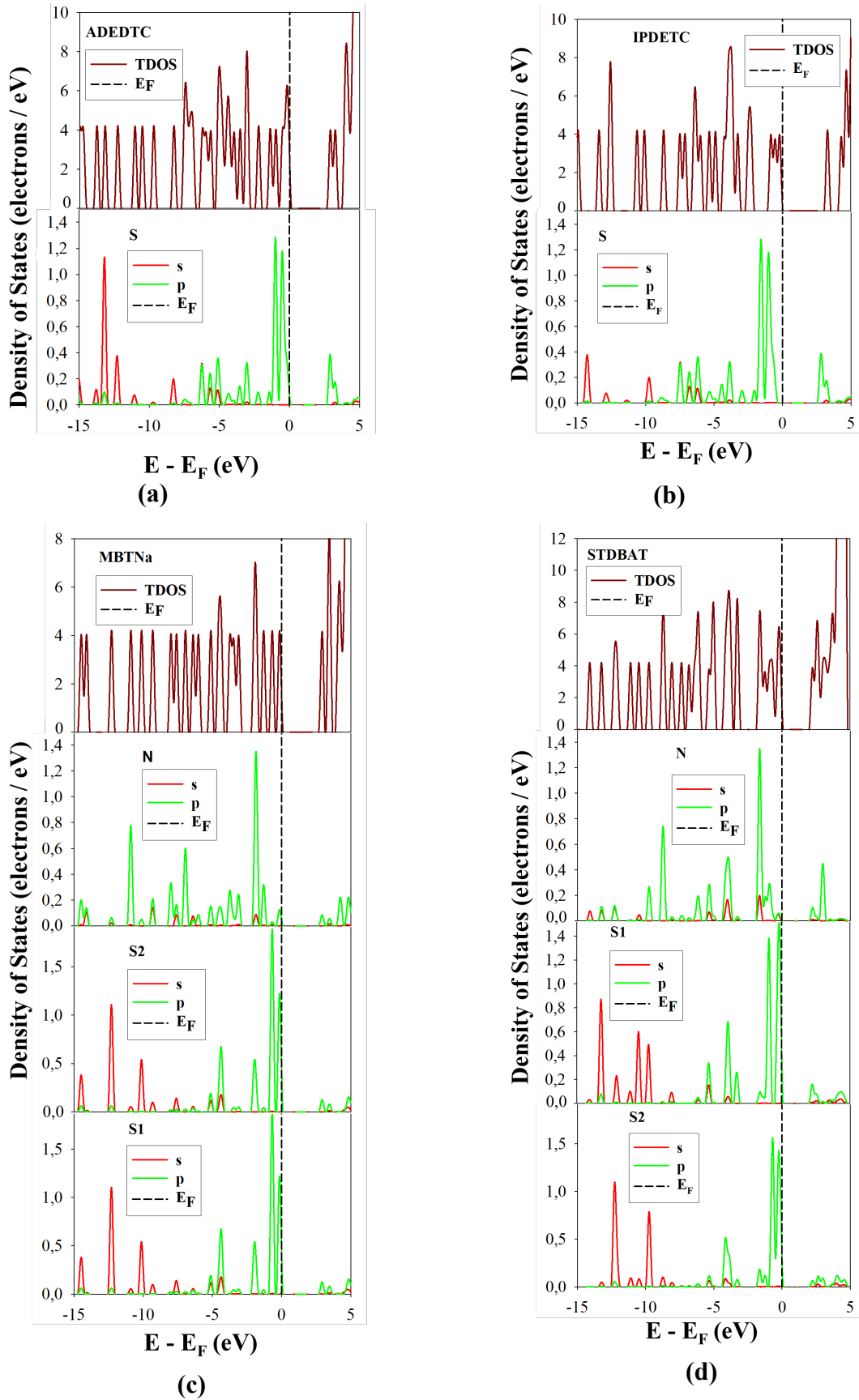


Figure 4.2: Collector density of states: (a) ADEDTC, (b) IPDETC, (c) MBTNa and (d) STDBAT.

## 4.2 ADEDTC, IPDETC, MBTNa, S-triazine adsorptions on Fe<sub>5</sub>Ni<sub>4</sub>S<sub>8</sub> (311) surface.

This section explored the adsorption of ADEDTC, IPDETC, MBTNa and SDTBAT on the Fe<sub>5</sub>Ni<sub>4</sub>S<sub>8</sub> (311) surface. Initially, various adsorption sites were tested, and those with the most exothermic adsorption energies are reported below, while the least exothermic sites are detailed in Appendix D. Note that the MBTNa collector was adsorbed in a vertically and horizontally orientated manner; for both orientations, the strongest adsorption sites are reported. The adsorption geometries, reactivity, and bonding modes of these collectors on the Fe<sub>5</sub>Ni<sub>4</sub>S<sub>8</sub> (311) surface, both before and after relaxation, are illustrated and discussed. The adsorption geometry of ADEDTC, IPDETC, MBTNa and SDTBAT on the Fe<sub>5</sub>Ni<sub>4</sub>S<sub>8</sub> (311) surface on Ni and Fe sites, both before and after relaxation, is shown in Figures 4.3, 4.4, 4.5, 4.6 and 4.7, respectively. The Ni–S = 2.350 Å and Fe–S = 2.400 Å bond lengths acquired from the sum of the empirically measured covalent radii of Ni (1.350 Å), Fe (1.400 Å) and S (1.000 Å) atoms determined by Slater [94] were used to compare with the bond lengths obtained from the adsorptions.

Table 4.3: The adsorption energies, dispersion energies and bond lengths of ADEDTC, IPDETC, MBTNa and SDTBAT collector adsorptions on the Fe<sub>5</sub>Ni<sub>4</sub>S<sub>8</sub> (311) mineral surface.

Adsorption mode	E <sub>ads.</sub> (kJ.mol <sup>-1</sup> )	E <sub>dis.</sub> (kJ.mol <sup>-1</sup> )	Ni–S1 (Å)	Fe–S1 (Å)	Fe–S2 (Å)
<b>ADEDTC</b>					
Ni–S1	–460.58	–97.15	2.250	–	–
Fe–S1	–381.37	–108.05	–	3.788	–
<b>IPDETC</b>					
Ni–S1	–161.01	–87.80	2.244	–	–
Fe–S1	–164.53	–56.27	–	2.355	–
<b>MBTNa</b>					
Ni–S1 (Vertical)	–249.26	–99.43	2.261	–	–
Fe–S1 (Vertical)	–214.17	–73.04	–	2.443	–
Ni–S1 (Horizontal)	–424.08	–109.29	2.339	–	–
Fe–S1 (Horizontal)	–306.99	–104.69	–	4.863	2.438
<b>SDTBAT</b>					
Ni–S1, Fe–S2	–352.48	–183.85	2.261	–	2.380

In Figure 4.3 it was observed that the most exothermic adsorption on the Ni site for ADEDTC collector was S1–Ni (see Figure 4.3a), which gave the bond lengths of 2.250 Å. The adsorption of ADEDTC collector on the Fe site, as shown in Figure 4.3b, resulted in desorption from the Fe atoms, leaving a distance of Fe---S1 = 3.788 Å. Interestingly, it was noted that the allyl chain interacted with the surface Ni atom, which formed C1–Ni = 2.111 Å and C2–Ni = 2.139 Å bonds. The ADEDTC adsorption bond lengths of S1–Ni = 2.250 Å

were smaller than the sum of the empirically measured covalent radii ( $\text{Ni-S} = 2.350 \text{ \AA}$ ) determined by Slater [94], which indicated a stronger bond. This smaller bond of the collector adsorption predicted the strong interaction of the pentlandite mineral with ADEDTC collectors and therefore suggested good floatability. The obtained adsorption energies and dispersion energies for the most exothermic adsorption models on Ni and Fe sites are displayed in Table 4.3. The ADEDTC adsorption on Ni sites gave adsorption and dispersion energies of  $E_{\text{ads}} = -460.58 \text{ kJ.mol}^{-1}$ , including  $E_{\text{disp}} = -97.15 \text{ kJ.mol}^{-1}$ , while on Fe sites gave  $E_{\text{ads}} = -381.37 \text{ kJ.mol}^{-1}$ , including  $E_{\text{disp}} = -108.05 \text{ kJ.mol}^{-1}$ . The adsorption energies clearly showed that the ADEDTC on the Ni site was more exothermic than on the Fe site, which suggested preferential interaction with Ni atoms on pentlandite. This showed that chalcopyrite selective collectors such as ADEDTC [18] may be used for selective flotation of pentlandite minerals. It was noted that the dispersion energies depicted the Fe site adsorption as more exothermic than the Ni site adsorption. This was ascribed to the allyl hydrocarbon chain's long-range interaction and the bonding with the surface.

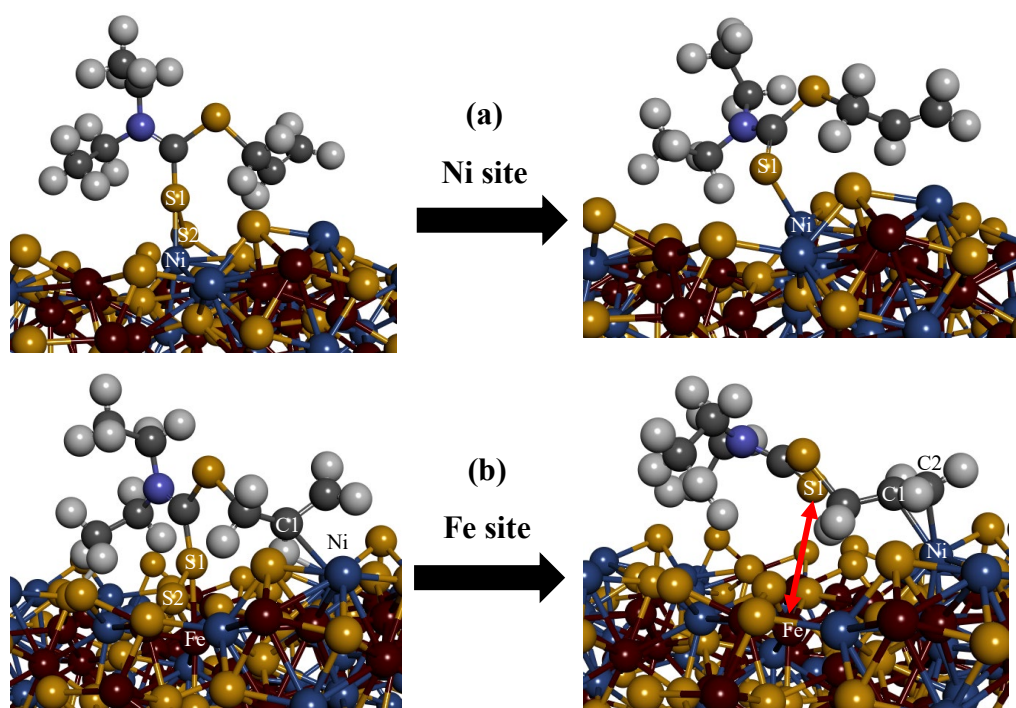


Figure 4.3: The un-relaxed and relaxed ADEDTC collector adsorption on the  $\text{Fe}_5\text{Ni}_4\text{S}_8$  (311) surface.

In the case of IPDETC adsorption as shown in Figure 4.4, the most exothermic adsorption on the Ni site for the IPDETC collector was the S1–Ni monodentate (see Figure 4.4a), which gave the bond length of  $2.244 \text{ \AA}$ . The adsorption of the IPDETC collector on the Fe site, as shown in Figure 4.4b, resulted in mono-bridge bonding on the Fe and Ni atoms, forming

bond lengths of Fe–S1 = 2.355 Å and Ni–S1 = 2.285 Å. For both Ni and Fe site adsorption, the IPDETC preferred to orientate at an angle on the surface. The IPDETC adsorption bond lengths on Ni and Fe sites were smaller than the sum of the empirically measured covalent radii (Ni–S = 2.350 Å and Fe–S = 2.400 Å) determined by Slater [94], which indicated a stronger bond. These smaller bonds of the collector adsorption predicted the strong interaction of the pentlandite mineral with IPDETC collectors and therefore suggested good floatability.

The obtained adsorption energies and dispersion energies for the most exothermic IPDETC adsorption on Ni and Fe sites are displayed in Table 4.3. The IPDETC adsorption on Ni sites gave adsorption and dispersion energies of  $E_{\text{ads}} = -161.01 \text{ kJ.mol}^{-1}$ , including  $E_{\text{disp}} = -87.80 \text{ kJ.mol}^{-1}$ , while on Fe sites gave  $E_{\text{ads}} = -164.53 \text{ kJ.mol}^{-1}$ , including  $E_{\text{disp}} = -56.27 \text{ kJ.mol}^{-1}$ . The adsorption energies clearly showed that the IPDETC on the Fe site was more exothermic than on the Ni site, which was attributed to the bridging on the Fe and Ni atoms. This still indicated the preferential IPDETC collector interaction with Ni atoms on pentlandite. This showed that the chalcopyrite collector, such as IPDETC [18], may be used for selective flotation of pentlandite minerals. It was noted that the dispersion energies depicted the Ni site adsorption as more exothermic than the Fe site adsorption. This was ascribed to the hydrocarbon chain's long-range interaction with the surface, which also indicated the preferential adsorption on the Ni site.

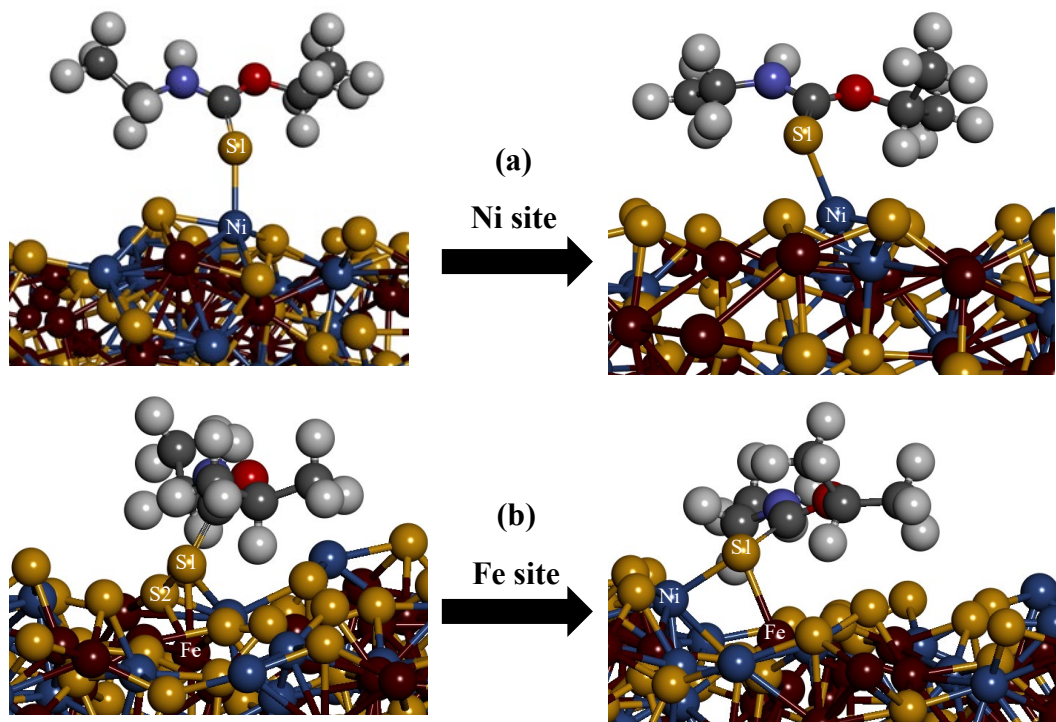


Figure 4.4 : The un-relaxed and relaxed IPDETC collector adsorption on the  $\text{Fe}_5\text{Ni}_4\text{S}_8$  (311) surface.

The adsorption of MBTNa on the  $\text{Fe}_5\text{Ni}_4\text{S}_8$  (311) surface was positioned vertically as shown in Figure 4.5. The most exothermic adsorption on the Ni site for the MBTNa collector was the S1–Ni monodentate (see Figure 4.5a), which gave the bond length of 2.261 Å. The adsorption of the MBTNa collector on the Fe site, as shown in Figure 4.5b, resulted in monodentate bonding with bond lengths of Fe–S1 = 2.443 Å. For both Ni and Fe site adsorption, the MBTNa preferred to orientate at an angle on the surface. The MBTNa adsorption bond length on the Ni site was smaller, while on the Fe site it was larger than the sum of the empirically measured covalent radii (Ni–S = 2.350 Å and Fe–S = 2.400 Å) determined by Slater [94]. This indicated a stronger bond for Ni site MBTNa adsorption and a weaker bond for Fe site MBTNa adsorption. The smaller bond for MBTNa collector adsorption on the Ni site predicted the strong interaction of the pentlandite mineral with MBTNa through Ni atoms.

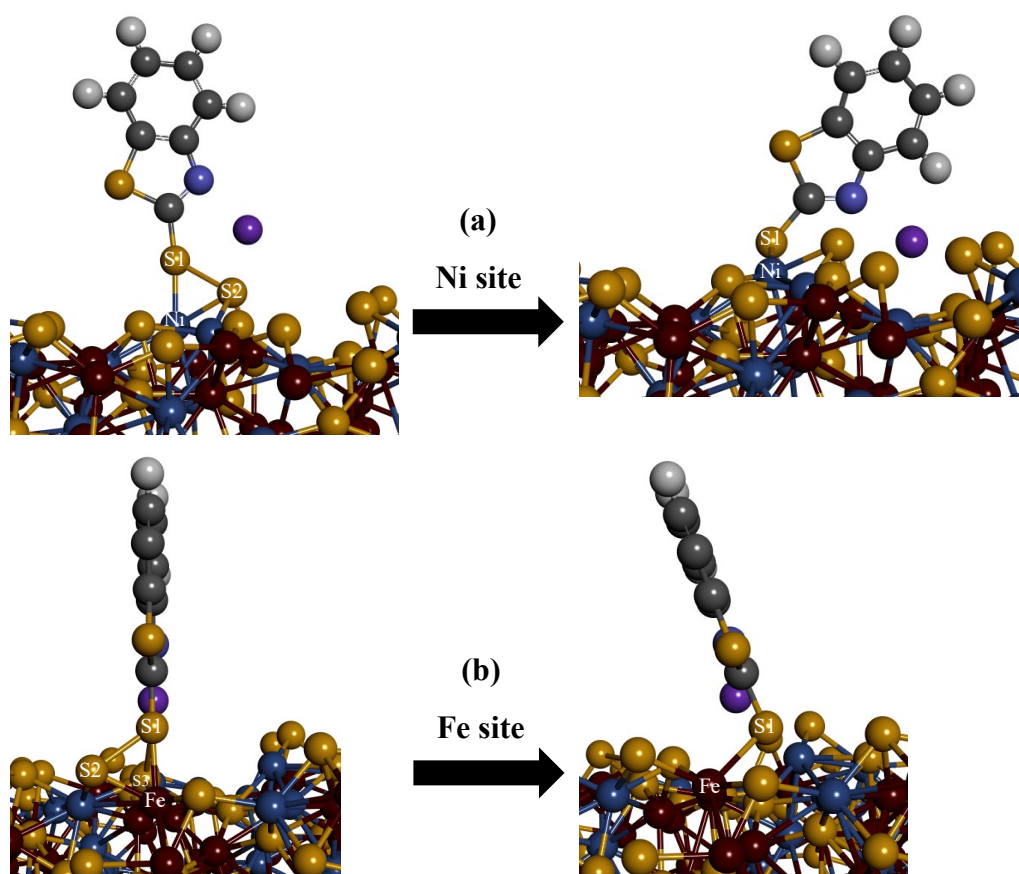


Figure 4.5 : The un-relaxed and relaxed MBTNa collector adsorption vertically on the  $\text{Fe}_5\text{Ni}_4\text{S}_8$  (311) surface.

The obtained adsorption energies and dispersion energies for the most exothermic vertical MBTNa adsorption on Ni and Fe sites are displayed in Table 4.3. The MBTNa adsorption on

Ni sites gave adsorption and dispersion energies of  $E_{\text{ads}} = -249.26 \text{ kJ.mol}^{-1}$ , including  $E_{\text{disp}} = -99.43 \text{ kJ.mol}^{-1}$ , while on Fe sites gave  $E_{\text{ads}} = -214.17 \text{ kJ.mol}^{-1}$ , including  $E_{\text{disp}} = -73.04 \text{ kJ.mol}^{-1}$ . The adsorption energies clearly showed that the MBTNA on the Ni site was more exothermic than on the Fe site, which demonstrated a preferential adsorption on the Ni atoms on pentlandite. It was noted that the dispersion energies depicted the Ni site adsorption as more exothermic than the Fe site adsorption. This was ascribed to the hydrocarbon chain's long-range interaction with the surface. As observed in Figure 4.5a for the Ni site adsorption, the MBTNA is bent more towards the surface compared to the Fe adsorption, (Figure 4.5b).

The horizontal adsorption of the MBTNa on the  $\text{Fe}_5\text{Ni}_4\text{S}_8$  (311) surface is shown in Figure 4.6. The most exothermic adsorption on the Ni site for the MBTNa collector was the S1–Ni monodentate (see Figure 4.6a), which gave the bond length of 2.339 Å. The adsorption of MBTNa collector on the Fe site, as shown in Figure 4.6b, resulted in the desorption of the exocyclic S1 atom from Fe, leaving a distance of  $\text{Fe} \cdots \text{S1} = 4.863 \text{ Å}$ . It was observed that the endocyclic S2 atom remained bonded on the surface, forming a monodentate bond with bond lengths of  $\text{Fe} \text{--} \text{S2} = 2.438 \text{ Å}$ . For both Ni and Fe site adsorption, the MBTNa preferred to orientate flat on the surface. The MBTNa adsorption bond length on the Ni site was smaller, while on the Fe site it was larger than the sum of the empirically measured covalent radii ( $\text{Ni} \text{--} \text{S} = 2.350 \text{ Å}$  and  $\text{Fe} \text{--} \text{S} = 2.400 \text{ Å}$ ) determined by Slater [94]. This indicated stronger bonding between Ni atoms and MBTNa and a weaker bond for the Fe site MBTNa adsorption. The smaller bond for MBTNa collector adsorption on the Ni site also suggested a strong interaction of the pentlandite mineral with MBTNa through Ni atoms.

The obtained adsorption energies and dispersion energies for the most exothermic horizontal MBTNa adsorption on Ni and Fe sites are displayed in Table 4.3. The MBTNa adsorption on Ni sites gave adsorption and dispersion energies of  $E_{\text{ads}} = -424.08 \text{ kJ.mol}^{-1}$ , including  $E_{\text{disp}} = -109.29 \text{ kJ.mol}^{-1}$ , while on Fe sites gave  $E_{\text{ads}} = -306.99 \text{ kJ.mol}^{-1}$ , including  $E_{\text{disp}} = -104.69 \text{ kJ.mol}^{-1}$ . The adsorption energies clearly showed that the MBTNa adsorption on the Ni site was more exothermic than on the Fe site, which demonstrated a preferential adsorption on the Ni atoms on pentlandite. It was noted that the dispersion energies depicted the Ni site adsorption as more exothermic than the Fe site adsorption. This was ascribed to the hydrocarbon chain's long-range interaction with the surface.

In comparison between vertical and horizontal MBTNa adsorption, it was clear that the adsorption energies depicted the horizontal adsorption as more exothermic. This was attributed to the flat mode adsorption, which benefitted strongly from the hydrocarbon chain interaction with the mineral surface. Moreover, the Ni site was the most exothermic

compared to the Fe sites adsorption. This showed that the MBTNa collector may be used for selective flotation of pentlandite minerals from other iron sulphide minerals.

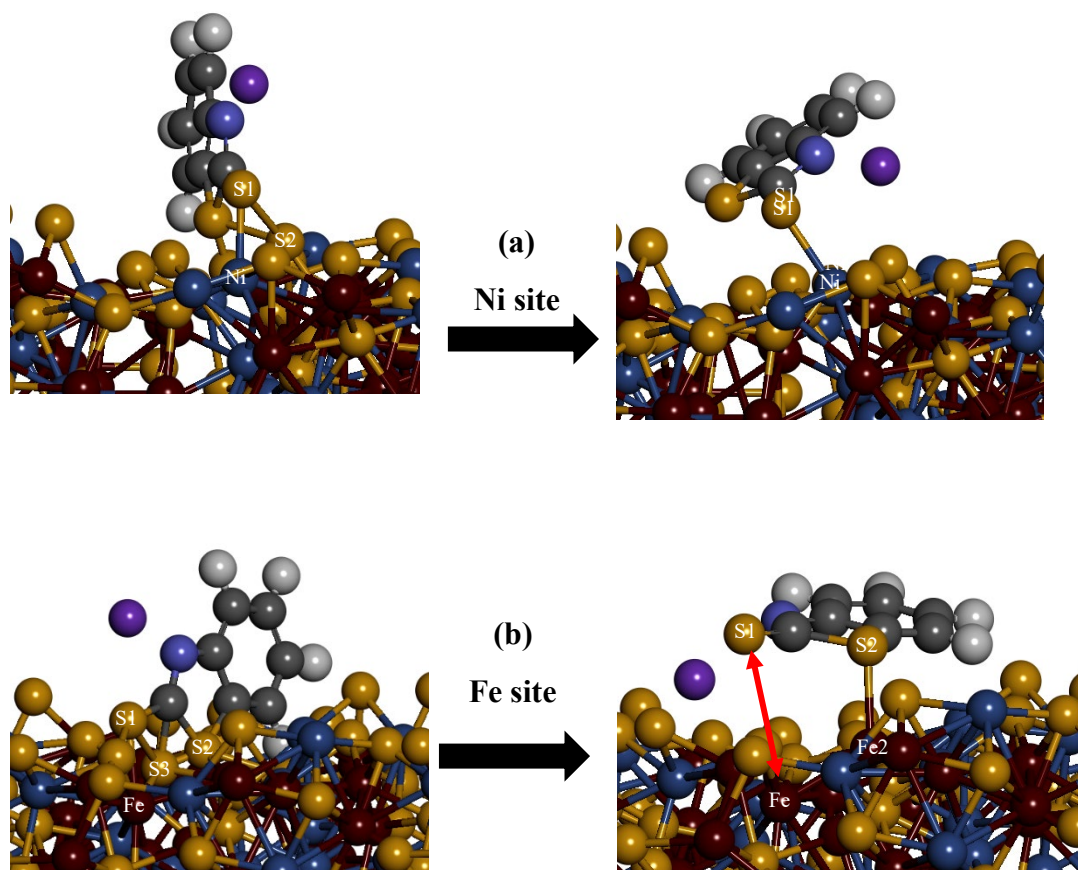


Figure 4.6 : The un-relaxed and relaxed MBTNa collector adsorption horizontally on the  $\text{Fe}_5\text{Ni}_4\text{S}_8$  (311) surface.

The SDTBAT adsorption on the  $\text{Fe}_5\text{Ni}_4\text{S}_8$  (311) surface, as displayed in Figure 4.7, was adsorbed bridging on both Ni and Fe atoms. It was observed that the collector preferred to lie flat with the hydrocarbon chain raised vertically on the surface. The adsorption was bidentate and formed bond lengths of  $\text{Ni-S1} = 2.261 \text{ \AA}$  and  $\text{Fe-S2} = 2.380 \text{ \AA}$ . The SDTBAT adsorption bond lengths on Ni and Fe sites were smaller than the sum of the empirically measured covalent radii ( $\text{Ni-S} = 2.350 \text{ \AA}$  and  $\text{Fe-S} = 2.400 \text{ \AA}$ ) determined by Slater[94]. This indicated stronger bonding of Ni and Fe atoms with SDTBAT adsorption. It was clear that the  $\text{Ni-S1} = 2.261 \text{ \AA}$  was much smaller, which suggested stronger bonding on the Ni site. The smaller bond for SDTBAT collector adsorption also suggested strong interaction of the pentlandite mineral with SDTBAT. The obtained adsorption energies and dispersion energies for SDTBAT adsorption on Ni and Fe sites are displayed in Table 4.3. The SDTBAT

adsorption on Ni sites gave adsorption and dispersion energies of  $E_{\text{ads}} = -352.48 \text{ kJ}\cdot\text{mol}^{-1}$ , including  $E_{\text{disp}} = -183.85 \text{ kJ}\cdot\text{mol}^{-1}$ . It was noted that the dispersion energy for SDTBAT is more negative than all collector adsorption, which was ascribed to the preferential flat adsorption and the hydrocarbon chain's long-range interaction with the surface. The s-triazine group long-range interaction with the surface contributed significantly, displaying the effect of including the dispersion correction on collector adsorption.

In comparison of all collector adsorptions, it was clear that the collectors preferred the Ni sites to the Fe sites on  $\text{Fe}_5\text{Ni}_4\text{S}_8$  pentlandite (311) surface. The adsorption energies were depicted to follow the decreasing adsorption strength as: ADEDTC ( $-460.58 \text{ kJ/mol}$ ) > MBTNa ( $-424.08 \text{ kJ/mol}$ ) > SDTBAT ( $-352.481 \text{ kJ/mol}$ ) > IPDETC ( $-164.53 \text{ kJ/mol}$ ). It was evident that ADEDTC gave much stronger exothermic adsorption energy amongst the collectors. Clearly demonstrated the selectivity of the collector towards Ni atoms and therefore highly selective towards pentlandite.

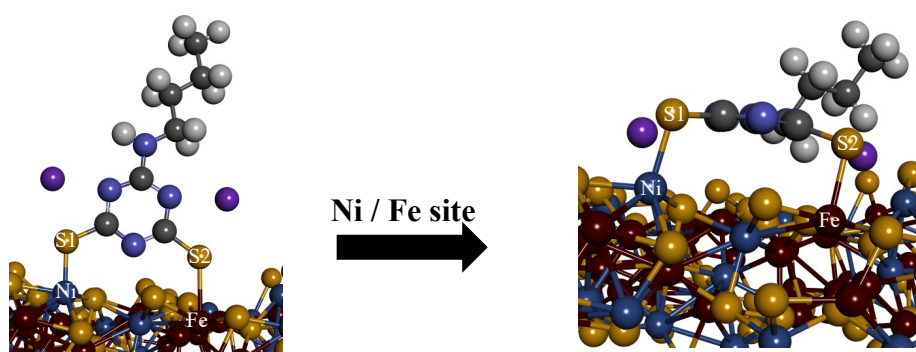


Figure 4.7 : The un-relaxed and relaxed SDTBAT collector adsorption on the  $\text{Fe}_5\text{Ni}_4\text{S}_8$  (311) surface.

The dispersion energies followed the trend order as SDTBAT > MBTNa > ADEDTC > IPDETC. The preferential adsorption on the Ni atoms is greater than the Fe atoms adsorption. This predicted that the collector may be useful as a highly selective collector for separation of pentlandite minerals from other iron sulphide minerals. Similar observations have been found where the ADEDTC and IPDETC collectors preferred Cu atoms in the separation of chalcopyrite from pyrite [94].

### 4.3 Density of states of ADEDTC, IPDETC, MBTNa and SDTBAT adsorptions

This section presents and analyses the electronic properties of ADEDTC, IPDETC, MBTNa and SDTBAT adsorption on  $\text{Fe}_5\text{Ni}_4\text{S}_8$  (311) surface. The focus was on the most

stable adsorption sites, describing the bonding chemistry. Therefore, the density of states (DOS) focused on the interacting active sites of the collectors with the surface atoms is provided.

### **4.3.1 Electronic properties of ADEDTC, IPDETC, MBTNa and SDTBAT adsorption on Fe<sub>5</sub>Ni<sub>4</sub>S<sub>8</sub> (311) surface**

The PDOS for ADEDTC, IPDETC, MBTNa and SDTBAT collector's adsorption on the Fe<sub>5</sub>Ni<sub>4</sub>S<sub>8</sub> (311) surface Ni and Fe atoms are analysed to determine the reactivity chemistry from before and after adsorptions. The PDOS of the collector S atoms and surface Ni and Fe atoms changed after adsorption, which was due to the hybridisation of 3p-orbitals and 3d-orbitals.

The PDOS for ADEDTC collector adsorption on Fe and Ni atoms is shown in Figure 4.8. In Figure 4.8a the PDOS of the ADEDTC collector on the Ni site is examined. It was observed that Ni atoms 3d-orbitals changed just below the  $E_F$  where the sharp peak split into two peaks affected by mixing with the S1 3p-orbitals. The states of the highest state sharp peak did not change but formed a new peak suggesting the gain of electrons from the S1 3p-orbitals. The S1 3p-orbital's highest states two peaks just below the  $E_F$  reduced states after adsorption (from above 1.0 electrons/eV to below 0.5 electrons/eV), which indicated electron loss towards the Ni atoms 3d-orbitals. This suggested that the ADEDTC collector adsorbed on Ni atoms through normal covalent bonding.

The ADEDTC collector adsorption on Fe atoms is shown in Figure 4.8b. It was noted that the Fe 3d-orbital changed at the  $E_F$ , where the split peak just below the  $E_F$  merged to a broad sharp peak. Interestingly, the peak just above the  $E_F$  increased in states suggesting electron loss. Moreover, the peak below the  $E_F$  reduced state after adsorption (from just below 2.0 electrons/eV to just above 1.5 electrons/eV), which clearly demonstrated electron loss from the 3d-orbital. The S1 3p-orbital's two highest states peaks just below the  $E_F$  were merged after adsorption, where the peak on the lower energy was smaller, which resulted in increased states. It should be noted that S1 atoms desorbed from the Fe atoms; as such, the S1 3p-orbital states did not show significant changes. The changes in the Fe atom's 3d-orbital suggested that Fe lost electrons to the neighbouring S atoms on the surface after adsorption.

The PDOS for IPDETC collector adsorption on Fe and Ni atoms is shown in Figure 4.9. In Figure 4.9a the PDOS of the IPDETC collector on the Ni site is examined. It was observed

that Ni atoms 3d-orbitals changed just below the  $E_F$  where the sharp peak split into four peaks affected by mixing with the S1 3p-orbitals. The states were reduced, which was due to the peak split.

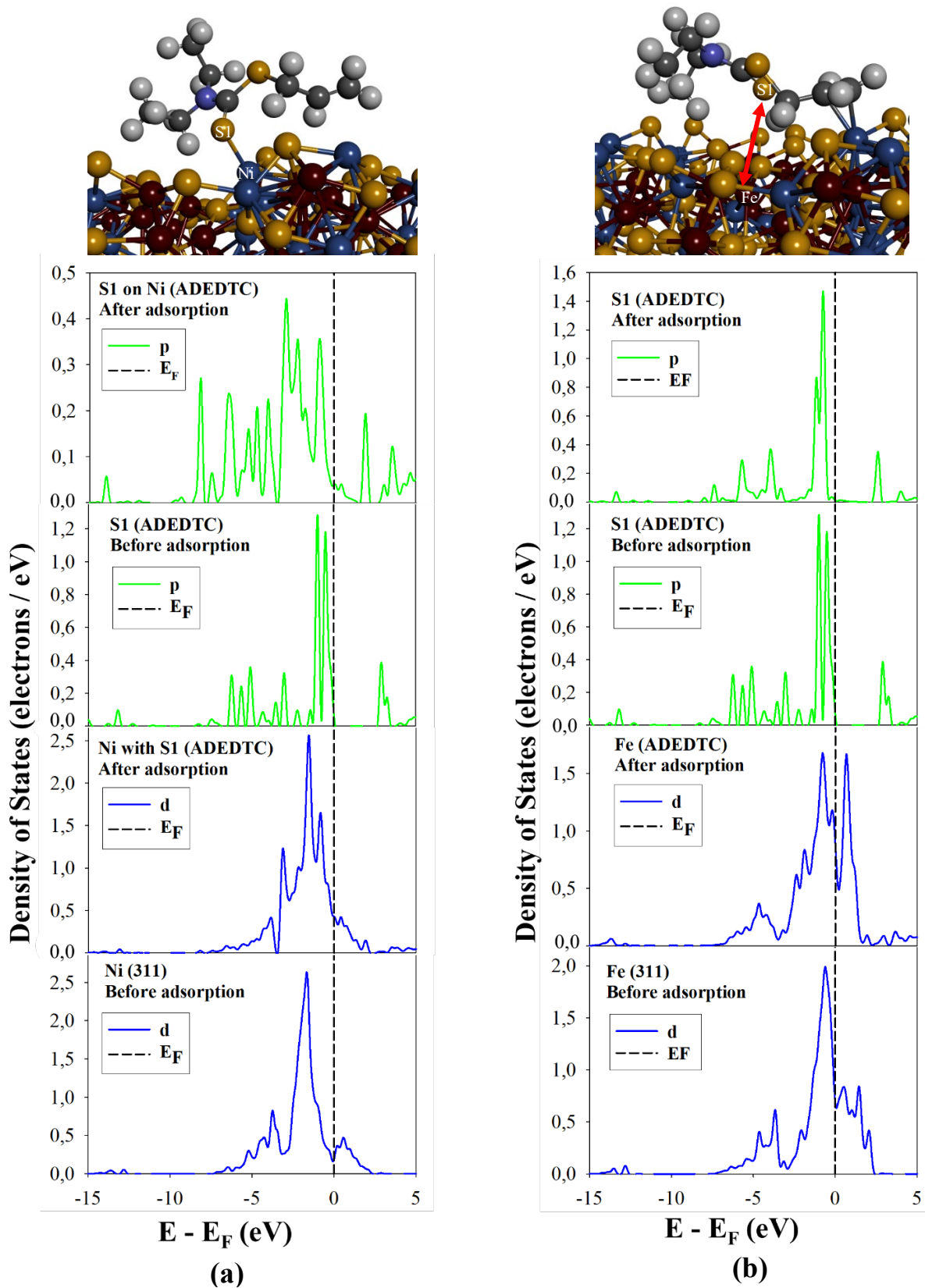


Figure 4.8: Partial density of states (PDOS) of ADEDTC collector before and after adsorption on Fe<sub>3</sub>Ni<sub>4</sub>S<sub>8</sub> (311) surface: (a) Ni site adsorption and (b) Fe site adsorption.

The S1 3p-orbital's highest states two peaks just below  $E_F$  significantly reduced states after adsorption (from above 1.0 electrons/eV to below 0.5 electrons/eV), which indicated electron loss towards the Ni atoms 3d-orbitals. This suggested that the IPDETC collector also adsorbed on Ni atoms through normal covalent bonding. The IPDETC collector adsorption on Fe atoms is shown in Figure 4.9b. It was noted that the Fe 3d-orbital changed at the  $E_F$ , where the smooth sharp peak just below the  $E_F$  was sharper and with a minor split on its sides. Interestingly, the peak just above the  $E_F$  moved towards the  $E_F$  and reduced states, suggesting electron gain to the 3d-orbital. The S1 3p-orbital's two highest states peaks just below the  $E_F$  are significantly reduced to almost zero states just below the  $E_F$  suggesting electron loss. These changes in the Fe atom and S1 atom suggested that the Fe atom gains electrons from the collector S1 atom, forming a normal covalent bond.

The PDOS for MBTNa collector vertical adsorption on Fe and Ni atoms is shown in Figure 4.10. In Figure 4.10a the PDOS of vertical adsorption of MBTNa collector on Ni site was examined. It was observed that Ni atoms 3d-orbitals changed just below the  $E_F$  where the sharp peak formed a minor split, which resulted in a slight decrease in states. The S1 3p-orbital's highest states, two peaks just below  $E_F$  were significantly reduced to almost zero states after adsorption, which indicated electron loss towards the Ni atoms 3d-orbitals. This suggested that the MBTNa collector also adsorbed on Ni atoms through normal covalent bonding. The MBTNa collector vertical adsorption on Fe atoms is shown in Figure 4.10b. It was noted that the Fe 3d-orbital changed at the  $E_F$ , where the smooth sharp peak just below the  $E_F$  reduced in states (from 2.0 electrons/eV to just above 1.0 electrons/eV). Interestingly, the peak just above the  $E_F$  increased in states suggesting electron loss to the S atom 3p-orbital. The S1 3p-orbital two highest states peaks just below the  $E_F$  significantly reduced states and formed multiple split peaks. Furthermore, the peaks at the CB moved towards the  $E_F$  after adsorption, with slight raised states at the  $E_F$ . This suggested that the S1 atom gained electrons from the Fe 3d-orbital, forming a back-donation covalent bond. There is a change in the PDOS of S1 after adsorption; the p-orbital dropped in state at the  $E_F$  suggesting that it lost electrons during adsorption. These observations suggest that there was a direct interaction between the d-orbital of Ni and Fe with the p-orbital of S1, with the Fe and S1 d- and p-orbital being more reactive. In Figure 4.10(b) the state of Fe with S1 decreased after adsorption, suggesting that Fe lost electrons during adsorption. S1 on Fe also decreased in

state after adsorption, suggesting a loss of electrons during adsorption. These observations suggest that MBTNa performs poorly when placed vertically on the surface.

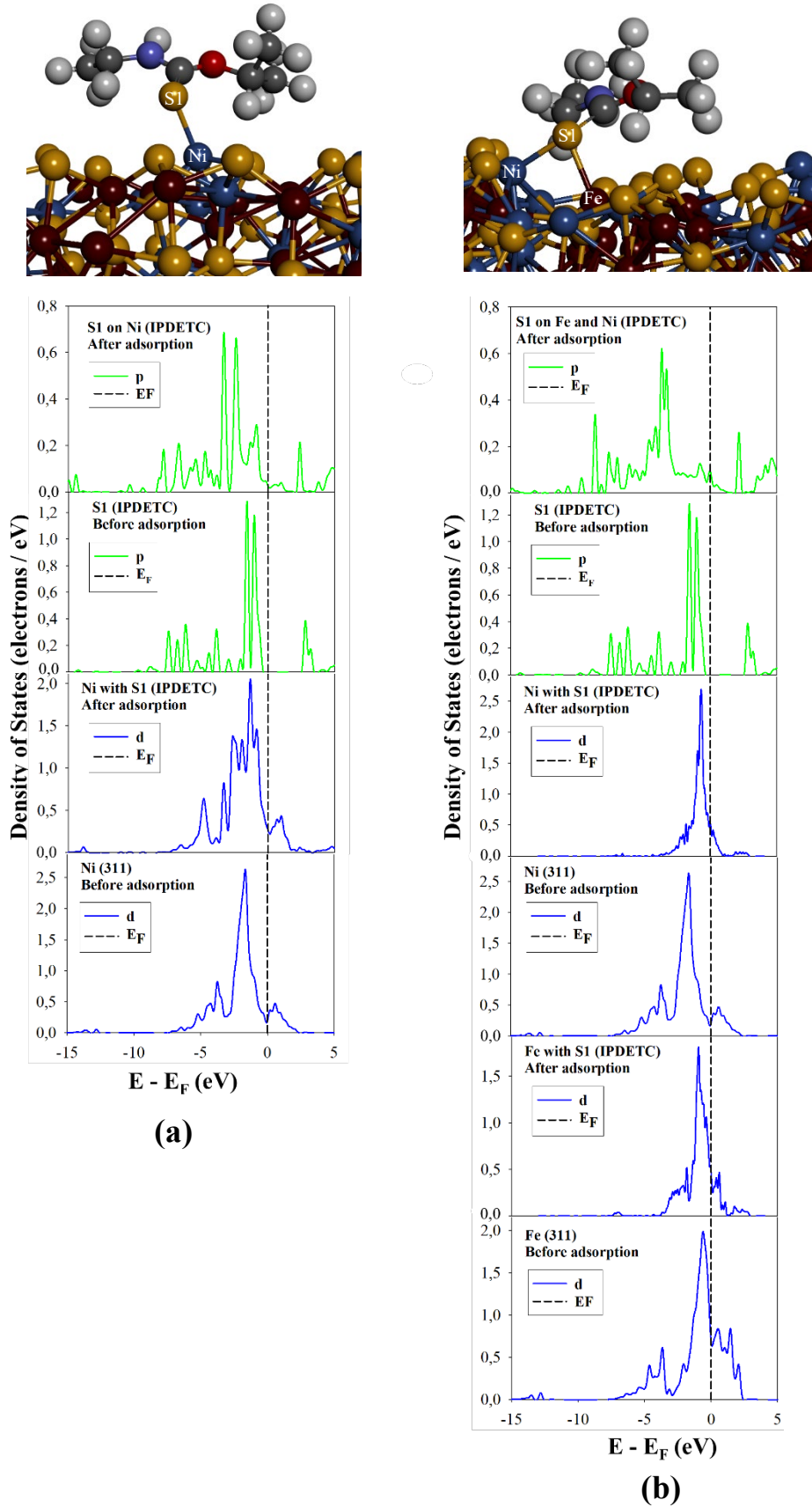


Figure 4.9: Partial density of states (PDOS) of IPEDTC collector before and after adsorption on  $\text{Fe}_5\text{Ni}_4\text{S}_8$  (311) surface: (a) Ni site adsorption and (b) Fe site adsorption.

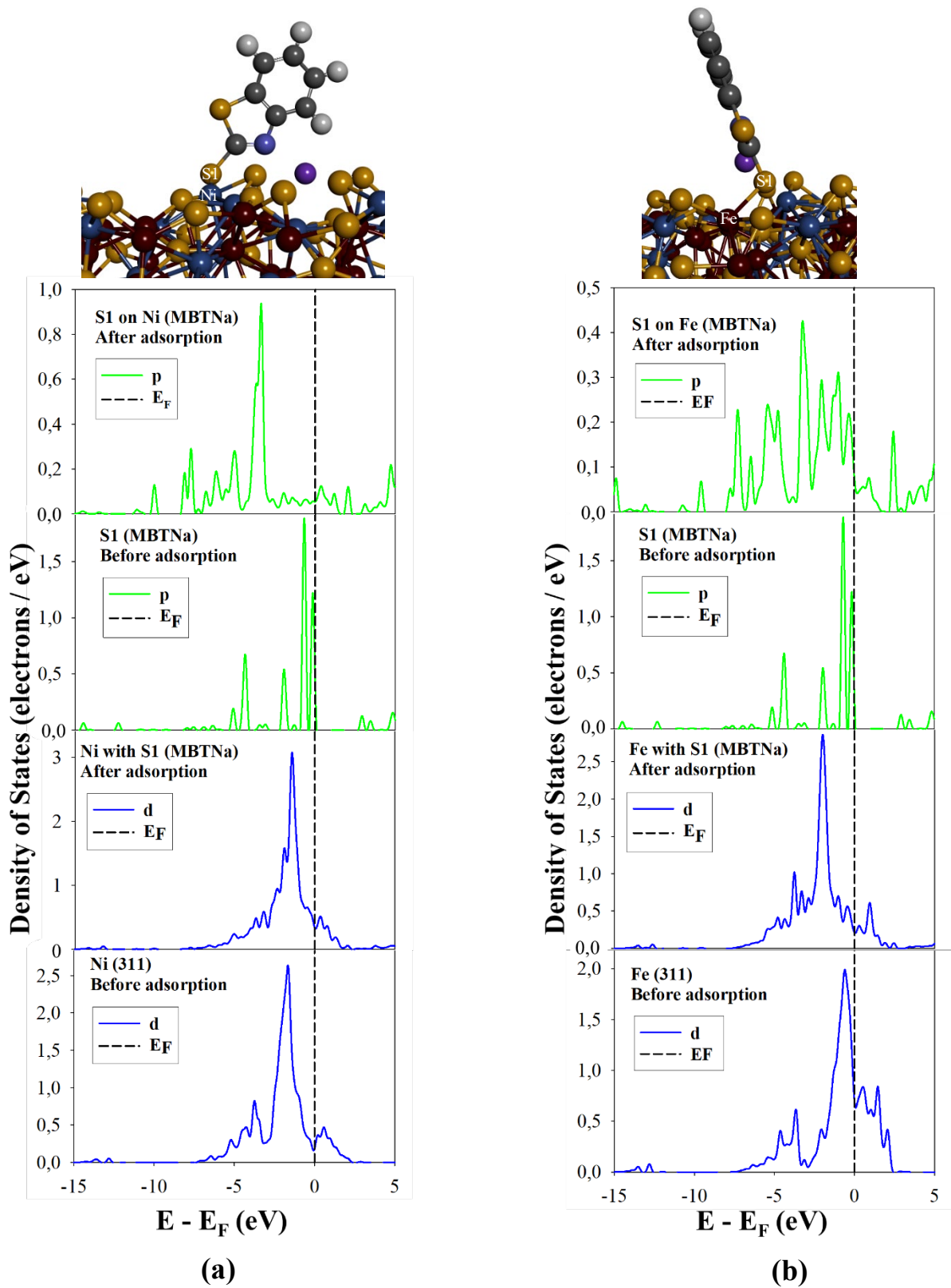


Figure 4.10: Partial density of states (PDOS) of MBTNa collector before and after adsorption on  $\text{Fe}_3\text{Ni}_4\text{S}_8$  (311) surface: (a) Ni site adsorption and (b) Fe site adsorption.

For the MBTNa collector placed horizontally on the surface in Figure 4.11 (a) and (b), the p-orbital of S1 p-orbital dropped in state after adsorption at the  $E_F$ , suggesting that it lost electrons during adsorption. It was noted that Ni with the S1 after the adsorption state at the  $E_F$  is higher than that of a clean surface, suggesting that Ni gained electrons in Figure 4.11(a).

The PDOS for MBTNa collector horizontal adsorption on Fe and Ni atoms is shown in Figure 4.11. In Figure 4.11a the PDOS of horizontal adsorption of MBTNa collector on Ni site was examined. It was observed that Ni atoms 3d-orbitals changed just below the  $E_F$  where the sharp peak forms a minor split; however, it resulted an increase in states. Interestingly, at the  $E_F$  the peak at the CB shifts towards the VB, whereby the small peak is completely moved to the VB. This suggested electron gain from the S atoms. The S1 3p-orbital's highest states, two peaks just below  $E_F$  were significantly reduced states after adsorption, with some states at the  $E_F$  shifting towards the CB. This indicated electron loss towards the Ni atoms 3d-orbitals. This suggested that the MBTNa collector also adsorbed on Ni atoms through normal covalent bonding. The MBTNa collector horizontal adsorption on Fe atoms is shown in Figure 4.10b. It was noted that the Fe 3d-orbital changed at the  $E_F$ , where the smooth sharp peak just below the  $E_F$  reduced in states (from 2.0 electrons/eV to just above 1.0 electrons/eV). Interestingly, the peak just above the  $E_F$  increased in states suggesting electron loss to the S atom 3p-orbital. The S2 3p-orbital's two highest states peaks just below the  $E_F$  significantly reduced states and formed multiple split peaks. Furthermore, the peaks at the CB moved towards the  $E_F$  after adsorption, with slight raised states at the  $E_F$ . This suggested that the S2 atom gained electrons from the Fe 3d-orbital, forming a back-donation covalent bond.

The PDOS for SDTBAT collector adsorption on Fe and Ni atoms is shown in Figure 4.12. In Figure 4.10a the PDOS of the SDTBAT collector on the Ni site was examined. It was observed that Ni atoms 3d-orbitals changed just below the  $E_F$  where the sharp peak formed broad splitting peaks and reduced states. In addition, at the  $E_F$ , the states shifted to the CB, suggesting electron loss towards the S atoms. The S1 3p-orbital's highest states two peaks just below  $E_F$  significantly reduced states after adsorption, with some states raised at the  $E_F$ , which indicated electron gain from the Ni atoms 3d-orbitals. This suggested that the SDTBAT collector adsorbed on Ni atoms through back-donation covalent bonding. The SDTBAT collector adsorption on Fe atoms is shown in Figure 4.12b. It was noted that the Fe 3d-orbital changed at the  $E_F$ , where the sharp peak just below the  $E_F$  reduced in states (from 2.0 electrons/eV to below 1.5 electrons/eV). Interestingly, the peak just above the  $E_F$  significantly increased in states to above the peak at the CV, suggesting electron loss to the S

atom 3p-orbital. The S1 3p-orbital's two highest states peaks just below the  $E_F$  significantly reduced states and moved towards the lower energy with raised states at the  $E_F$ . This suggested that the S1 atom gained electrons from the Fe 3d-orbital, forming a back-donation covalent bond.

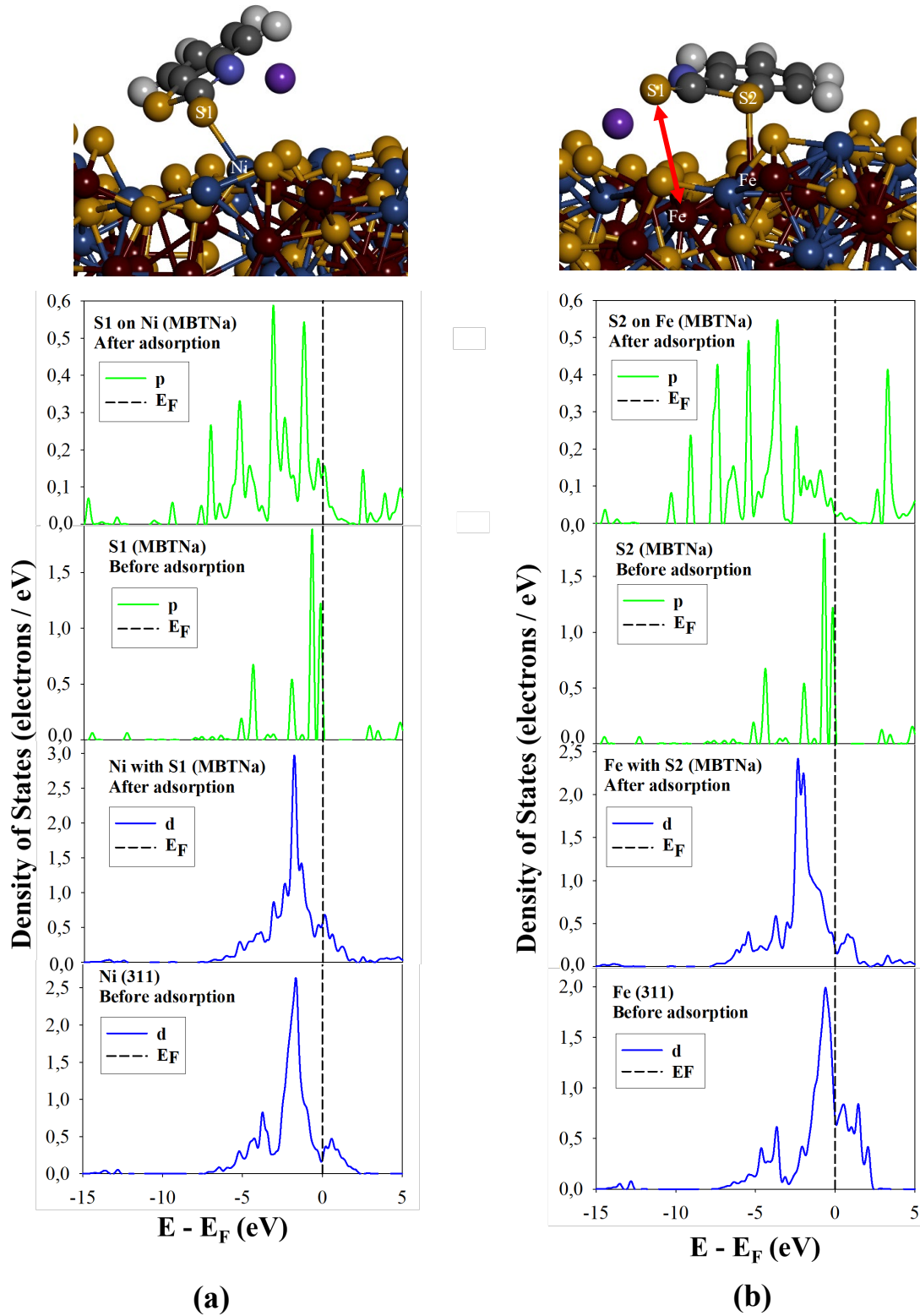


Figure 4.11: Partial density of states (PDOS) of MBTNa collector before and after adsorption on  $\text{Fe}_5\text{Ni}_4\text{S}_8$  (311) surface: (a) Ni site adsorption and (b) Fe site adsorption.

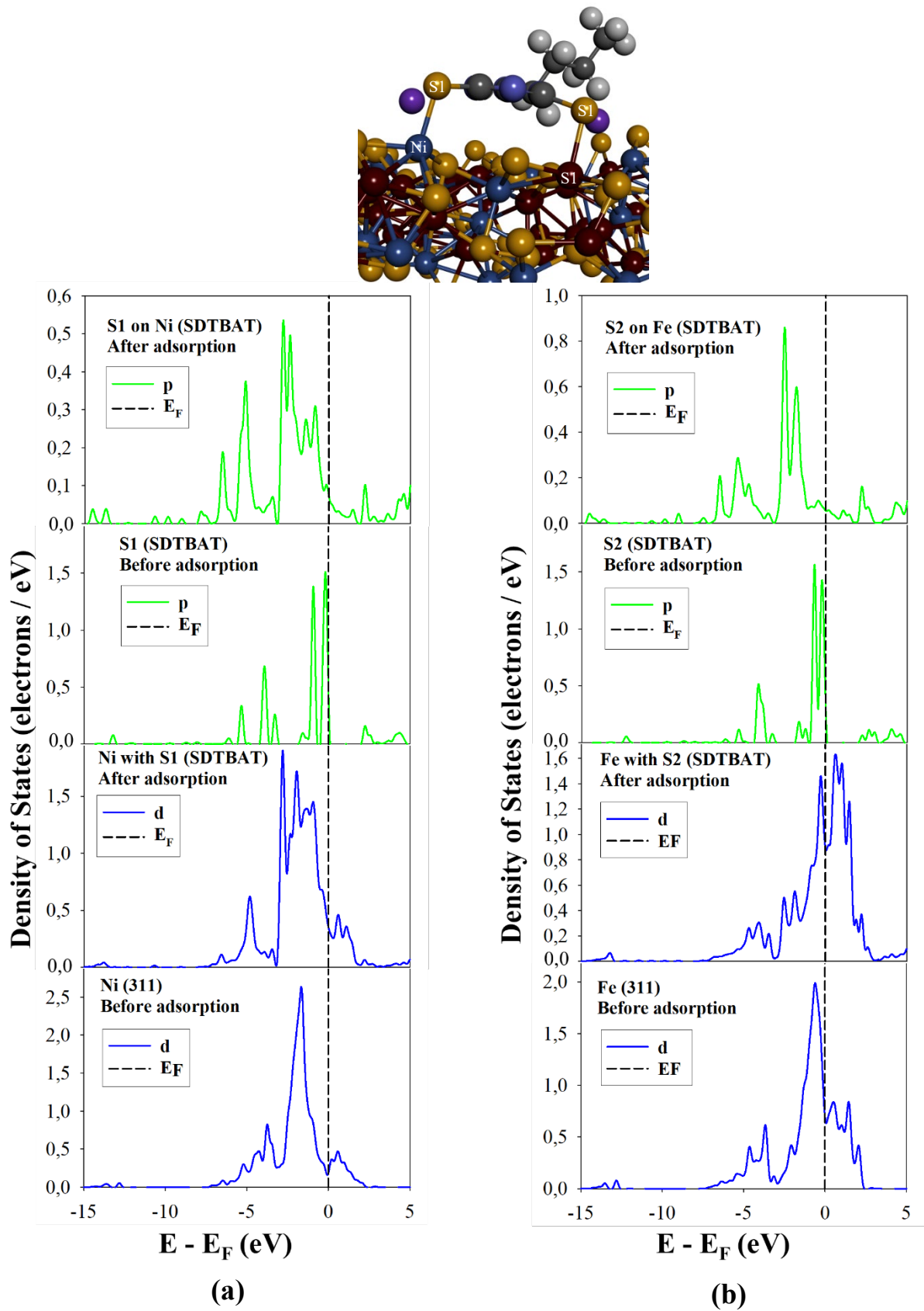


Figure 4.12: Partial density of states (PDOS) of STDBAT collector before and after adsorption on  $\text{Fe}_5\text{Ni}_4\text{S}_8$  (311) surface: (a) Ni site adsorption and (b) Fe site adsorption.

## 4.4 Summary

The adsorption of collectors on the  $\text{Fe}_5\text{Ni}_4\text{S}_8$  (311) surfaces was studied to assess their affinity for these surfaces. The calculated HOMO and LUMO energies for the isolated collectors revealed that the electron-donating capability followed the order:  $\text{SDTBAT} > \text{MBTNa} > \text{ADEDTC} > \text{IPDETC}$ , while the electron-accepting ability follows the order:  $\text{MBTNa} > \text{SDTBAT} > \text{ADEDTC} > \text{IPDETC}$ . The H-L gap reactivity predicted the order to decrease as:  $\text{SDTBAT} > \text{ADEDTC} > \text{MBTNa} > \text{IPDETC}$ . The PDOS showed that the S atoms dominated the EF and therefore the most active sites of the collectors.

Various adsorption sites on the mineral surfaces were explored to identify the most stable, exothermic site. The IPDETC, ADEDTC, MBTNa and SDTBAT collectors were adsorbed on the Fe and Ni sites. It was found that all collectors preferred the Ni sites compared to the Fe sites. This suggested that the collectors were highly selective towards Ni, which indicates pentlandite selectivity. The adsorption energies were depicted to follow the decreasing adsorption strength as:  $\text{ADEDTC} (-460.58 \text{ kJ/mol}) > \text{MBTNa} (-424.08 \text{ kJ/mol}) > \text{SDTBAT} (-352.481 \text{ kJ/mol}) > \text{IPDETC} (-164.53 \text{ kJ/mol})$ . It was evident that ADEDTC gave much stronger exothermic adsorption energy amongst the collectors. The PDOS of the adsorbed surface indicated that in most instances the collector S atoms donated electrons to the Fe or Ni atoms on the surface, which suggested the formation of a normal covalent bond.

# **CHAPTER 5**

## **Summary and Conclusion**

The study explored the interaction of ADEDTC, IPDETC, MBTNa and novel SDTBAT collectors on Fe<sub>5</sub>Ni<sub>4</sub>S<sub>8</sub> (311) mineral surfaces. The quantum mechanical first principle density functional theory with dispersion correction by the Grimme method was employed as implemented in the VASP code.

Full geometry optimisation of bulk model was performed and the cut-off energies needed to converge the total energy of the Fe<sub>5</sub>Ni<sub>4</sub>S<sub>8</sub> bulk structure were determined. The bulk model converged from the cut-off energy of 400 eV, which was adopted in the study. The k-points of 8×8×6 were found to be sufficient to converge the total energy of the Fe<sub>5</sub>Ni<sub>4</sub>S<sub>8</sub> bulk model. The 4×4×1 k-points were found sufficient to converge the total energies of the surfaces. The optimised bulk Fe<sub>5</sub>Ni<sub>4</sub>S<sub>8</sub> pentlandite had lattice dimensions of a = b = 7.020 Å and c = 9.930 Å, and the angles between the cell faces were α = β = λ = 90° with a space group P4<sub>2</sub>/nmc. Its primitive lattice could be multiplied by a = b = 7.020 Å×√2 = 9.930 Å, which showed that the cluster expansion generated structure possessed both primitive and conventional lattice parameters.

The low index (100), (110), (111), (224) and (311) surfaces were cleaved at different terminations, considering non-dipole surfaces for relaxations. The non-dipole surface energies computed for (111), (211), (224) and (311) surfaces were found to be 1.622 J/m<sup>2</sup>, 1.843 J/m<sup>2</sup>, 1.844 J/m<sup>2</sup> and 1.484 J/m<sup>2</sup>, respectively. The (311) surface was found to be the most stable surface since it has the lowest surface energy. The electronic structures (density of states) for Fe<sub>5</sub>Ni<sub>4</sub>S<sub>8</sub> (311) surface showed metallic behaviour since there were no band gaps observed at the E<sub>F</sub>. The case of Fe<sub>5</sub>Ni<sub>4</sub>S<sub>8</sub> (311) surface DOS fell into the pseudo gap, suggesting stability.

The study of collector adsorption on Fe<sub>5</sub>Ni<sub>4</sub>S<sub>8</sub> (311) surface assessed the collectors' affinity for Ni and Fe sites and their selective flotation potential for pentlandite minerals. Analysis of the highest occupied molecular orbital (HOMO) and lowest unoccupied molecular orbital (LUMO) energies showed that SDTBAT had the highest electron-donating capability, while MBTNa had the highest electron-accepting ability. Adsorption calculations revealed that all collectors preferred Ni sites over Fe sites. The computed adsorption energies strength was found to decrease as follows: ADEDTC > MBTNa > SDTBAT > IPDETC. This indicated that the ADEDTC had strong adsorption amongst the collector, and therefore the best collector for pentlandite. The dispersion energies were ranked as: SDTBAT > MBTNa > ADEDTC > IPDETC, which highlighted hydrocarbon chain interactions as influential in collector performance.

Projected density of states (PDOS) analysis for each collector corroborated these adsorption trends. ADEDTC formed covalent bonds with Ni, resulting in electron gain from S atoms, while it induced electron loss on Fe. The IPDETC collector adsorption was bonded on both Fe and Ni, whereby the Ni atoms lost electrons, while the Fe atoms gained electrons. The PDOS of IPDETC S atoms after adsorption showed that the 3p-orbital lost electrons to the metals. MBTNa's vertical adsorption displayed weak bonding on Fe atoms, while horizontal adsorption enhanced electron transfer to Ni, indicating stronger interaction. SDTBAT on Ni demonstrated extensive electron transfer to S atoms, forming a strong back-donation covalent bond.

In conclusion, the collectors displayed a strong preferential bonding with Ni atoms over Fe atoms. Furthermore, the ADEDTC collector gave the strongest adsorption ( $-460.581$  kJ/mol) on pentlandite surface. These findings affirm that the ADEDTC is the best collectors' for selective flotation of pentlandite. Moreover, the IPDETC collector also has the potential for flotation separation of pentlandite. As such both ADEDTC and IPDETC collectors are recommended for selective flotation of pentlandite from gangue minerals as sole collectors or as co-collectors. These predictions will benefit the mining sector in South African, in particular the mineral processing industry on the processing and improving the recovery of the pentlandite minerals for beneficiation of nickel metal.

## **Recommendations and future work**

This dissertation investigated the adsorption of ADEDTC, IPDETC, MBTNa and SDTBAT collectors on  $\text{Fe}_5\text{Ni}_4\text{S}_8$  (311) surfaces using density functional theory with dispersion corrections, highlighting their use as collectors for pentlandite. The literature review identified several information gaps, some of which were addressed by this study, while others remain. Notably, molecular dynamics simulations are needed to assess the effect of temperature on collector adsorption, and examining adsorption on oxidised surfaces is crucial to understanding the behaviour of oxidised pentlandite minerals.

The findings of this dissertation have opened areas for additional research, such as investigating the introduction of impurities on the surfaces. This raises the question of how impurity substitution in the bulk and surface structures could impact or improve structural stability. Understanding this would help explain the possible reasons for decreased flotation efficiency in pentlandite minerals. The study explored the interactions between thionocarbamate, heterocyclic and a novel s-triazine collector on pentlandite surfaces. These

results are critical for predicting the affinity and floatability of the pentlandite minerals. In addition the aspects of electron structures as Bader charges and charge density difference are crucial to unravel the chemistry bonding of the collectors and are proposed for future work.

The computational methods used in this study, which examine bulk and surface adsorption with collectors, are essential for understanding the recovery of pentlandite minerals. These techniques can also be applied to other base metal sulphides (BMS), laying the groundwork for assessing water's impact on collector adsorption and the development of novel collectors to potentially replace widely used ones. The reliability of these adsorption predictions is supported by the outcomes that have been found for chalcopyrite using these collectors, in particular the ADEDTC, IPDETC and MBTNa collectors. As such both ADEDTC and IPDETC collectors are recommended for selective flotation of pentlandite from gangue minerals as sole collectors or as co-collectors.

## References

- [1] S. K. Haldar, 'Mineral Exploration: Principles and Applications', Elsevier, ch. 13, pp. 259–290, 2018.
- [2] B. Mishra, 'Cobalt and Nickel Production', Elsevier, pp. 1288–1294, 2001.
- [3] S. J. Barnes, 'The Occurrence and Origin of Pentlandite-Chalcopyrite-Pyrrhotite Loop Textures in Magmatic Ni-Cu Sulfide Ores', *Economic Geology*, vol. 115, pp. 1777–1798, 2020.
- [4] M. A. Mehlape, P. E. Ngoepe, and S. C. Parker, 'Computational studies of the bulk cobalt pentlandite (Co<sub>9</sub>S<sub>8</sub>): Validation of the potential model', 2013.
- [5] R. T. Jones, "Platinum smelting in South Africa", vol. 95. *South African journal of science*, vol. 95, pp. 525–534, 1999.
- [6] L. J. Cabri, "Platinum group elements: Mineral, geology and recovery", Canadian institution on mining and metallurgy, 1989.
- [7] S. K. Haldar, "Introduction in Platinum-Nickel-Chromium Deposits", Elsevier, pp. 1–35, 2017.
- [8] H. V. Eales and R. G. Cawthorn, 'The Bushveld Complex', pp. 181–229, 1996.

- [9] M. Junge, R. Wirth, T. Oberthür, F. Melcher, and A. Schreiber, “Mineralogical siting of platinum-group elements in pentlandite from the Bushveld Complex, South Africa”, *Miner Depos*, vol. 50, pp. 41–54, 2015.
- [10] A. T. Makanza, M. K. G. Vermaak, and J. C. Davidtz, “The flotation of auriferous pyrite with a mixture of collectors”, *Int J Miner Process*, vol. 86, pp. 85–93, 2008.
- [11] B. Meyer, “The Pseudopotential Plane Wave Approach”, *Computational Nanoscience*, vol. 31, pp. 71–83, 2006.
- [12] W. A. Ngobeni and G. Hangone, “The effect of using sodium di-methyl-dithiocarbamate as a co-collector with xanthates in the froth flotation of pentlandite containing ore from nkomati mine in south Africa”, *Miner Eng*, vol. 54, pp. 94–99, 2013.
- [13] R.S. Smart, J. Amarantidis, W. M. Skinner, C.A. Prestidge, L. La Vanier and S. R. Grano, “Surface analytical studies of oxidation and collector adsorption in sulfide mineral flotation”, *Scanning Microscopy International*, vol. 12, pp. 3–62, 2003.
- [14] T. Inoue, “Mineral comminution and separation” *Civil Engineering*, vol. 11, p. 248, 2009.
- [15] P. Pawliszak, B. H. Bradshaw-Hajek, W. Skinner, D. A. Beattie, and M. Krasowska, “Frothers in flotation: A review of performance and function in the context of chemical classification”, *Miner Eng*, vol. 207, 2024.
- [16] M. S. Manono, K. Matibidi, I. O. Otunniyi, C. K. Thubakgale, K. C. Corin, and J. G. Wiese, “The Behaviour of Mixtures of Sodium Iso-Butyl Xanthate and Sodium Di-Ethyl Dithiophosphate during the Flotation of a Cu-Ni-Pt Ore in Degrading Water Quality”, *Minerals*, vol. 10, p. 123, 2020.
- [17] G. Marape, “Fundamental electrochemical behaviour of pentlandite”, University of Pretoria (South Africa), 2010.
- [18] P. P. Mkhonto, L. Lu, W. Xiong, Y. Zhu, L. Han and P. E. Ngoepe, “Adsorption mechanisms and effects of thiocarbamate collectors in the separation of chalcopyrite from pyrite minerals: DFT and experimental studies”, *Miner Eng*, vol. 176, pp. 1–14, 2022.
- [19] X. Zhang W. Xiong, L. Lu, Z. Qian, Y. Zhu, P. P. Mkhonto, Y. Zheng, L. Han and P. E. Ngoepe, “A novel synthetic polymer depressant for the flotation separation of

- chalcopyrite and galena and insights into its interfacial adsorption mechanism”, *Sep Purif Technol*, vol. 279, p. 119658, 2021,
- [20] W. Maree, L. Kloppers, G. Hangone, and O. Oyekola, “The effects of mixtures of potassium amyl xanthate (PAX) and isopropyl ethyl thionocarbamate (IPETC) collectors on grade and recovery in the froth flotation of a nickel sulfide ore”, *S Afr J Chem Eng*, vol. 24, pp. 116–121, 2017.
- [21] G. S. Maier and B. Dobiáš, “2-mercaptobenzothiazole and derivatives in the flotation of galena, chalcocite and sphalerite: A study of flotation, adsorption and microcalorimetry”, *Miner Eng*, vol. 10, pp. 1375–1393, 1997.
- [22] Y. Feng, S. Chen, H. Zhang, P. Li, L. Wu, and W. Guo, “Characterization of iron surface modified by 2-mercaptobenzothiazole self-assembled monolayers”, *Appl Surf Sci*, vol. 253, pp. 2812–2819, 2006.
- [23] P. P. Mkhonto, X. Zhang, B. McFadzean, J. Taguta, Y. Zhu, L. Han and P. E. Ngoepe, “Incorporating pH into DFT-D+U and microflotation recovery studies on heterocyclic collector-pyrite interactions”, *Sep Purif Technol*, vol. 337, p. 126430, 2024.
- [24] K. B. Molala, P. P. Mkhonto, M. A. Mehlappe, and P. E. Ngoepe, “First principles study on stability of base and precious metals pentlandite-like compounds”, *Theor Chem Acc*, vol. 142, 2023.
- [25] T. S. Manyama, P. P. Mkhonto, X. Zhang, Y. Zhu, and P. E. Ngoepe, “A DFT-D+U study on comparative adsorption of s-triazine with xanthate and dithiocarbamate collectors on dry and hydrated cooperite (101) surface”, *J Mol Liq*, vol. 391, p. 123282, 2023.
- [26] C. N. Waterson, P. A. Tasker, R. Farinato, D. R. Nagaraj, N. Shackleton, and C. A. Morrison, “A Computational and Experimental Study on the Binding of Dithio Ligands to Sperrylite, Pentlandite, and Platinum”, *The Journal of Physical Chemistry C*, vol. 120, pp. 22476–22488, 2016.
- [27] B. D. Ikotun, F. V. Adams, and A. G. Ikotun, “Application of three xanthates collectors on the recovery of nickel and pentlandite in a low-grade nickel sulfide ore using optimum flotation parameters”, *Particulate Science and Technology*, vol. 35, pp. 462–471, 2017.

- [28] P. Mkhonto, H. Chauke, P. E. Ngoepe, P. P. Mkhonto, H. R. Chauke, and P. E. Ngoepe, “The effect of thiol collectors on nickel-rich (110) pentlandite surface using density functional theory”, *Proceedings of SAIP*, pp. 95–100, 2017.
- [29] I. O. Otunniyi, M. Oabile, A. A. Adeleke, and P. Mendonidis, “Copper activation option for a pentlandite–pyrrhotite–chalcopyrite ore flotation with nickel interest”, *International Journal of Industrial Chemistry*, vol. 7, pp. 241–248, 2016.
- [30] J. He, Y. Cao, X. Jiang, S. Xu, R. Zheng, W. Sun, and Z. Gao, “Unveiling the adsorption mechanism of xanthate on the pentlandite/pyrrhotite heterostructure from first principles calculations”, *Applied Surface Science*, vol. 616, p. 156480, 2023.
- [31] M. Zhou, Z. Wang, K. Zhao, C. Yao, R. Chen, X. Huang, S.S. Safarov, and K.I. Kholov, “Combined collector based on N-propyl-N-allyl-o-isobutyl thiocarbamate improving the flotation of pentlandite”, *Minerals Engineering*, vol. 227, p. 109256, 2025.
- [32] S. K. Halder, “*Mineral Processing in Mineral Exploration*”, Elsevier, pp. 259–290, 2018.
- [33] D. Bunyak, “To Float or Sink: A Brief History of Flotation milling”, vol. 7, pp. 35–44, 2000.
- [34] A. Flow and F. Rate, “1.1 Froth Flotation-Fundamental Principles”.
- [35] S. Janishar Anzoom, G. Bournival, and S. Ata, “Coarse particle flotation: A review”, Elsevier Ltd, 2024.
- [36] S. M. Bulatovic, “*Handbook of flotation reagents: chemistry, theory and practice*”, Elsevier, 2007.
- [37] D. Lerch, O. Wieckhorst, G. L. W. Hart, R. W. Forcade, and S. Müller, “UNCLE: a code for constructing cluster expansions for arbitrary lattices with minimal user-input”, *Model Simul Mat Sci Eng*, vol. 17, p. 055003, 2009.
- [38] K. B. Molala, P. P. Mkhonto, M. A. Mehlape, and P. E. Ngoepe, “A DFT and cluster expansion study of  $(\text{Fe,Ni})_9\text{S}_8$  pentlandite and unravelling doping with Mn, Co, Cu and precious metals”, *Mater Chem Phys*, vol. 331, p. 130146, 2025.

- [39] T. van Mourik, M. Bühl, and M.-P. Gaigeot, “Density functional theory across chemistry, physics and biology”, *Philosophical Transactions of the Royal Society A: Mathematical, Physical and Engineering Sciences*, vol. 372, p. 20120488, 2014.
- [40] G. Vignale, M. Rasolt, and D. J. W. Geldart, “Magnetic Fields and Density Functional Theory”, pp. 235–253, 1990.
- [41] P. Hohenberg and W. Kohn, “Inhomogeneous Electron Gas”, *Physical Review*, vol. 136, pp. B864–B871, 1964.
- [42] W. Kohn and L. J. Sham, “Self-Consistent Equations Including Exchange and Correlation Effects”, *Physical Review*, vol. 140, pp. A1133–A1138, 1965.
- [43] M. C. Payne, M. P. Teter, D. C. Allan, T. A. Arias, and J. D. Joannopoulos, “Iterative minimization techniques for *ab initio* total-energy calculations: molecular dynamics and conjugate gradients”, *Rev Mod Phys*, vol. 64, pp. 1045–1097, Oct. 1992.
- [44] Sherrill C.D, “Introduction to Density Functional Theory”, Georgia, pp. 134–145, 2004.
- [45] Y. Kudoh and A. H. Tekeda, “Local approximation for the exchange correlation energy of an electronic system”, *Physical Chemical Mineral*, vol. 13, pp. 233–237, 1986.
- [46] D. Mkhonto, P. E. Ngoepe, T. G. Cooper, and N. H. de Leeuw, “A computer modelling study of the interaction of organic adsorbates with fluorapatite surfaces”, *Phys Chem Miner*, vol. 33, pp. 314–331, 2006.
- [47] J. P. Perdew, K. Burke, and Y. Wang, “Generalized gradient approximation for the exchange-correlation hole of a many-electron system”, *Phys Rev B*, vol. 54, pp. 16533–16539, 1996.
- [468] J. C. Cuevas, “Introduction to Density Functional Theory”, Universität Karlsruhe, 2010.
- [49] J. P. Perdew, K. Burke, and M. Ernzerhof, “Generalized Gradient Approximation Made Simple”, *Phys Rev Lett*, vol. 77, pp. 3865–3868, 1996.
- [50] Q. Wu and W. Yang, “Empirical correction to density functional theory for van der Waals interactions”, *J Chem Phys*, vol. 116, pp. 515–524, 2002.

- [51] T. Sato, T. Tsuneda, and K. Hirao, “A density-functional study on  $\pi$ -aromatic interaction: Benzene dimer and naphthalene dimer”, *J Chem Phys*, vol. 123, 2005.
- [52] I.G. Kaplan, “Intermolecular Interactions: Physical Picture, Computational Methods, and Model Potentials” Canada: Wiley & Sons, 2006.
- [53] S. Grimme, S. Ehrlich, and L. Goerigk, “Effect of the damping function in dispersion corrected density functional theory”, *J Comput Chem*, vol. 32, pp. 1456–1465, 2011.
- [54] A. Tkatchenko and M. Scheffler, “Accurate Molecular Van Der Waals Interactions from Ground-State Electron Density and Free-Atom Reference Data”, *Phys Rev Lett*, vol. 102, p. 073005, 2009.
- [55] M. D. Segall, “Ab initio study of biological system”, Doctoral dissertation, University of Cambridge, 1997.
- [56] N. W. Ashcroft and N. D. Mermin, “Solid state physics”, *Phys Rev B*, vol. 13, pp. 27–32, 1976.
- [57] M. L. Cohen and Heine V, “Solid state physics”, *Phys Rev B*, vol. 24, pp. 627–629, 1970.
- [58] D. Vanderbilt, “Soft self-consistent pseudopotentials in a generalized eigenvalue formalism”, *Phys Rev B*, vol. 41, pp. 7892–7895, 1990.
- [59] D. J. Chadi and M. L. Cohen, “Special Points in the Brillouin Zone”, *Phys Rev B*, vol. 8, pp. 5747–5753, 1973.
- [60] H. J. Monkhorst and J. D. Pack, “Special points for Brillouin-zone integrations”, *Phys Rev B*, vol. 13, pp. 5188–5192, 1976.
- [61] G. Kresse and J. Furthmüller, “Efficient iterative schemes for *ab initio* total-energy calculations using a plane-wave basis set”, *Phys Rev B*, vol. 54, pp. 11169–11186, 1996.
- [62] P. E. Blöchl, “Projector augmented-wave method”, *Phys Rev B*, vol. 50, pp. 17953–17979, 1994.
- [63] Kresse G, “VASP group, theoretical physics departments, Vienn”, *Phys Rev B*, vol. 84, pp. 2780–2785, 2011.

- [64] W. Kohn and L. J. Sham, “Self-Consistent Equations Including Exchange and Correlation Effects”, *Physical Review*, vol. 140, pp. A1133–A1138, 1965.
- [65] P. Hohenberg and W. Kohn, “Inhomogeneous Electron Gas”, *Physical Review*, vol. 136, pp. B864–B871, 1964.
- [66] H. J. Monkhorst and J. D. Pack, “Special points for Brillouin-zone integrations”, *Phys Rev B*, vol. 13, pp. 5188–5192, Jun. 1976.
- [67] D. N. Basov, F. S. Pierce, P. Volkov, S. J. Poon, and T. Timusk, “Optical Conductivity of Insulating Al-Based Alloys: Comparison of Quasiperiodic and Periodic Systems”, *Phys Rev Lett*, vol. 73, pp. 1865–1868, 1994.
- [68] A. Matsuda, S. Sugita, T. Fujii, and T. Watanabe, “Study of pseudogap phenomena by STM and other probes”, *Journal of Physics and Chemistry of Solids*, vol. 62, pp. 65–68, 2001.
- [69] Y. N. Gornostyrev, O. Y. Kontsevoi, A. F. Maksyutov, A. J. Freeman, M. I. Katsnelson, A. V. Trefilov and A. I. Lichtenshtein, “Negative yield stress temperature anomaly and structural instability of Pt<sub>3</sub>Al”, *Phys Rev B*, vol. 70, p. 014102, 2004.
- [70] D. A. Pankhurst, D. Nguyen-Manh, and D. G. Pettifor, “Electronic origin of structural trends across early transition-metal disilicides: Anomalous behavior of CrSi<sub>2</sub>”, *Phys Rev B*, vol. 69, p. 075113, 2004.
- [71] Bader R, “Atoms in molecules: A quantum theory”, New York: Oxford University Press., 1990.
- [72] G. L. Gutsev, B. K. Rao, and P. Jena, “Systematic Study of Oxo, Peroxo, and Superoxo Isomers of 3d-Metal Dioxides and Their Anions”, *J Phys Chem A*, vol. 104, pp. 11961–11971, 2000.
- [73] A. Hung, I. Yarovsky, and S. P. Russo, “Density-functional theory studies of xanthate adsorption on the pyrite FeS<sub>2</sub>(110) and (111) surfaces”, *J Chem Phys*, vol. 118, pp. 6022–6029, 2003.
- [74] P. L. A Popelier., “MORPHY98, a program written by P.L.A. Popelier with a contribution from R.G.A. Bone”, UMIST, Manchester, England, 1998.

- [75] B. B. Stefanov and J. Cioslowski, “An efficient approach to calculation of zero-flux atomic surfaces and generation of atomic integration data”, *J Comput Chem*, vol. 16, pp. 1394–1404, 1995.
- [76] F. De Proft, C. Van Alsenoy, A. Peeters, W. Langenaeker, and P. Geerlings, “Atomic charges, dipole moments, and Fukui functions using the Hirshfeld partitioning of the electron density”, *J Comput Chem*, vol. 23, pp. 1198–1209, 2002.
- [77] N. O. J. Malcolm and P. L. A. Popelier, “An improved algorithm to locate critical points in a 3D scalar field as implemented in the program MORPHY”, *J Comput Chem*, vol. 24, pp. 437–442, 2003.
- [78] S. Noury, X. Krokidis, F. Fuster, and B. Silvi, “Computational tools for the electron localization function topological analysis”, *Comput Chem*, vol. 23, pp. 597–604, 1999.
- [79] B. Silvi and C. Gatti, “Direct Space Representation of the Metallic Bond”, *J Phys Chem A*, vol. 104, pp. 947–953, 2000.
- [80] G. Henkelman, A. Arnaldsson, and H. Jónsson, “A fast and robust algorithm for Bader decomposition of charge density”, *Comput Mater Sci*, vol. 36, pp. 354–360, 2006.
- [81] W. Tang, E. Sanville, and G. Henkelman, “A grid-based Bader analysis algorithm without lattice bias”, *Journal of Physics: Condensed Matter*, vol. 21, p. 084204, 2009.
- [82] J. P. Perdew, K. Burke, and M. Ernzerhof, “Generalized Gradient Approximation Made Simple”, *Phys Rev Lett*, vol. 77, pp. 3865–3868, 1996.
- [83] S. J. Adkins and M. J. Pearse, “The influences of collector chemistry on kinetics and selectivity in base-metal sulphide flotation”, *Miner Eng*, vol. 5, pp. 295–310, 1992.
- [84] K. Molala, M. Mehlape, P. Mkhonto, and P. Ngoepe, “Effect of precious metals (Ru, Rh, Pd, Os, Ir, Pt, Co) on structural, stability and ductility of Fe<sub>5</sub>Ni<sub>4</sub>S<sub>8</sub> (P4<sub>2</sub>/nmc) pentlandite: cluster expansion method”, *MATEC Web of Conferences*, vol. 388, p. 02005, 2023.
- [85] H. R. Chauke, D. Nguyen-Manh, P. E. Ngoepe, D. G. Pettifor, and S. G. Fries, “Electrostatic structure and stability of the pentlandites Co<sub>9</sub>S<sub>8</sub> and (Fe, Ni)<sub>9</sub>S<sub>8</sub>”, *Phys Rev B*, vol. 66, p. 155105, 2002.

- [86] P. P. Mkhonto, H. R. Chauke, and P. E. Ngoepe, “Ab initio studies of o<sub>2</sub> adsorption on (110) nickel-rich pentlandite (Fe<sub>4</sub>Ni<sub>5</sub>S<sub>8</sub>) mineral surface”, *Minerals*, vol. 5, pp. 665–678, 2015.
- [87] J. Xu, Y. Ma, J. Wang, X. Guo, L. Gong, Y. Zhu and C. Xuan, “Constructing defect-rich Ni<sub>9</sub>S<sub>8</sub>/Fe<sub>5</sub>Ni<sub>4</sub>S<sub>8</sub> heterostructure nanoparticles for efficient oxygen evolution reaction and overall water splitting”, *JPhys Materials*, vol. 4, Jul. 2021.
- [88] T. P. A. and M. C. A. Waterson C.N., “Design, synthesis and testing of reagents for high-value mineral collection”, Edinburgh, 2015.
- [89] Gibbs J.W., “The collected works of J. Willard Gibbs”, Longmans, 1928.
- [90] L. Lu, S. Yu, and H. Tian, “Theoretical insight into surface structures of pentlandite toward hydrogen evolution”, *J Colloid Interface Sci*, vol. 607, pp. 645–654, 2022.
- [91] B. Delley, “Density Functional Theory Electronic Structure Program”, *J. Chem. Phys*, vol. 113, pp. 7756–7764, 2000.
- [92] H. Yekeler and M. Yekeler, “Reactivities of some thiol collectors and their interactions with Ag (+1) ion by molecular modelling”, *Appl Surf Sci*, vol. 236, pp. 435–443, 2004.
- [93] G. Klopman, “Chemical reactivity and the concept of charge- and frontier-controlled reactions”, *J Am Chem Soc*, vol. 90, pp. 223–234, 1968.
- [94] J. C. Slater, “Atomic Radii in Crystals”, *J Chem Phys*, vol. 41, pp. 3199–3204, 1964.

## Appendix A: Explanation data of the project

- Project – Computational modelling studies on adsorption of heterocyclic: sodium mercaptobenzothiazole (MBT), novel triazine: sodium 2, 6-dithio-4-butylamino-1, 3, 5-triazine (SDTBAT) and thionocarbamate: O-isopropyl-N-diethyl-thionocarbamate (IPDETC) and S-allyl-N-diethyl-dithiocarbamate (ADEDTC) collectors on Fe<sub>5</sub>Ni<sub>4</sub>S<sub>8</sub> mineral surfaces.

DFT (VASP)	– Density function theory with dispersion correction method implemented in Vienna Ab initio simulation Package to study the bulk structures and adsorption of ADEDTC, IPDETC, MBT and SDTBAT collectors on Fe <sub>5</sub> Ni <sub>4</sub> S <sub>8</sub> (311) surfaces.
Bulk structure	– We used Fe <sub>5</sub> Ni <sub>4</sub> S <sub>8</sub> bulk structures to study and investigate structural, electronic properties
Surfaces	– (111), (211), (224) and (311) surfaces were cleaved from to bulk structure to investigate surface stability.
Dry surface adsorptions	– The MBTNa, s-triazine, thionocarbamate and S-allyl dithiocarbamate collector adsorption on dry Fe <sub>5</sub> Ni <sub>4</sub> S <sub>8</sub> (311) surface and describing their chemistry of bonding from electronic properties.

## Appendix B: Papers presented at conferences

- i. University of Limpopo Faculty of Science and Agriculture (FSA) post-graduate research day held at Bolivia Lodge in Polokwane (2022) “Computational study of iron-rich pentlandite (Fe<sub>5</sub>Ni<sub>4</sub>S<sub>8</sub>) surface stabilities”.
- ii. University of Limpopo Faculty of Science and Agriculture (FSA) post-graduate research day held at Bolivia Lodge in Polokwane (2022) “Computational study of iron-rich pentlandite (Fe<sub>5</sub>Ni<sub>4</sub>S<sub>8</sub>) surface stabilities”.
- iii. South African Institute of Physics (SAIP) conference at Richards Bay Campus University of Zululand (2023) “Investigation of Surface Stability and Interaction of Thionocarbamate Collectors on Pentlandite (Fe, Ni)<sub>9</sub>S<sub>8</sub> Mineral Surfaces”.
- iv. University of Limpopo Faculty of Science and Agriculture (FSA) post-graduate research day held at Bolivia Lodge in Polokwane (2023) “Thiocarbamate Collectors Interaction with Pentlandite (Fe, Ni)<sub>9</sub>S<sub>8</sub> Mineral Surfaces”.
- v. Centre for High Performance Computing (CHPC) conference held at Kruger National Park (2023) “Investigation of Surface Stability and Interaction of Thionocarbamate Collectors on Pentlandite (Fe, Ni)<sub>9</sub>S<sub>8</sub> Mineral Surfaces”.

- vi. South African Institute of Physics (SAIP) conference held online (2024) “Computational study on interaction of thionocarbamate, dithiocarbamate and heterocyclic collectors on (311) surface of pentlandite ( $\text{Fe}_5\text{Ni}_4\text{S}_8$ )”.
- vii. University of Limpopo Faculty of Science and Agriculture (FSA) post-graduate research day held at The Ranch Resort in Polokwane (2024) “Computational study on interaction of mercaptobenzothiazole and s-triazine collectors on (311) surface of pentlandite ( $\text{Fe}_5\text{Ni}_4\text{S}_8$ ).”

## Appendix C: Tables

Table C1.1 shows the atomic position (X, Y, Z) for the systems  $\text{Fe}_5\text{Ni}_4\text{S}_8$ .

Property		Value		
Formula		$\text{Fe}_5\text{Ni}_4\text{S}_8$		
Unit cell length (a=b)		$7.020 \text{ \AA} \times \sqrt{2} = 9.930 \text{ \AA}$		
(c)		9.930 $\text{ \AA}$		
Cell angles ( $\alpha=\beta=\gamma$ )		90°		
Space-group		$P4_2/nmc$		
Atoms	Position	X	Y	Z
Fe1 (O)	(2a)	0.750	0.250	0.750
Fe2 (T)	(8g)	0.250	0.498	0.624
Ni1 (T)	(8g)	0.250	0.002	0.876
S1 (l)	(4d)	0.250	0.250	0.000
S2 (l)	(4c)	0.750	0.250	0.000
S3 (f)	(8f)	0.000	0.000	0.000

## Appendix D: ADEDTC, IPDETC, MBT and SDTBAT adsorption on $\text{Fe}_5\text{Ni}_4\text{S}_8$ (311) surface

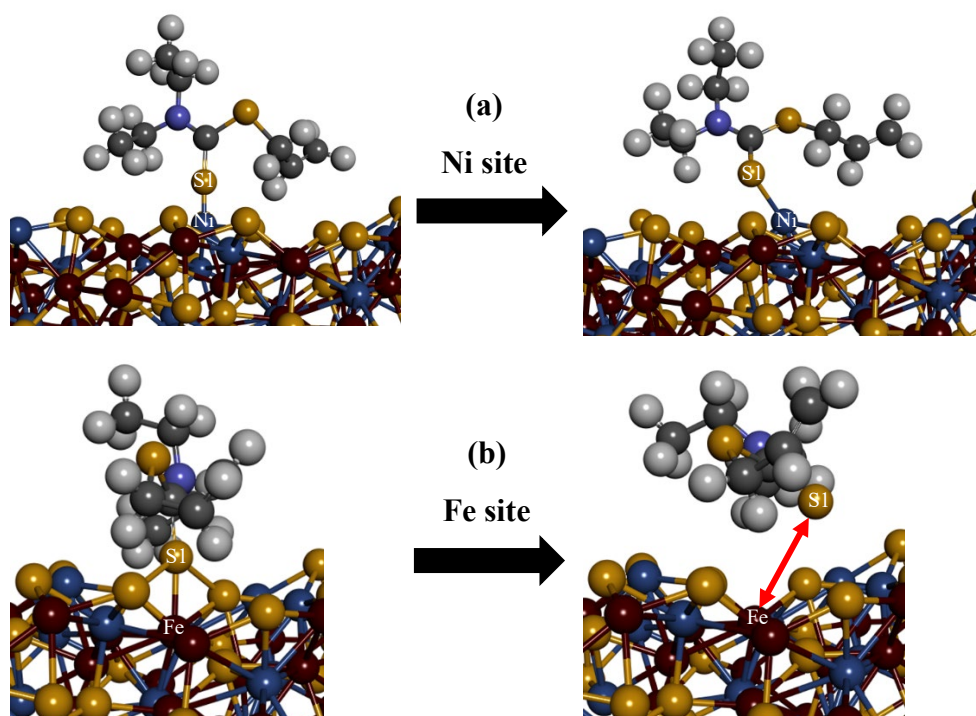


Figure D1.1: The un-relaxed and relaxed ADEDTC collector adsorption on the  $\text{Fe}_5\text{Ni}_4\text{S}_8$  (311) surface.

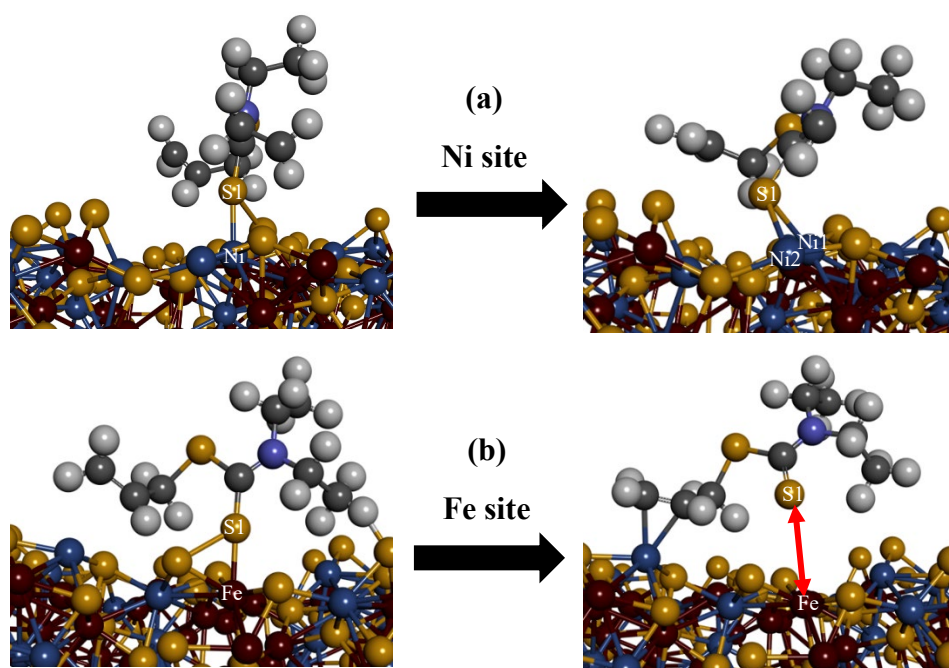


Figure D1.2: The un-relaxed and relaxed ADEDTC collector adsorption on the  $\text{Fe}_5\text{Ni}_4\text{S}_8$  (311) surface.

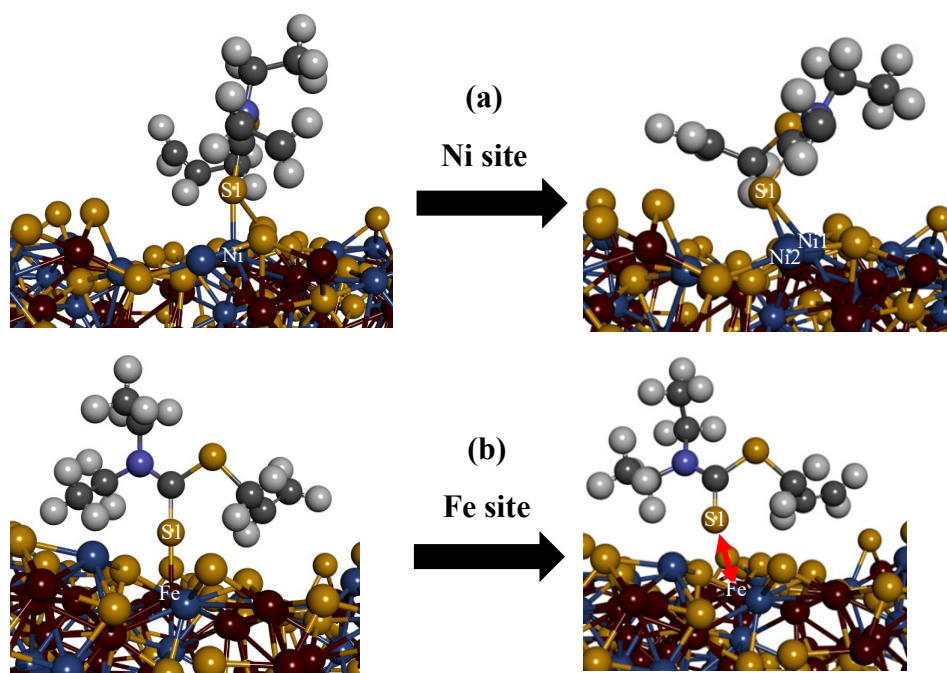


Figure D1.3: The un-relaxed and relaxed ADEDTC collector adsorption on the  $\text{Fe}_5\text{Ni}_4\text{S}_8$  (311) surface.

Table D1.1: The adsorption energies of ADEDTC on the  $\text{Fe}_5\text{Ni}_4\text{S}_8$  (311) mineral surfaces (kJ/mol).

Figure	Adsorption mode	$E_{\text{ads.}}$ (kJ.mol <sup>-1</sup> )	$E_{\text{dis.}}$ (kJ.mol <sup>-1</sup> )	Ni-S1 (Å)	Fe-S1 (Å)	Fe-S2 (Å)
D1.1	Ni-S1	-423.56	-96.40	2.24	-	-
	Fe-S1	-336.51	-55.93	-	3.94	-
D1.2	Ni-S1	-385.03	-123.84	2.37	-	-
	Fe-S1	-370.38	-77.43	-	3.83	-
D1.3	Ni-S1	-640.71	-48.74	3.57	-	-
	Fe-S1	-340.66	-90.14	-	3.91	-

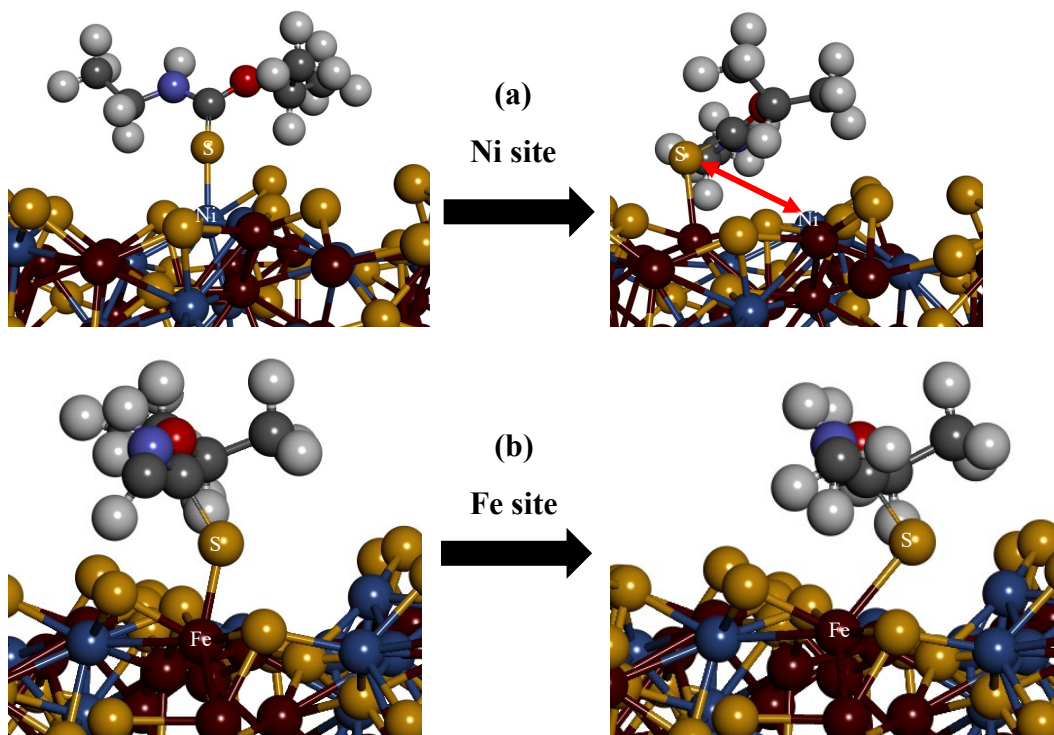


Figure D1.4: The un-relaxed and relaxed IPDETC collector adsorption on the  $\text{Fe}_5\text{Ni}_4\text{S}_8$  (311) surface.

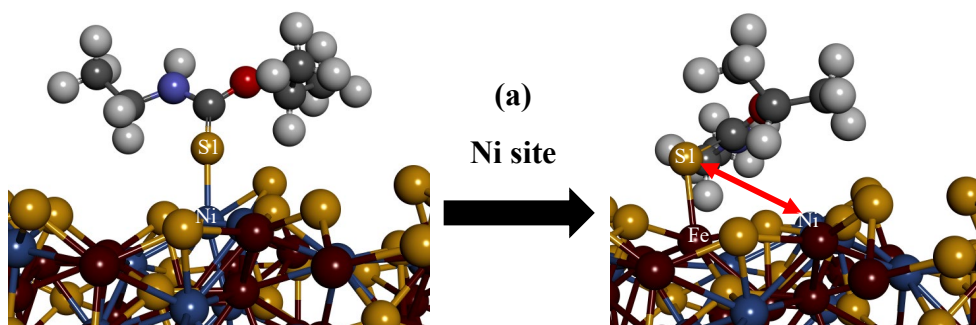


Figure D1.5: The un-relaxed and relaxed IPDETC collector adsorption on the  $\text{Fe}_5\text{Ni}_4\text{S}_8$  (311) surface.

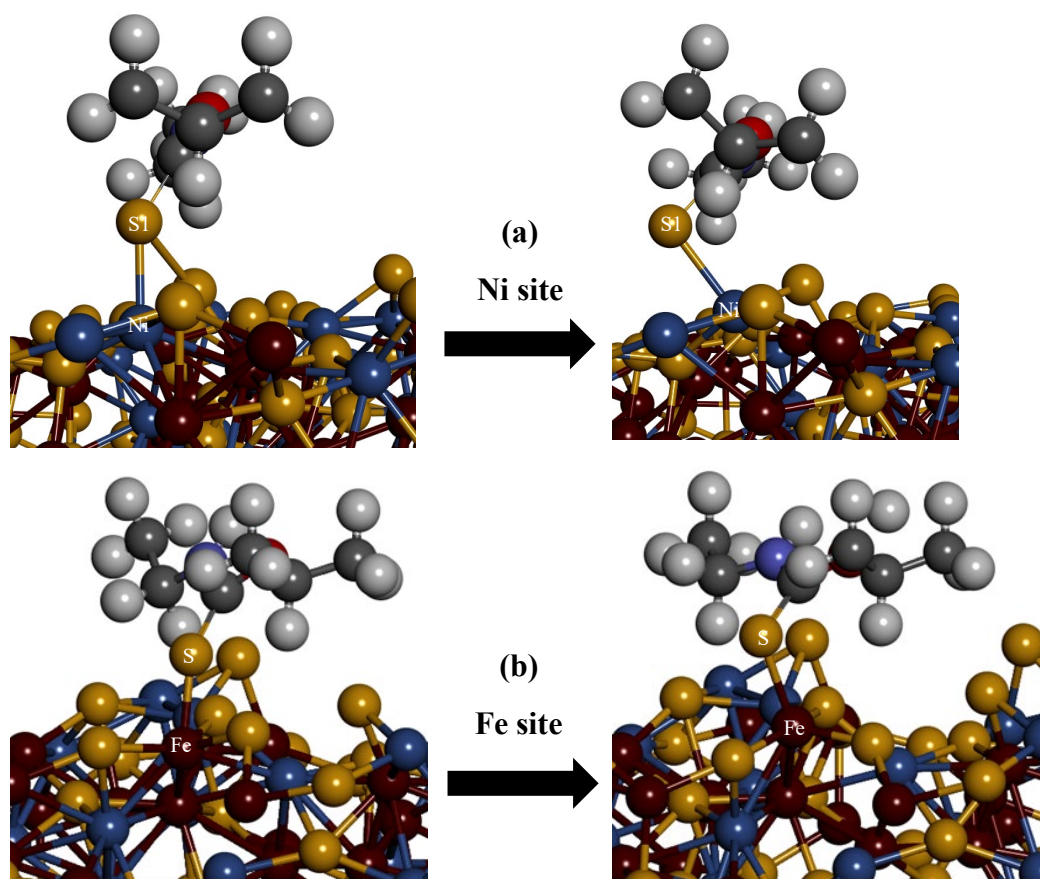


Figure D1.6: The un-relaxed and relaxed IPDETC collector adsorption on the  $\text{Fe}_5\text{Ni}_4\text{S}_8$  (311) surface.

Table D1.2: The adsorption energies of IPDETC on the  $\text{Fe}_5\text{Ni}_4\text{S}_8$  (311) mineral surfaces (kJ/mol).

Figure	Adsorption mode	$E_{\text{ads.}}$ (kJ.mol <sup>-1</sup> )	$E_{\text{dis.}}$ (kJ.mol <sup>-1</sup> )	Ni-S1 (Å)	Fe-S1 (Å)	Fe-S2 (Å)
D1.4	Ni-S1	-51.15	-109.92	2.38	-	-
	Fe-S1	-82.99	-103.32	-	2.47	-
D1.5	Ni-S1	-90.13	-56.17	2.27	-	-
	Fe-S1	-	-	-	-	-
D1.6	Ni-S1	-151.38	-85.82	2.39	-	-
	Fe-S1	-103.59	-89.79	-	2.26	-

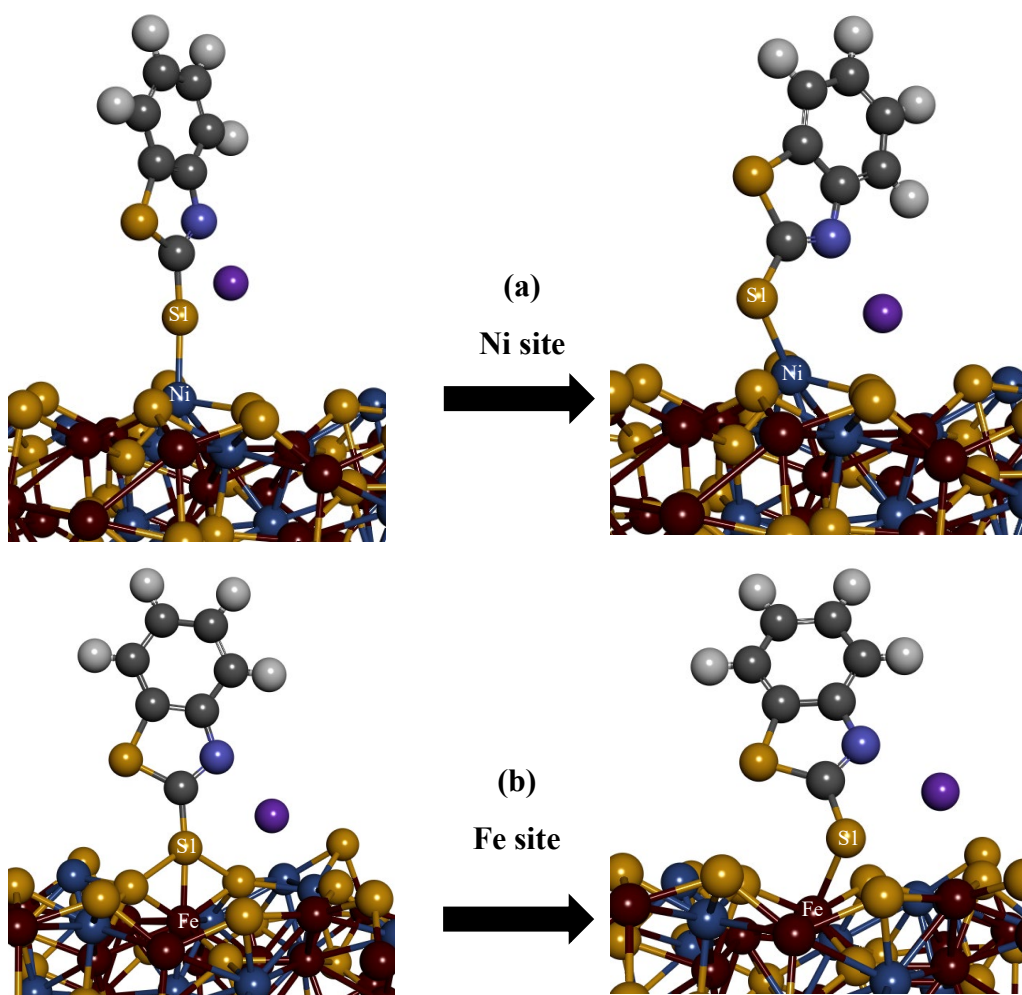
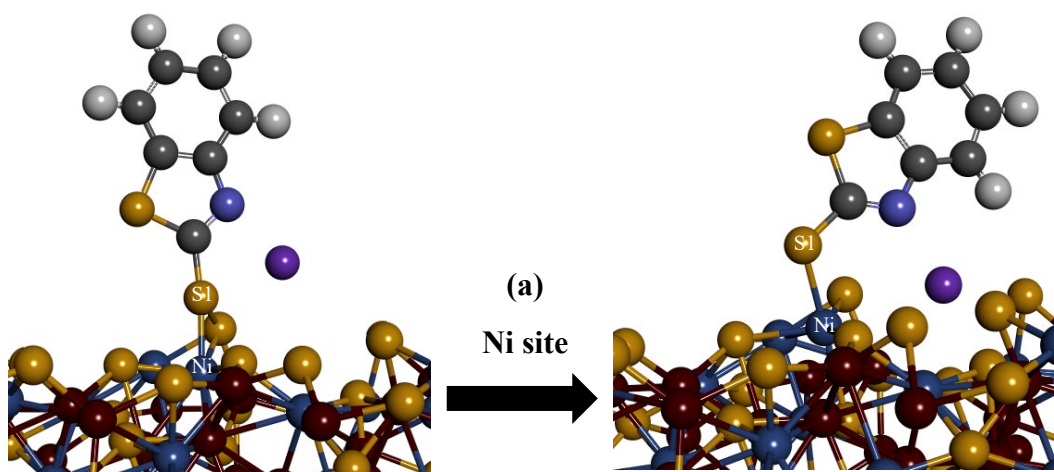


Figure D1.7: The un-relaxed and relaxed MBTNa collector adsorption vertical on the  $\text{Fe}_5\text{Ni}_4\text{S}_8$  (311) surface.



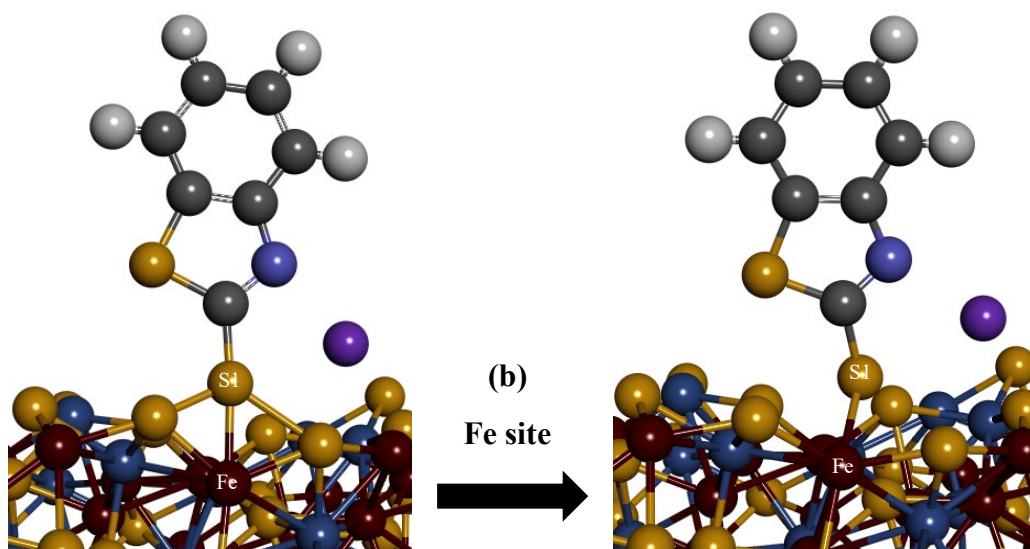
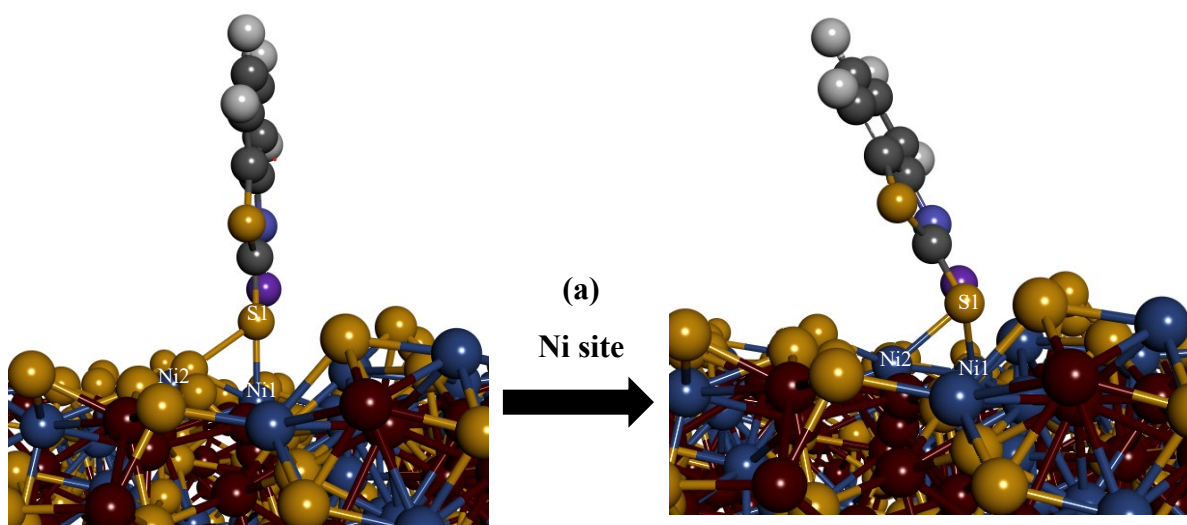


Figure D1.8: The un-relaxed and relaxed MBTNa collector adsorption vertical on the  $\text{Fe}_5\text{Ni}_4\text{S}_8$  (311) surface.



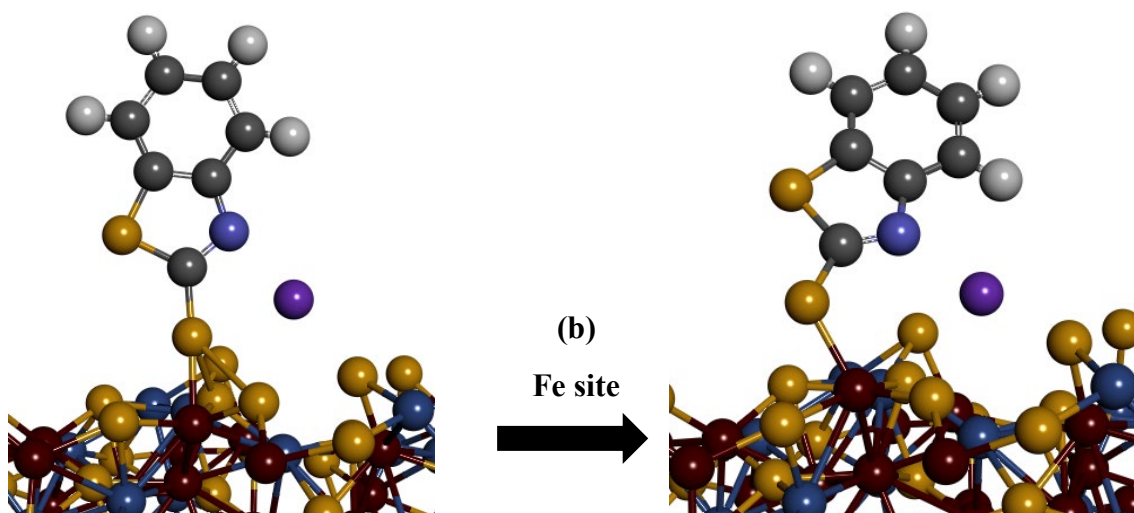
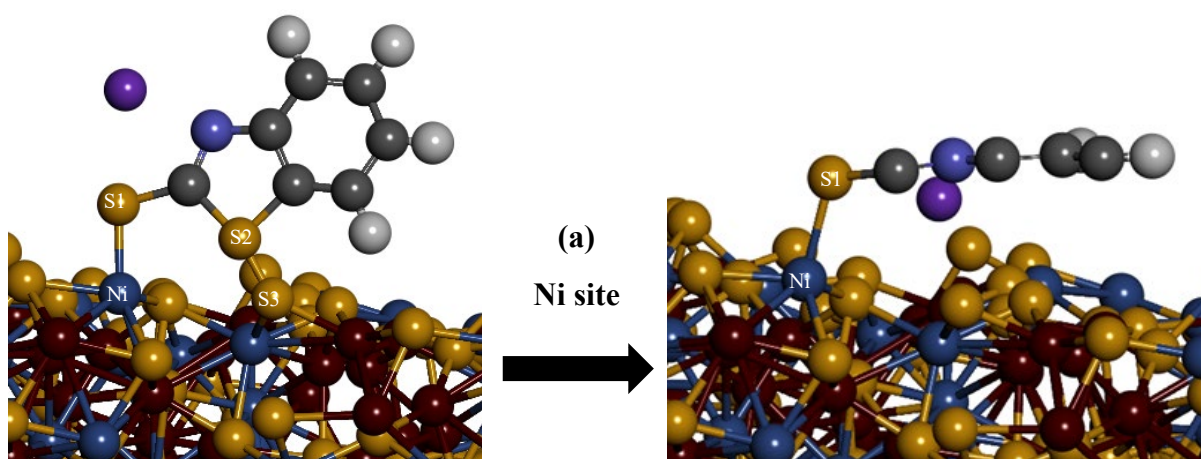


Figure D1.9: The un-relaxed and relaxed MBTNa collector adsorption vertical on the  $\text{Fe}_5\text{Ni}_4\text{S}_8$  (311) surface.

Table D1.3: The adsorption energies of MBTNa on the  $\text{Fe}_5\text{Ni}_4\text{S}_8$  (311) mineral surfaces (kJ/mol).

Figure	Adsorption mode	$E_{\text{ads.}}$ (kJ.mol <sup>-1</sup> )	$E_{\text{dis.}}$ (kJ.mol <sup>-1</sup> )	Ni-S1 (Å)	Fe-S1 (Å)	Fe-S2 (Å)
D1.7	Ni-S1	-204.28	-74.72	2.20	-	-
	Fe-S1	-178.96	-86.65	-	2.40	-
D1.8	Ni-S1	-140.67	-74.87	2.28	-	-
	Fe-S1	-82.46	-38.98	-	2.40	-
D1.9	Ni-S1	-170.34	-87.90	2.32	-	-
	Fe-S1	-162.89	-78.07	-	2.19	-



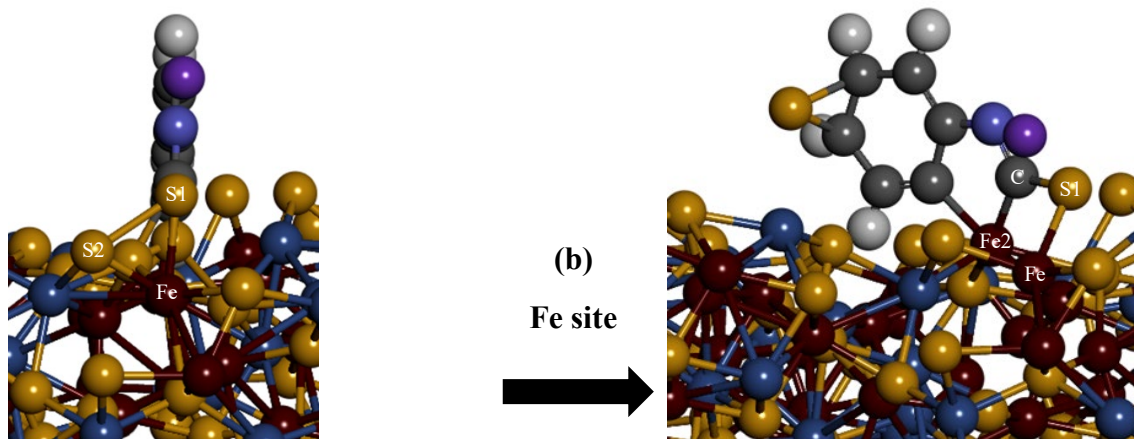


Figure D1.10: The un-relaxed and relaxed MBTNa collector adsorption horizontal on the  $\text{Fe}_5\text{Ni}_4\text{S}_8$  (311) surface.

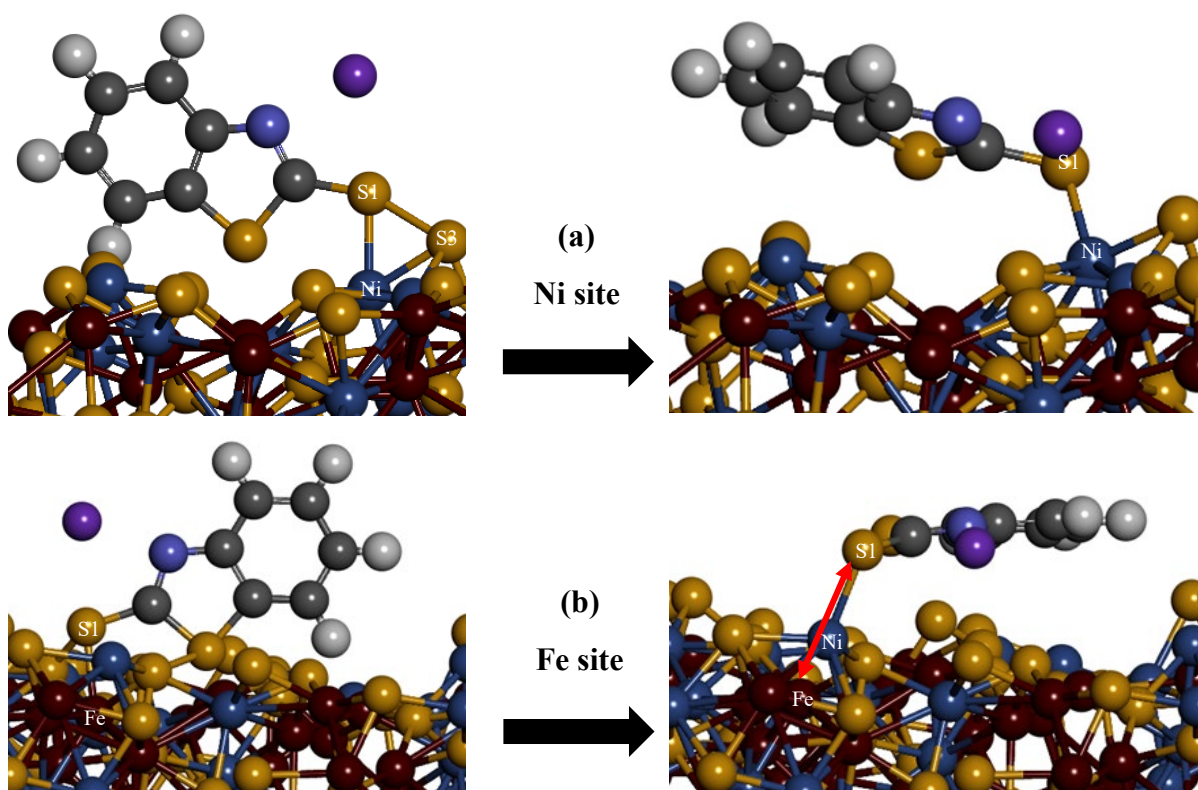


Figure D1.11: The un-relaxed and relaxed MBTNa collector adsorption horizontal on the  $\text{Fe}_5\text{Ni}_4\text{S}_8$  (311) surface.

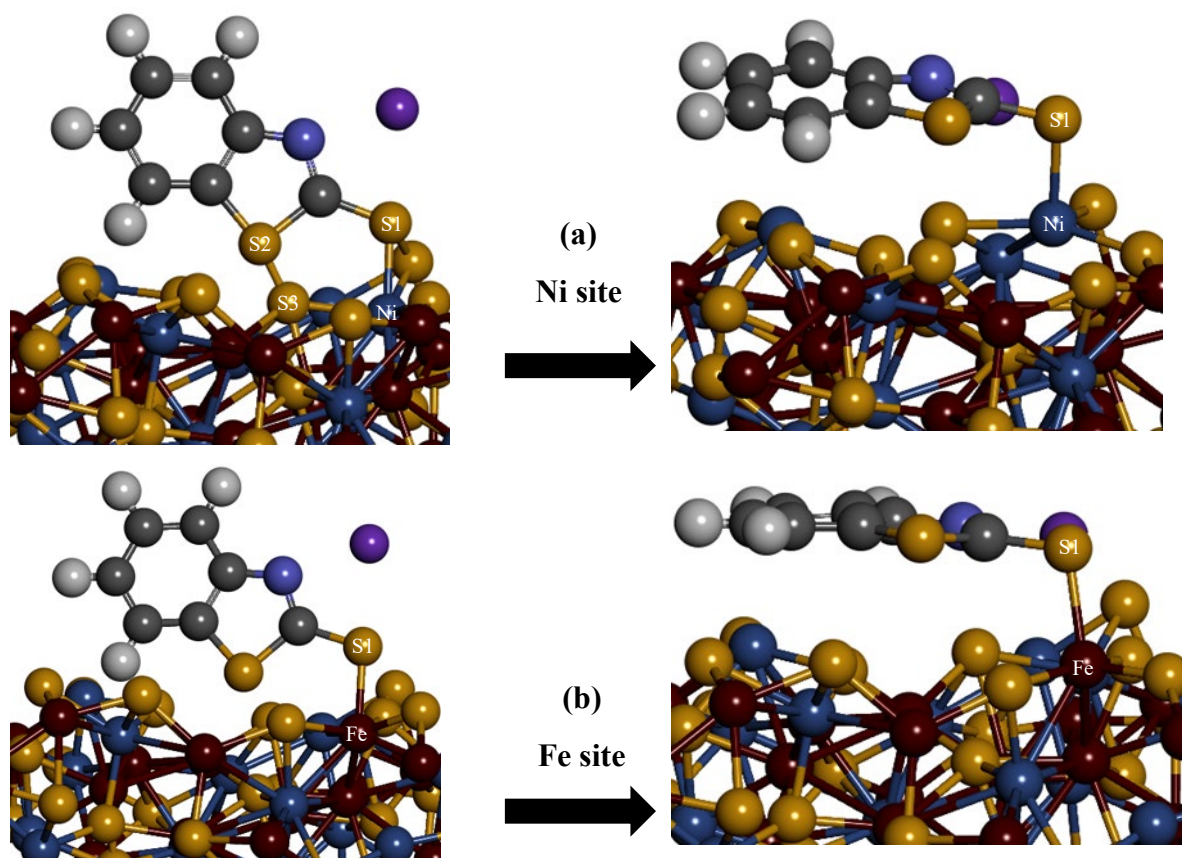


Figure D1.12: The un-relaxed and relaxed MBTNa collector adsorption horizontal on the  $\text{Fe}_5\text{Ni}_4\text{S}_8$  (311) surface.

Table D1.4: The adsorption energies of MBTNa on the  $\text{Fe}_5\text{Ni}_4\text{S}_8$  (311) mineral surfaces (kJ/mol).

Figure	Adsorption mode	$E_{\text{ads.}}$ (kJ.mol <sup>-1</sup> )	$E_{\text{dis.}}$ (kJ.mol <sup>-1</sup> )	Ni-S1 (Å)	Fe-S1 (Å)	Fe-S2 (Å)
D1.10	Ni-S1	-228.76	-109.99	2.27	-	-
	Fe-S1	-80.25	-93.97	-	2.22	-
D1.11	Ni-S1	-200.66	-113.81	2.25	-	-
	Fe-S1	-221.16	-102.46	-	5.05	-
D1.12	Ni-S1	-156.00	-116.74	2.32	-	-
	Fe-S1	-248.82	-124.82	-	2.33	-

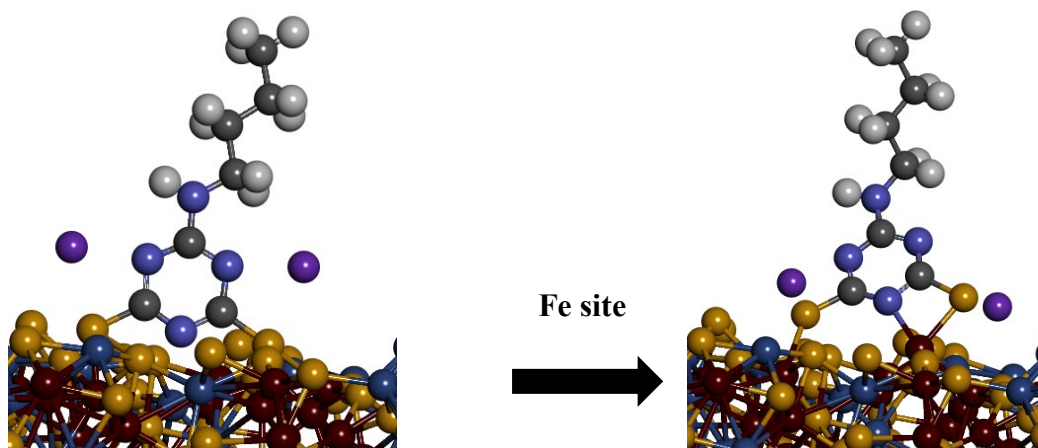


Figure D1.13: The un-relaxed and relaxed STDBAT collector adsorption on the  $\text{Fe}_5\text{Ni}_4\text{S}_8$  (311) surface.

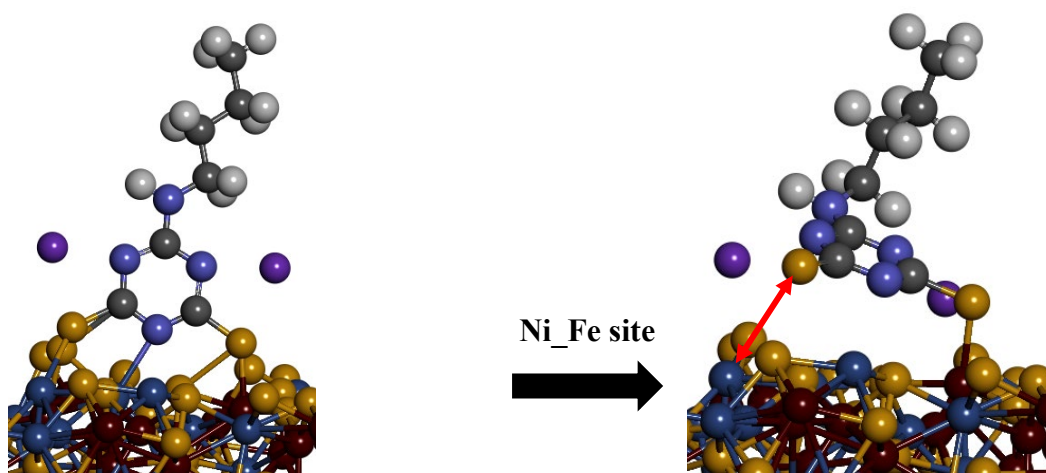


Figure D1.14: The un-relaxed and relaxed STDBAT collector adsorption on the  $\text{Fe}_5\text{Ni}_4\text{S}_8$  (311) surface.

Table D1.5: The adsorption energies of STDBAT on the  $\text{Fe}_5\text{Ni}_4\text{S}_8$  (311) mineral surfaces (kJ/mol).

Figure	Adsorption mode	$E_{\text{ads.}}$ (kJ.mol <sup>-1</sup> )	$E_{\text{dis.}}$ (kJ.mol <sup>-1</sup> )	Ni-S1 (Å)	Fe-S1 (Å)	Fe-S2 (Å)
D1.13	Ni-S1	-190.72	-30.65	-	2.26	2.29
D1.14	Ni-S1	-265.34	-133.80	4.03	-	2.23